CONSTRUCTIVE UTILIZATION OF INTENTIONAL NONLINEARITY IN SYSTEMS OF COUPLED MICRO/NANOMECHANICAL RESONATORS

BY

BONGWON JEONG

DISSERTATION

Submitted in partial fulfillment of the requirements
for the degree of Doctor of Philosophy in Mechanical Engineering
in the Graduate College of the
University of Illinois at Urbana-Champaign, 2014

Urbana, Illinois

Doctoral Committee:

Professor Alexander F. Vakakis, Chair and Director of Research
Professor Lawrence A. Bergman, Co-Director of Research
Professor William P. King
Research Associate Professor D. Michael McFarland
Professor Min-Feng Yu, Georgia Institute of Technology

Abstract

Micro/nanomechanical resonators have been actively studied in the last decade in designs of highly sensitive detection, high frequency signal-processing, and high speed switching. These designs benefit from the exceptional dynamic characteristics of these systems, *i.e.*, high frequency resonance and high Q-factor, arising from their small length scales. Most of previous studies in micro/nanomechanical resonators, however, remain in the framework of the linear dynamics while the inherent nonlinearity of these systems is either neglected or considered as unwanted. In some works nonlinear effects are taken into account, but these are considered as perturbations of linear effects, and mostly explored in the regime of weakly nonlinear effects. Some additional recent works have focused on intentionally exploiting the rich dynamics arising from the intrinsic nonlinearities in micro/nanomechanical resonators, and showing that these nonlinear dynamics can be beneficial in satisfying design objectives that could not be met with in linear settings.

In this dissertation, we further exploit the constructive utilization of intentional strong nonlinearities in the design of micro/nanomechanical resonators. We present three different studies incorporating intentional strong nonlinear dynamics in diverse applications, with the aim to perform fundamental studies of these systems, but also with significant practical applications. In these systems the intentional utilization of nonlinearity was enabled by introducing 'mechanical coupling' through the integration of nanoscale components onto readily realized microcantilever systems.

For a system of a microcantilever with an attached nanotube and harmonic base excitation we report expansion of its resonance bandwidth through by the geometric nonlinearity generated by the flexibility of the nanotube, as well as strong nonlinear damping effects. These nonlinearities have significant influence of the resonance bandwidth and the effective Q-factor of the system. In addition, we develop a methodology for identifying and quantifying the nonlinear damping effects originating from the oscillations of flexible nanocomponents to the dynamics of microresonators to which they are attached. For a system of two microcantilever resonators coupled by a nanomembrane and under harmonic base excitation, we study the effect of varying the coupling strength on the nonlinear dynamics and show that in the limit of weak coupling nonlinear localization occurs in this system. Moreover, we report strongly nonlinear resonance phenomena, such as sudden transitions in the resonance amplitude for small increase or decrease of the frequency of base excitation, multiple co-existing resonance solutions and nonlinear hysteresis phenomena. In addition, we report interesting frequency shifts to resonance peaks of the response at different sensing positions of the coupled microcantilevers, and attribute these shifts to nonpropertional damping effects. These same damping effects generate 'splitting' of resonance modes with decreasing coupling. In both applications our theoretical findings are validated by experimental tests.

Finally, we present a new concept for high-frequency AFM design, whereby an intentional *1:n* nonlinear resonance is introduced into a traditional AFM microcantilever with an attached nanomembrane for the purpose of significantly amplifying the n^{th}

harmonic component of its steady state response. This is achieved by nonlinear energy transfers from low to high frequencies that are activated by the internal resonance; these energy transfers not only magnify the high frequency components in the detection signal, but, perhaps even more importantly, affect the phase of this signal, which in turn can be used to enhance the sensitivity and performance of the nonlinear AFM design, compared to current traditional linear designs. The capability of the proposed AFM system for discretely imaging the compositional differences of inhomogeneous specimen is assessed experimentally.

The findings reported in this dissertation extend the state-of-the-art in the design of nonlinear micro/nanomechanical resonators. Furthermore, our concepts and results can contribute towards a new paradigm of exploiting intentional strong nonlinearities in these systems, with diverse practical applications and with benefits that would not otherwise obtainable with current linear designs.

Acknowledgements

It would not have been possible for me to reach the end of my PhD studies without all the considerate supports and helps from the people I met in University of Illinois. First of all, I would like to express my deepest gratitude to my advisor, Prof. Alexander F. Vakakis, for his thoughtful advices and insightful guidance in my PhD research. Not to mention his great support in the research perspective, I will be always grateful for his patience and encouragement whenever I was standing on the edge of losing the confidence and the enthusiasm during my PhD studies. Also, I would like to truly thank my co-advisors, Prof. Lawrence A. Bergman, Prof. D. Michael McFarland and Prof. Min-Feng Yu, for their insightful discussions, invaluable suggestions and considerate encouragement in every aspect in the pursuit of my PhD studies. It was no doubtfully a great luck of my life to receive the interdisciplinary perspectives from the diverse research backgrounds, which couldn't have been possible without my co-advisors. I would like to also thank Prof. William P. King, for not only his support and advice as a PhD committee member but also providing me with a key idea for the breakthrough in the realization of the nonlinear systems. My special thanks go to my collaborators, Prof. Hanna Cho, Prof. Seok Kim and Hohyun Keum – without their previous accomplishments in the theoretical, experimental and manufacturing basis, none of my current research works could have come to the reality. Finally, but not for the least, I would like to convey my appreciation to the members of LNDVL and NSTG, and my friends in MechSE Korean Student Association, for being together at the moments of paving a way to overcome the difficulties, yet sharing the happiness of the graduate life.

I can never thank enough my wife, Seongju, for her unfathomable love she has shown in my pursuit of PhD degree. Being apart for a long time, I cannot easily imagine her sufferings and sacrifices in the absence of myself beside her. I will be always in debt of her unbounded love. I would like to also express my deepest love to my parents and sister, whose endless support always let me stand still.

Nov. 4, 2014

Bongwon Jeong

Table of Contents

Chapter 1

Introduction: Intentional Utilization of Nonlinearity in the Micro/Nano-Scales

Advances in mirco/nanotechnology in the last two decades have led to the development of miniaturized multi-physical devices that receive an electrical signal as input and convert it in turn to useful mechanical motion, or vice versa. Such devices have been often referred to as micro/nano-electromechanical systems (MEMS/NEMS). As one of the main branches of M/NEMS devices, mirco/nanomechanical resonators have been designed to attain oscillatory responses by periodic flexural/torsional deformations of their mechanical components when subjected to harmonic base motions or harmonic excitation forces.

Micro/nanomechanical resonators exhibit extraordinary dynamic characteristics, which are unrealizable in macro-scale systems; *e.g.*, the range of their natural frequencies is typically within 10^4-10^9 Hz, and the corresponding Q-factors are in the range of 10^0-10^5 (Rhoads *et al.*, 2010). These exceptional properties which benefit from the small dimensions of these systems are favorable for high sensitivity detection, high frequency signal-processing, and optical modulation applications. Moreover, the recent discovery of nanomaterials with exceptional mechanical properties and low densities, *e.g.* the carbon nanotube (CNT) or graphene, has boosted the advances in this field toward reaching the ultimate physical limit of micro/nanomechanical resonators, thus enabling fundamental studies at the atomic-scale using appropriately designed resonators.

Most of the previously considered micro/nanomechanical resonators have been designed and studied in the framework of linear dynamics. Nevertheless, nonlinearities in these dynamic systems frequently occur and are realized due to various sources. A micro/nano-scale structure due its enhanced flexibility and increased deformation due to its small length scale can enter the nonlinear dynamical regime. Also, actuation schemes employed to oscillate these dynamical systems (*e.g.*, electrostatic forces) or dynamic interactions between oscillating mechanical components and the surrounding ambient environment (*e.g.*, van der Waals forces) also may induce inherent nonlinearities. Rich dynamical behaviors arising from such intrinsic nonlinearity can be a potential solution to overcome limitations that the linear dynamic system poses (*e.g.*, narrow resonance bandwidth), but such inherent nonlinearity has been either ignored or regarded as detrimental to design objectives (Ekinci *et al.*, 2004; Ekinci and Roukes, 2005; Kacem and Hentz, 2009; Kacem *et al.*, 2010).

However, several recent studies have demonstrated the intentional utilization of intrinsic nonlinearity in micro/nanomechanical resonators for novel applications, such as resonance bandwidth expansion (Cho *et al.*, 2010 and 2012; Stanton *et al.*, 2010) and frequency-tuning (Rhoads *et al.*, 2005). These works demonstrate not only that the intrinsic nonlinearity can be utilized for practical usages, but also that the proposed systems incorporating controlled nonlinearities can be intentionally designed to attain dynamic behaviors, design objectives and enhanced performances that cannot be obtained using traditional linear concepts and methods.

Based on the previous discussion, a main objective of this dissertation is to develop micro/nanomechanical resonators that incorporate intentional nonlinear dynamics and composed of microcomponents with 'mechanical coupling' achieved by integrating flexible nanoscale components. We aim to study these systems in order to address both fundamental issues related to the effects of weak coupling and intrinsic nonlinearities on the dynamics, and also new design concepts that would be applicable for different practical applications. Our overall aim, however, is broader: To propose a new paradigm for designing flexible microresonators with nanoscale coupling elements that incorporate strong intentional stiffness and/or damping nonlinearities and possess properties that would not be otherwise obtainable in the absence of these nonlinearities.

The corresponding tasks in order to fulfill the above objective include: (i) To design flexible micro/nanoscale nonlinear dynamical systems that intentionally utilize the nonlinearities arising from their geometrical configurations or coupling interaction forces; (ii) developing representative mathematical models that accurately capture the nonlinear dynamics of the proposed micro/nanoresonators, followed by analytical and/or numerical studies of these models; (iii) constructing experimental systems based on the theoretically designed dynamical systems through unique micro/nanofabrication techniques; and (iv) experimentally validating the analytical estimations and the design predictions and objectives.

This dissertation consists of 6 Chapters, which are briefly summarized below. Each Chapter contains its own references and its own numbering system for the equations provided in the text. Chapter 2 outlines some basic theoretical concepts, discusses certain

applications of linear and nonlinear micro/nanomechanical resonators, and provides a brief summary of some of the nonlinear phenomena encountered in this work.

Chapter 3 considers the first system examined in this work, consisting of a nonlinear microcantilever system with typical dimensions of a conventional AFM microcantilever. Base harmonic excitation is provided to the system at frequencies close to its resonance frequency. In this system the nonlinearity is realized by the geometric modification of the microcantilever followed by integration of a boron nitride nanotube onto the microcantilever base. It is shown experimentally and analytically that the resonance bandwidth of this system is broadened by the nonlinear hysteresis originating from the increased flexibility of the nanotube attachment, indicating that a nanoscale attachment can introduce strongly nonlinear effects in an otherwise linear flexible microresonator. In addition, we find that a nonlinear damping effect is induced in this system due to the combination of geometric nonlinearity and the viscoelasticity of the attached nanotube. The influence of the nonlinear damping on the effective Q-factor and resonance bandwidth of the microcantilever is discussed, and a new way of experimentally testing the nonlinear damping properties of nanoscale flexible components is discussed.

In Chapter 4 we introduce a system of two microcantilevers that are nonlinearly coupled by a silicon nanomembrane whose width (and, hence, its coupling strength) can be accurately controlled by microfabrication. Again, harmonic base excitation is provided to the two microcantilevers at frequencies in the range close to, and in between their fundamental resonance frequencies. To overcome the fabrication difficulties of the nanostructure integration discussed in previous studies (Cho *et al.*, 2010 and 2012), we

incorporate the transfer-printing assembly technique to integrate the nanomembrane onto a set of microcantilevers for reliable realization of geometric nonlinearity. It is experimentally shown that the nonlinear dynamical response is triggered when the coupling strength becomes weaker than the axial stiffness of microcantilevers. Besides, nonlinear complex modes (*i.e.*, modes of oscillation with nontrivial phase differences between the motions of different points of the microstructure) are experimentally observed in the weakly coupled system, potentially induced by the nonlinear damping effect induced by the coupling nanomembrane. Strongly nonlinear effects, such as jump phenomena, nonlinear hysteresis loops, multiple stable co-existing steady state motions, mode 'splitting', and shifting of resonance peaks of the responses of different sensing positions on the system are experimentally observed, and theoretical models are proposed.

Chapter 5 introduces a new design concept for nonlinear multi-frequency AFM microcantilever design, exploiting *1:n* internal resonance for amplification of the n^{th} harmonic response of the system based on which the AFM operation is based. In the proposed design, a silicon nanomembrane is coupled to the AFM microcantilever as a form of an inner paddle, with its dimension being controlled according to a representative mathematical model. Specifically, the proposed nonlinear AFM system is designed to achieve a *1:n* ratio between its fundamental and its *n*-th eigenfrequencies. It is shown through numerical simulations and experimental studies that the amplitude of the n^{th} harmonic component of the response is amplified by the internal resonance, and, perhaps even more important, the sensitivity of its phase is greatly enhanced, which, in turn, provides an enhanced sensitivity compared to the fundamental harmonic of the response.

Tapping-mode AFM measurements on inhomogeneous polymer specimen is carried out to show that the higher harmonic of the measured response is capable of simultaneous compositional mapping and topography imaging.

We conclude this Dissertation with Chapter 6 where the main findings of this work are summarized and their potential applications to practical designs of N/MEMS are discussed. In addition, suggestions for further work are provided.

REFERENCES

Cho, H., Jeong, B., Yu, M.-F., Vakakis, A. F., McFarland, D. M., Bergman, L. A., Nonlinear Hardening and Softening Resonances in Micromechanical Cantilever-Nanotube Systems Originated from Nanoscale Geometric Nonlinearities, *Int. J. Solids Struct.,* 49, 2059-2065 (2012).

Cho, H., Yu, M.-F., Vakakis, A. F., Bergman, L. A., McFarland, D. M., Tunable, Broadband Nonlinear Nanomechanical Resonator, *Nano Lett.*, 10, 1793-1798 (2010).

Ekinci, K.L., Yang, Y.T., Roukes, M.L., Ultimate limits to inertial mass sensing based upon nanoelectromechanical systems, *J. Appl. Phys.*, 95, 2682–2689 (2004).

Ekinci, K.L., Roukes, M.L., Nanoelectromechanical systems, *Rev. Sci. Instr*., 76, 061101 (2005).

Kacem, N., Hentz, S., Bifurcation topology tuning of a mixed behavior in nonlinear micromechanical resonators, *Appl. Phys. Lett.*, 95, 183104 (2009).

Kacem, N., Arcamone, J., Perez-Murano, F., Hentz, S., Dynamic range enhancement of nonlinear nanomechanical resonant cantilevers for highly sensitive NEMS gas/mass sensor applications, *J. Micromech. Microeng.*, 20, 045023 (2010).

Rhoads, J. F., Shaw, S. W., Turner, S. W., Nonlinear Dynamics and Its Applications in Micro- and Nanoresonators," *J. Dyn. Sys. Meas. Control,* 132, 034001 (2010).

Rhoads, J., Shaw, S., Turner, K., Baskaran, R., Tunable microelectromechanical filters that exploit parametric resonance, *J. Vib. Acoust.*, 127, 423–430 (2005).

Stanton, S., McGehee, C., Clark, C.M., Mann, B.P., Nonlinear dynamics for broadband energy harvesting: Investigation of a bistable piezoelectric inertial generator, *Physica D*, 239, 640–653 (2010).

Chapter 2

Dynamics of Micro/Nanomechanical Resonators

2.1 Introduction

In this Chapter, we discuss the linear and nonlinear dynamics of micro-/nanomechanical resonators. Section 2.2 provides an overview on the general theory of the linear dynamics for single- and multi-degree-of-freedom systems. We also discuss notable applications developed in the framework of linear dynamics and their limitations. In Section 2.3, the sources of nonlinearity in micro/nanomechanical resonators are presented and their effects on the dynamics are briefly discussed. We also introduce some of the key new applications incorporating and taking advantage of the unique dynamical features induced by system nonlinearities.

2.2 Linear Micro/Nanomechanical Resonators

2.2.1. Basic Concepts

Micro/Nanomechanical resonators undergoing sufficiently small-amplitude oscillations and without certain types of constraints (*e.g.*, giving rise to clearance, friction or vibro-impact nonlinearities) can be studied in the framework of linear dynamics. In this context the basic assumptions regarding the oscillations of these systems are, (i) that the restoring forces originating from the geometrical configurations of the resonators are linearly

dependent on the resulting deformations; (ii) that any applied excitation force does not change significantly in magnitude and direction with respect to the direction of the oscillation; and (iii) that any stiffness or damping nonlinear effects do not affect the global dynamical properties of these systems, *e.g.*, their eigenfrequencies and their corresponding mode shapes, so that the principle of superposition holds. In this section, the basic concepts of the linear dynamics of a micro/nanomechanical resonator are briefly reviewed to provide the general theoretical background before we discuss the nonlinear dynamics of these systems.

2.2.1.1. Single Degree-of-Freedom Systems

In N/MEMS applications a micro/nanomechanical resonator is often modeled as a linear single-degree-of-freedom (SDOF) oscillator. This is the case when the system possesses a concentrated (discrete) instead of a distributed mass, and the inertia effects of supporting elements (such as springs and dampers) are small in comparison, and, thus, can be neglected. In additional applications, flexible (continuous) resonators, such as forced or unforced microcantilevers are operated close to one of their eigenfrequencies and having well-separated modes in frequency, can also be approximately reduced to sets of SDOF modal oscillators by employing modal analysis. Since these types of SDOF linear oscillators are rather often encountered in current N/MEMS studies, we start our discussion by providing a brief review of their linear steady state responses.

When a harmonically forced single degree-of-freedom dissipative dynamical system is operated in its linear regime, the governing equation of motion is given by,

$$m\ddot{x} + c\dot{x} + kx = F_0 \cos \omega t \tag{2-1}$$

where m is the actual mass (that is, a discrete inertia element) of a SDOF resonator or the modal (effective) mass of a particular mode of a flexible (continuous) resonator; similarly, c is either the actual or the modal viscous damping coefficient, and k the actual or modal stiffness, and x the resulting displacement. On the right hand side of Eq. (2-1), F_0 indicates the forcing amplitude and ω the driving frequency of the applied excitation. Assuming a steady state solution of Eq. (2-1) is in the following form,

$$x_{ss}(t) = X \cos(\omega t - \phi) \tag{2-2}$$

where X is the amplitude of the steady state response and ϕ is the phase shift of the response with respect to the applied harmonic force, substituting into to Eq. (2-1) and solving for X and ϕ we obtain the expressions:

$$X = \frac{F_0 / k}{\left[\left(1 - \left(\frac{\omega}{\omega_n} \right)^2 \right)^2 + \left(2\xi \frac{\omega}{\omega_n} \right)^2 \right]^{1/2}} \tag{2-3a}$$

$$\phi = \tan^{-1} \left(\frac{2\xi \frac{\omega}{\omega_n}}{1 - \left(\frac{\omega}{\omega_n} \right)^2} \right) \tag{2-3b}$$

In Eq. (2-3a) and (2-3b), ω_n is the undamped eigenfrequency (or natural frequency) of the system expressed as

$$\omega_n = \sqrt{\frac{k}{m}} \tag{2-4}$$

and ξ is the viscous damping ratio defined as:

$$\xi = \frac{c}{2\sqrt{mk}} \tag{2-5}$$

Then, the Q-factor, indicating the ratio of the energy stored to the energy dissipated per cycle, can be expressed in terms of the viscous damping ratio ξ as,

$$Q = \frac{1}{2\xi} = \frac{\omega_n}{\Delta\omega} \tag{2-6}$$

where $\Delta\omega$ is the half-power bandwidth.

As seen in Eqs. (2-3a) and (2-4), for weak damping the eigenfrequency of the system indicates approximately the location of the maximum steady state amplitude in the frequency spectrum, or the resonance of the system, and depends by the mass and stiffness of the oscillator. Clearly, a perturbation in the mass or stiffness will result in a shift in the perturbed natural frequency, which can be utilized as a mass- or stiffness-sensing parameter. The Q-factor, on the other hand, determines the sharpness of the resonance plot, *i.e.*, the steady state amplitude dependence on the excitation frequency, with the resonance in the neighborhood of the eigenfrequency becoming sharper for higher Q-factors. One can intuitively conclude that the aforementioned shift in the eigenfrequency is more clearly visualized for sharper resonance plots, so it can be surmised that the Q-factor is directly related to the frequency resolution, and, hence, to the sensitivity of the linear oscillation when used as a sensing device. Moreover, the previous discussion highlights one of the

basic features of linear resonators, namely that they are *narrowband* devices, undergoing large-amplitude responses only in the neighborhood of their eigenfrequencies.

In addition to the case of harmonic excitation considered in Eq. (2-1), another common application is a micro/nanoscale resonator excited by harmonic base motion, as widely adopted in AFM operations. Assuming that the mass of the resonator is attached to its base by a spring and a damper in parallel, the Eq. (2-1) is modified as follows,

$$m\ddot{x} + c(\dot{x} - \dot{y}) + k(x - y) = 0 \tag{2-7}$$

where y is the prescribed (harmonic) motion of the base. Assuming again that $y = Y \sin \omega t$, this equation becomes:

$$m\ddot{x} + c\dot{x} + kx = c\omega Y \cos \omega t + kY \sin \omega t \tag{2-8}$$

Assuming a steady state solution for x in the form of Eq. (2-2) and solving for X and ϕ we compute,

$$X = \frac{Y\left(1 + \left(2\xi \frac{\omega}{\omega_n}\right)^2\right)^{1/2}}{\left[\left(1 - \left(\frac{\omega}{\omega_n}\right)^2\right)^2 + \left(2\xi \frac{\omega}{\omega_n}\right)^2\right]^{1/2}} \tag{2-9a}$$

$$\phi = \tan^{-1}\left(\frac{2\xi\left(\frac{\omega}{\omega_n}\right)^3}{1 + \left(4\xi^2 - 1\right)\left(\frac{\omega}{\omega_n}\right)^2}\right) \tag{2-9b}$$

By comparing (2-9) and (2-3) we observe that the damping coupling term between the responses of the mass (x) and its base (y) generates different frequency responses for the

amplitude and the phase. In particular, we note that for base harmonic excitation it holds that at $\omega/\omega_n = \sqrt{2}$ it is satisfied that $X = Y$ for any damping ratio ξ, and that $\phi \neq \pi/2$ at the natural frequency (*i.e.*, at $\omega/\omega_n = 1$) as long as $\xi > 0$.

In micro/nanomechanical resonators operating in ambient pressure, however, the inherent dissipative effects arising from structural damping are considerably smaller compared to the dissipative effect provided by the surrounding air. It follows that assuming that this ambient dissipative effect is proportional to the absolute velocity of the mass, one may neglect the damping element connecting the mass to the base (*i.e.*, the structural damping effect) and instead include a viscous damping element connecting the mass to the ground (modeling air damping) in the model. Hence, in this case Eq. (2-1) can be used in a predictive capacity for experimental tests that are conducted in ambient environment. As discussed later in this dissertation, however, when similar experiments are performed under condition of high vacuum, the ambient dissipative effect is small and then can be neglected compared to structural damping which becomes dominant under such conditions.

2.2.1.2. Multi Degree-of-Freedom Systems

Typical micro/nanomechanical resonators are continuous, flexible systems with distributed inertia, stiffness and damping, possessing an infinite number of degrees of freedom. If more than one eigenmodes are excited by the initial conditions or the external excitation, the SDOF approximation discussed in Section 2.2.1.1 no longer applies, and one must resort to a different approach for analyzing the linear dynamics. Although direct vibration

analysis based on continuum models may provide analytical solutions that reflect the dynamics more precisely, this requires the explicit solution of coupled partial differential equations in space and time; this task can be tedious. On the contrary, it is often advantageous to approximate a continuous resonator by a MDOF lumped-parameter model since this enables a simplified analysis with an acceptable tolerance within the frequency range of interest of the specific application. In that case one needs to take into account only the vibration modes of the continuous resonator with eigenfrequencies in that specific frequency range, and then apply modal analysis to reduce the original coupled governing differential equations to sets of coupled ordinary differential equations, which in turn can be decoupled by suitable modal transformations.

Although issues such as non-proportional damping distribution in a system (due to local damping sources, for example) can complicate this procedure, the simplification obtained justifies the use of this methodology in many applications. Hence, in the following exposition we briefly summarize the MDOF analysis leading to the aforementioned lumped-parameter models.

Considering a flexible micro/nanomechanical resonator operating within a specified frequency range where n of its modes lie, and assuming linear dynamics, we define n coordinates (degrees of freedom) and model the resonator as an n-DOF dynamical system. To this end, we denote by x_i the displacement corresponding to the i-th coordinate and assemble the overall n-vector of displacements as follows:

$$\{x\}^T = \{x_1, x_2, \cdots, x_{n-1}, x_n\} \tag{2-10}$$

Eq. (2-10) is utilized to express the equations of motion in a matrix form as,

$$M\{\ddot{x}\} + K\{x\} = \{F(t)\} \tag{2-11}$$

where M and K are the $n \times n$ mass matrix and stiffness matrix, respectively. Dissipative effects are neglected, and $\{F(t)\}$ represents the vector of the external forces exerted on the coordinates. In general (2-11) represents a set of coupled linear ordinary differential equations. This set can be reduced to a set of uncoupled ordinary differential equations by appropriate modal transformations whereby the coordinate vector is expressed as $\{x\}^T = P\{v\}^T$ where P is the modal matrix composed of the eigenvectors of system (2-11) when the external forces are neglected, and $\{v\}^T$ represents the n-vector of modal coordinates.

Substituting this coordinate transformation into Eq. (2-11), the equations of motion in the modal coordinate can be derived as

$$\{\ddot{u}\} + L\{u\} = \{f(t)\} \tag{2-12}$$

where the $n \times n$ matrix L is expressed as,

$$L = P^{-1}M^{-1}KP = \begin{bmatrix} \lambda_1 & 0 & \cdots & 0 \\ 0 & \lambda_2 & \cdots & 0 \\ \vdots & \vdots & \ddots & \vdots \\ 0 & 0 & \cdots & \lambda_n \end{bmatrix} \tag{2-13}$$

and the modal force vector $\{f(t)\}$ is given by:

$$\{f(t)\} = P^{-1}M^{-1}\{F(t)\} \tag{2-14}$$

Given that L in Eq. (2-13) is a diagonal matrix, we conclude that Eq. (2-12) represents a set of uncoupled ordinary differential equations, with each equation being analogous to Eq. (2-1) for the SDOF oscillator derived in Section 2.2.1.1. It follows that each of the n

equations in system (2-12) can be solved independently from the other equations, so each modal response is independent of the other modal responses. This result holds only for linear resonators though, and relies on the principle of linear superposition.

Moreover, the *i*-th eigenfrequency ω_i can then be estimated from the *i*-th eigenvalue λ_i as:

$$\omega_i = \sqrt{\lambda_i} \tag{2-15}$$

For each modal frequency ω_i, the corresponding modal shape is expressed by the eigenvector $\{v_i\}$. Once the modal responses are computed, the response in terms of physical coordinates can be computed using the previous modal coordinate transformation.

2.2.2. APPLICATIONS AND LIMITATIONS

The dynamical properties of linear micro/nanomechanical resonators are exceptional, exhibiting resonance frequencies in the range 10^4-10^9 Hz and Q-factors in the range 10^0-10^5 (Rhoads *et al.*, 2010). These remarkable properties benefit from the small length scales of these systems (10^1-10^4 μm) and the outstanding mechanical properties of the composing materials (*e.g.*, 10^2-10^4 GPa of Young's modulus). Among various attempts to exploit these unique advantages of linear micro/nanomechanical resonators, representative fields of application are in the areas of N/MEMS signal-processing and physical sensing.

Indeed, a micro/nanomechanical resonator with a resonance frequency overlapping with the radio frequency range (3 kHz-300 GHz), can be utilized as an electromechanical component in RF wireless communications. Recent works have demonstrated the

feasibility of using considerably small (~1 μm) electromechanical components consisting of single-walled carbon nanotubes as simultaneous antennas and tunable filters, thus forming essential components of radio devices (Jensen *et al.*, 2007; Gouttenoir *et al.*, 2010). In this application, the frequency-tunability and bandwidth are of great concern as they are directly related to the resulting signal processing performance. For example, a narrow bandwidth will limit the range of the frequency at which signal is received and processed through an electromechanical resonator. As explained by the analytical model in Section 2.2.1.1, however, the resonant frequency and Q-factor, whose changes are directly related to frequency-tuning and bandwidth respectively, are constant in the framework of linear dynamics as long as the configuration of the resonating system and its operational environment remain stationary. This limitation arising from the inherent narrowband nature of the linear dynamical resonance response can be overcome by designing the overall system to include a mechanism that can perturb the resonator; from an implementation point of view, however, this is not preferable or desirable, since the addition of another (perturbation) mechanism in the system sometimes results in design complexity, and accordingly complicates considerably the fabrication processes.

The other major application of the linear micro/nanomechanical resonator is in its use as physical sensor. As briefly discussed in Section 2.2.1.1, a shifting (perturbation) of the resonant frequency or the Q-factor of a linear resonator can be immediately detected due the narrowband resonance, and, hence can improve the sensitivity of this device in its capacity as sensor by enhancing the measurable resolution based on this frequency shift. Accordingly, micro/nanomechanical systems have been considered as exceptional sensing

devices. Some of the recent accomplishments in this area include the design of mass sensors with atomic resolution (Chiu *et al.*, 2008; Jensen *et al.*, 2008), force sensors capable of sensing a single spin (Rugar *et al.*, 2004) and a single electron-tunneling (Kouwenhoven *et al.*, 2009). However, it is noteworthy that further development of the sensing capacity of this type of linear resonators is restricted, considering that there exists a physical limit in the miniaturization of a nano/mechanical resonator. Besides, the oscillatory amplitudes of these devices need to be small enough to restrict their operation within the linear dynamic regime, and in order to maintain high Q-factors; excessive oscillations are expected to incur to Q-factor reduction and accordingly to reduced sensing sensitivity due to nonlinear effects such as, geometric nonlinearities and nonlinear dissipative forces (Jeong *et al.*, 2013). However, measuring small oscillation amplitudes, especially of nanoscale mechanical resonators, is sometimes quite challenging and may require a complicated measurement scheme. Overall, the aforementioned limitations pose technical obstacles that cannot be conveniently overcome in the framework of linear dynamics.

This calls for a better understanding of the effects of nonlinearities on the operation of micro/nanomechanical resonators, and, based on this understanding, of constructive utilization of intentional nonlinearities for the design of these systems for enhanced capacity and performance compared to their linear analogs. In the next section we provide a brief introduction in the field of nonlinear dynamics of these devices.

2.3. Nonlinear Micro/Nanomechanical Resonators

2.3.1. Nonlinear Dynamics in N/MEMS

Compared to macroscopic dynamic systems, micro/nanomechanical resonators exhibit more profound nonlinear dynamical effects that are attributed to unique physical phenomena that are only observable (and realizable) in small scales. The nonlinearity affects the dynamics in various ways, with each source of nonlinearity capable introducing unique and complex dynamical phenomena that are not encountered in linear settings, and cannot be understood and studied in the context of linear theory. Below, we discuss various sources of nonlinearity in micro/nanomechanical resonators, followed by an overview of some concepts related to their constructive utilization in practical designs and applications.

2.3.2. Sources of Nonlinearity

2.3.2.1. Geometric Nonlinearity and Nonlinearity due to Constraints

The inherent geometric configuration, kinematics and constraints of micro/nanomechanical resonators often induce strong nonlinearity in their dynamics. Particularly constrained flexible systems, such as clamped-clamped microcantilevers, nanotubes, micro/nanomembranes or nanowires can exhibit strong nonlinearities leading to broadband resonances.

For example, the transverse oscillations of a clamped-clamped flexible resonator induce length elongation and nonlinear mid-plane stretching, which, in turn, results in the

generation of axial tension. This axial tension, serving as a restoring force through which the resonating structure switches back to its initial shape, introduces geometric nonlinearly with respect to the transverse displacement in the direction of the oscillation. As discussed later, this type of geometric nonlinearity typically gives rise to a cubic term in the transverse force – transverse displacement law governing the oscillation of the resonator, which in turn results in hardening-type stiffness nonlinearity. Accounting for such a nonlinear cubic relationship into the corresponding equation of motion, and assuming that in the frequency range of interest one can take into account only one mode of vibration of the flexible resonator, the dynamics can be approximately reduced to the well-known Duffing oscillator (Nayfeh and Mook, 1995).

When a Duffing oscillator is subjected to an adequately strong harmonic excitation, its resonance plot depicting the magnitude of its steady state oscillation as function of the driving frequency bends toward frequencies higher than the intrinsic resonance frequency predicted by linear theory. This is referred to as 'stiffness-hardening' nonlinear behavior and it is a characteristic nonlinear feature, that gives rise to dynamic phenomena such as co-existing stable steady state solutions, 'jumps' (*i.e.*, sudden transitions between different stable steady state responses when small perturbations are applied to the system), and nonlinear hysteresis loops. Specifically, in the stiffness-hardening region, a bifurcation occurs as the response of the system converges to either one of two stable steady state responses. At the point where the bifurcation occurs, a sudden transition from one stable point to another is observed in the frequency response, which is referred as 'jump phenomenon'.

This type of nonlinear effects is caused by nonlinear stretching of the midplane section of the flexible structure (considered to be an extensible flexible body) resulting from the geometrical configuration and the boundary conditions (constraints), but not from the material behavior which is typically linear. For example, in another type of (inextensible) clamped-free microcantilevers, nonlinear dynamic behavior again occurs due to their geometric configurations, but it does not occur unless the resonators are subjected to excitation forces of excessive magnitudes, and is mainly caused by the nonlinear curvature – transverse displacement relationship and longitudinal inertia effects. This is because for clamped-free flexible resonators, unlike the clamped-clamped case, no axial tension is formed, as they are unconstrained at one of their ends. It is noteworthy, however, that integrating a very small mechanical component that restricts the oscillatory motion at the free end can again induce the previous type of geometric nonlinearity (Cho *et al.*, 2012a and b; Jeong *et al.*, 2013).

Hence, geometric nonlinear effects occur in both extensional and inextensional flexible micro/nanoresonators, but the source of the nonlinearity can be different. In both cases, however, assuming that the resonator is forced harmonically close to one of its linearized eigenfrequencies, the nonlinear dynamics can be studied by SDOF reduced-order models similar to the Duffing system.

A more challenging source of nonlinearity is caused by rigid boundaries constraining the oscillation of the flexible resonators, leading to clearance, vibro-impact or dry friction effects. These represent a class of particularly strong nonlinearities that can affect the response even at low amplitudes of oscillation. Their study requires special

computational and experimental effects since the resulting dynamics can be highly complex and chaotic. It is interesting to note that this commonly encountered source of strong nonlinearity can affect drastically the dynamics of otherwise linear resonators of even simple configurations (*e.g.*, SDOF linear oscillators with a rigid constraint), and their understanding is important in applications such as tapping mode atomic force microscopy.

2.3.2.2. Nonlinear Damping

Another source of the nonlinearity is the nonlinear damping induced by the geometrical configuration and the energy dissipation in the composing material of an oscillating micro/nanoresonator. Accounting for structural damping in combination with geometric nonlinearity, the overall energy dissipation during the oscillation of the resonator can no longer be regarded as being linearly proportional to the velocity of the oscillation, as shown in the recent analytical studies (Lifshitz *et al.*, 2010; Zaitsev *et al.*, 2012). Instead, the overall damping force is expressed as a nonlinear function with respect to the velocity and the displacement of the resonator. The works by Eichler *et al.* (2011) and Jeong *et al.* (2013) have shown experimentally that the nonlinear damping determines the maximum attainable values of the Q-factor, and defines the available resonance bandwidth of the steady state response. In cases when the resonator is in ambient environmental conditions, the ambient damping effects caused by the pressure of the surrounding air may be dominant compared to the inherent structural damping of the resonator, thus rendering the nonlinear damping effects almost negligible. Nevertheless, in many micro/nanomechanical systems

that are operated in high vacuum environment where the effect of ambient damping is small, the structural damping effect can be dominant. In such cases, when driving the system with high-amplitude excitation in order to achieve high Q-factor, the nonlinear structural damping effects must be taken into design consideration, since they can be dominant in the dynamics.

2.3.2.3. Nonlinear Force-System Interaction

In the micro/nanoscale, there exist interesting physical phenomena unobservable in the macroscopic scale, such as van der Waals attractions and the Casimir effect. Micro/nanomechanical resonators sometimes involve these unique phenomena in their operation, and in most cases, these phenomena give rise to highly nonlinear forces. Hence, even though a system is designed to operate in the regime of linear dynamics, the strong nonlinearity emerging from such micro/nanoscale interacting forces can result in complicated, strongly nonlinear dynamic behaviors.

One of the representative micro/nanoscale applications involving nonlinear interaction forces is probe-scanning microscopy, in particular, atomic force microscopy (AFM). When a sensing tip attached to the free end of an AFM microcantilever interacts with the sample substrate, the tip experiences an attractive force by van der Waals effect and/or a repulsive force by the elastic deformation of the tip when it interacts with the surface of the elastic specimen, resulting in complicated nonlinearity. As a result, a shift in the resonant frequency occurs followed by changes in the amplitude and phase of the

measured response (R. Garcia, 2010), through which the topographical and compositional images, respectively, of the specimen can be sensed and measured.

2.3.2.4. Nonlinear External Potential Forces

Finally, nonlinearity in the dynamics of micro/nanomechanical resonators is sometimes induced intrinsically by the external potentials, which are originally employed for the actuation and/or data acquisition mechanisms. Electrostatic actuation, for example, is one of the commonly utilized schemes to interrogate a mechanical structure in the micro/nanoscale. In electrostatic actuation, the change in the capacitance (proportional to the electrostatic force) with the oscillation amplitude of the resonator is highly nonlinear, especially for cases when a system is configured as a set of parallel plates, resulting in nonlinear actuation forces. This nonlinear force induces a stiffness-softening behavior when it is used for direct excitation, or an emergence of several unstable response regimes through frequency modulation when used for parametric excitation (Rhoads et *al.*, 2010).

2.3.3. APPLICATIONS

Early studies on nonlinear micro/nanomechanical resonators have focused on understanding the rich but complicated dynamical phenomena induced by the nonlinearity. Yet, there have been recent attempts to utilize and implement some of the unique dynamic features arising from nonlinearities, *e.g.*, bi-stability, wide resonance bandwidth and internal resonance, in designs of new classes of nonlinear resonators in the micro/nanoscale

with unique capacities, and to employ these designs in novel applications. Below, we summarize some of the key practical applications reported recently.

Bi-stability due to the stiffness-hardening and/or softening could be a favorable feature for electrical signal-processing components, since the abrupt change of the oscillation amplitude in the vicinity of a jump frequency (i.e., a transition point) is suitable for rapid switching and other signal amplifying purposes with high signal-to-noise ratios (SNR). Such a nonlinear dynamical system realized as an electrical component was reported by Guerra *et al.* (2008) where a nonlinear dynamical switch implementing the concept of bi-stability was implemented; in that system, switching from one state to another was performed through adjusting the phase in the modulation signal. Karabalin *et al.* (2011) report the design of a switch with three states by utilizing a set of two nonlinear mechanical resonators. Besides, bi-stability is also preferable for sensing purposes since the corresponding shift in the jump frequency due to a mass or energy perturbation can be conveniently measured with less influence from the Q-factor owing to the aforementioned high SNR, compared to the corresponding shifts in the resonance frequencies of linear resonators. Indeed, the nanomechanical resonator developed by Cho *et al.* (2010) employed the jump phenomenon for a mass-sensing application and reported a measurement resolution of 2.18 Hz/zepto-gram.

Moreover, internal resonance is defined as a strongly nonlinear phenomenon whereby under certain conditions strong nonlinear energy transfers occur between two or more modes, even if they are widely separated in frequency. The resulting nonlinear beat phenomena cannot be observed in linear systems, where the only possibility of strong

energy exchange between modes is when their frequencies are closely spaced. It is well know that internal resonances occur in systems with no damping (Nayfeh and Mook, 1985); when dissipation effects are taken into account resonance captures may occur leading to targeted (*i.e.*, unidirectional) energy transfer (Vakakis *et al*., 2008) between different nonlinear modes. The ensuing strong energy transfer can selectively amplify the response of selected modes of a flexible resonator, which, in turn, can be applied to applications such as high-frequency atomic force microscopy; this particular application will be discussed later in this dissertation. Internal resonances were also employed in signal-processing and sensing applications, *e.g*., implementing them in band-pass signal filters (Vyas *et al.*, 2008 and 2009), and in noise mitigation microdevices (Antonio *et al.*, 2012). Additionally, Chotolishvili *et al.* (2011) reported a nonlinear mass sensor incorporating an internal resonance, and demonstrated enhanced sensitivity compared to traditional linear sensing devices.

In the next Chapters we present three different applications of intentional use of strong nonlinearity in microresonators incorporating nanoscale coupling elements. Both computational and experimental studies are performed in each case and the rich nonlinear dynamical phenomena induced by the geometric nonlinearities are examined in detail. In addition, attention is provided in micro/nanofabrication issues in order to demonstrate the feasibility of practical implementation of the findings in practical applications.

REFERENCES

Antonio, D., Zanette, D. H., Lopez, D., Frequency Stabilization in Nonlinear Micromechanical Oscillators, *Nat. Comm.*, 3, 806 (2012).

Chiu, H.-Y., Hung, P., Postma, H. W. C., Bockrath, M., Atomic-Scale Mass Sensing Using Carbon Nanotube Resonators, *Nano Lett.*, 8, 4342–4346 (2008).

Cho, H., Jeong, B., Yu, M.-F., Vakakis, A. F., McFarland, D. M., Bergman, L. A., Nonlinear Hardening and Softening Resonances in Micromechanical Cantilever-Nanotube Systems Originated from Nanoscale Geometric Nonlinearities, *Int. J. Solids Struct.,* 49, 2059-2065 (2012a).

Cho H., Yu M.-F., Vakakis A., McFarland D.M., Bergman L.A., Dynamics of Microcantilever Integrated with Geometric Nonlinearity for Stable and Broadband Nonlinear Atomic Force Microscopy, *Surf. Science*, 606, 74-78 (2012b).

Cho, H., Yu, M.-F., Vakakis, A. F., Bergman, L. A., McFarland, D. M., Tunable, Broadband Nonlinear Nanomechanical Resonator, *Nano Lett.*, 10, 1793-1798 (2010).

Chotorlishvili, L., Ugulava, A., Mchedlishvili, G., Komnik, A., Wimberger, S., Berakdar, J., Nonlinear Dynamics of Two Coupled Nano-electromechanical Resonators, *J. Phys. B*, 44, 215402 (2011).

Eichler, A., Moser, J., Chaste, J., Zdrojek, M., Wilson-Rae, I., Bachtold, A., Nonlinear Damping in Mechanical Resonators Made from Carbon Nanotubes and Graphene, *Nature Nanotech.,*, 6, 339-342 (2011).

Garcia, R., *Amplitude Modulated Atomic Force Microscopy, Ch 4: Theory of Amplitude Modulation AFM,* Wiley-VCH (2010).

Gouttenoire, V., Barois, T., Perisanu, S., Leclercq, J.-L., Purcell, S. T., Vincent, P., Ayari, A., Digital and FM Demodulation of a Doubly Clamped Single-Walled Carbon-Nanotube Oscillator: Towards a Nanotube Cell Phone, *Small*, 9, 1060-1065 (2010).

Guerra, D. N., Imboden, M., Mohanty, P., Electrostatically Actuated Silicon-based Nanomechanical Switch at Room Temperature, *Appl. Phys. Lett.*, 93, 033515 (2008).

Jensen, K., Kim, K., Zettl, A., An Atomic-Resolution Nanomechanical Mass Sensor, *Nature Nanotech.*, 3, 533–536 (2008).

Jensen, K., Weldon, J., Garcia, H., Zettl, A. Nanotube Radio, *Nano Lett.,* 7, 3508–3511 (2007).

Jeong, B., Cho, H., Yu, M.-F., Vakakis, A., McFarland, D. M., Bergman, L.A.; Modeling and measurement of geometrically nonlinear damping in a microcantilever-nanotube system, *ACS Nano*, 10, 8547-8553 (2013).

Karabalin, R. B., Lifshitz, R., Cross, M. C., Matheny, M. H., Masmanidis, S. C., Roukes, M. L., Signal Amplification by Sensitive Control of Bifurcation Topology, *Phys. Rev. Lett.*, 106, 094102 (2011).

Lifshitz, R., Cross, M. C., Nonlinear Dynamics of Nanomechanical Resonators. In *Nonlinear Dynamics of Nanosystems*; Radons, G., Rumpf, B., Schuster, H. G., J. Wiley & Sons (2010).

Nayfeh, A.H., Mook D., *Nonlinear Oscillations*, Wiley Interscience (1995).

Rhoads, J. F., Shaw, S. W., Turner, S. W., Nonlinear Dynamics and Its Applications in Micro- and Nanoresonators," *J. Dyn. Syst. Meas. Control,* 132, 034001 (2010).

Rugar, D., Budakian, R., Mamin, H.J., Chui, B. W., Single spin detection by magnetic resonance force microscopy, *Nature*, 430, 329-332 (2004).

Steele, G. A., Hüttel, A. K., Witkamp, B., Poot, M., Meerwaldt, B., Kouwenhoven, L. P., van der Zant, H. S. J., Strong Coupling between Single-Electron Tunneling and Nanomechanical Motion, *Science*, 325, 1103–1107 (2009).

Vakakis, A.F., Gendelman, O., Bergman, L.A., McFarland, D.M., Kerschen, G., Lee, Y.S., *Passive Nonlinear Targeted Energy Transfer in Mechanical and Structural Systems: I and II*, Springer Verlag (2008).

Vyas, A., Peroulis, D., Bajaj, A. K., A Microresonator Design Based on Nonlinear 1:2 Internal Resonance in Flexural Structural Modes, *J. Microelectromech. Syst.*, 18, 744-762 (2009).

Vyas, A., Peroulis, D., Bajaj, A. K., Dynamics of a Nonlinear Microresonator Based on Resonantly Interacting Flexural-torsional Modes, *Nonl. Dyn.*, 54, 31-52 (2008).

Zaitsev, S., Shtempluck, O., Buks, E., Gottlieb, O., Nonlinear Damping in a Micromechanical Oscillator, *Nonl. Dyn.*, 67, 859-883 (2012).

Chapter 3

Nonlinear Microcantilever Coupled to a Nanotube Attachment[1]

3.1 Introduction

The advances in nanotechnology in the last decade have brought the development of various nanomechanical systems, among which nanomechanical resonators represent notable ones. Nanoresonators fabricated by integrating components such as carbon nanotubes and graphene membranes have readily shown high resonant frequency and high *Q*-factor performance owing to the nanoscale dimension, and the high mechanical strength and low density of the nanostructures serving as their critical mechanical elements (Poot *et al.*, 2012). As a result, various related devices have been developed for many applications, such as for ultra-sensitive mass detection (Chiu *et al.*, 2008; Jensen *et al.*, 2008; Cho *et al.*, 2010), atom-absorption sensing (Wang *et al.*, 2010), ultra-high-frequency electrical circuitry (Jensen *et al.*, 2007; Gouttenoire *et al.*, 2010), as well as for the fundamental study of the quantum limit of vibration modes (Lassagne *et al.*, 2009; Steele *et al.*, 2009; Laird *et al.*, 2011).

While most of the current studies on nanomechanical resonators focus on the study of linear resonance that takes advantage of the unique mechanical and linear dynamic properties of nanowires and nanotubes, in this study we introduce a uniquely designed

[1] B. Jeong, H. Cho, M.-F. Yu, A.F. Vakakis, D.M. McFarland, L.A. Bergman, Modeling and Measurement of Geometrically Nonlinear Damping in a Microcantilever-Nanotube System, *ACS Nano*, Vol. 7, No. 10, 8547–8553 (2013).

microcantilever system with strong intentional nonlinearity in the form of an attached ultraflexible nanotube. Although nonlinear dynamic behavior can be conveniently realized in a micro/nanocantilever system through various physical mechanisms (*e.g.*, nonlinear electrostatic actuation), in the system considered in this Chapter the realization of intrinsic nonlinearity is achieved in complete absence of any external nonlinear potential, and is caused exclusively by large-amplitude oscillations of the micro/nanocantilever system beyond the regime of validity of linear elastic response. Our aim is to develop a typical microcantilever system with dimensions and operating conditions similar to those widely used in scanning probe microscopy, but with the important (and distinctive) added feature of strongly nonlinear dynamic behavior leading to broadband resonance even at relatively small drive amplitudes. Hence, this is the first of the systems considered in this Dissertation where constructive implementation of intentional strong nonlinearity is presented.

In the following exposition, we show by employing both experiment and modeling that both the geometry of the system configuration and the kinematics of the system are responsible for the nonlinear dynamic behavior of this flexible micro/nanoresonator. We further discover that in order to account for the observed mechanical damping behavior of the system, we must take into consideration nonlinear damping in our model development. This damping nonlinearity is caused by the flexible oscillation of the nanotube and is beside the typical linear structural damping that is inherent in this nanoscale structure. Indeed, the geometric nonlinearity of the dynamic response amplifies the nonlinear damping associated with the tensile stretching of the nanotube, and contributes to the overall nonlinear damping behavior of the integrated microcantilever – nanotube system. We show

that the existence of this nonlinear damping behavior, which is amplitude-dependent, results in the narrowing of the broadband resonance of this strongly nonlinear system.

Hence, the designed microcantilever system can serve both as a practical nonlinear resonance system for sensing-related applications, and also as a testing platform for directly studying the nonlinear damping behavior of individual nanostructures. In addition, it provides a further example where *local* nonlinearity of an attached flexible nanocomponent can significantly affect the *global* dynamics of the microscale structure to which it is attached. Moreover, the methodology developed in this Chapter can be extended to study the nonlinear damping properties of similar components such as graphene or silicon nanomembranes and different types of nanotubes and nanowires.

3.2 Theoretical Analysis

3.2.1. System Description

Figure 3.1a shows the scanning electron microscope (SEM) images of the nonlinear microcantilever fabricated for incorporating significant geometrical nonlinearity. An inner paddle was carved out in a rectangular cantilever structure to create an inner cantilever having its free end close to the fixed base of the overall structure. It is expected (and later demonstrated in our modeling result) that when the microcantilever system is driven through base excitation to resonate near one of its bending modal frequencies, the free end of the inner paddle can exhibit a large vertical (out-of-plane) displacement relative to the

fixed base located just across a small gap. To introduce intentional strong nonlinearity, a single boron nitride nanotube (BNNT) is attached across this gap as shown in the inset in Figure 3.1a. This local modification of the microcantilever structure alters the relation between the overall force acting on the structure and its resulting transverse deformation, and introduces strong geometric and kinematic nonlinearity due to the involvement of the axial stretching of the nanotube in the dynamic mechanical resonance of the system (Anderson *et al.*, 2012; Cho *et al.*, 2012). A harmonic base excitation is provided to the system through electromechanical actuation.

Figure 3.1b represents the simplified, lumped-parameter model of the nonlinear microcantilever system. Considering that the microcantilever structure is geometrically large compared to the attached nanotube, the contribution of the nanotube mass to the overall mass of the system can be neglected; hence, it is assumed that the nanotube is merely subjected to longitudinal deformation, taking into account that it is relatively soft in transverse deformation but relatively stiff in axial deformation. In the model, the vertically attached parallel spring and damper represent the microcantilever structure in its second (linear) bending mode in the absence of the nanotube attachment. This mode is selected over the first mode of the system, since it corresponds to relatively large-amplitude displacements between the tip of the inner cantilever and the rigid base of the nanotube, and hence, to relatively large axial deformations of the attached nanotube; this is important in order to magnify as much as possible the geometrically nonlinear effects generated by the deformation of the oscillating nanotube. The nanotube itself is modeled as a massless system of a linear spring in parallel with a viscous damper, which is attached horizontally

between the mass and the ground. Here, the point near the base where the nanotube is anchored is modeled as the rigid ground because that point is nearly stationary. The mass moves along the *x*-axis, denoting the out-of-plane displacement of the free end of the inner paddle. As the mass moves in the *x*-direction, the force *T* is exerted on the microcantilever by the horizontally attached nanotube

3.2.2. EQUATION OF MOTION

In the lumped-parameter model depicted in Figure 3.1b, it is assumed that (i) the vertical deflection of the microcantilever is small enough so that in the absence of the attached nanotube its response is linear, (ii) its deflection is small enough to be approximated as a pure vertical displacement, (iii) the attached nanotube experiences only axial deformation, and (iv) the mass of the nanotube is negligible compared to that of the microcantilever. The governing equation of motion based on the given model is then expressed as,

$$m\ddot{x} + c_1\dot{x} + k_1 x + T\sin\theta = F_0\cos\omega t \tag{3-1}$$

where m, c_1 and k_1 are the effective mass, effective damping coefficient and effective stiffness of the microcantilever when it oscillates in its second (linear) bending mode; and $T\sin\theta$ is the vertical component of the axial force acting on the nanotube due to the vertical displacement of the microcantilever. The lateral component of T is neglected because of the assumption that the effective mass moves only in the *x*-direction. As in a similar analysis performed in previous works (Anderson *et al.*, 2012; Cho *et al.*, 2012), the axial deformation δ of the nanotube is:

$$\delta = \sqrt{L^2 + x^2} - L \tag{3-2}$$

In Eq. (3-2) L is the suspended length of the nanotube. The derivation of the axial force T starts by assuming that the nanotube is composed of linear viscoelastic material obeying the classic Kelvin-Voigt stress-strain relationship,

$$\sigma_n = E\varepsilon_n + \eta\dot{\varepsilon}_n \tag{3-3}$$

where σ_n is the stress, ε_n the strain, and E, η the Young's modulus and viscoelastic damping coefficient of the material of the nanotube, respectively. As $\sigma_n = T/A$ and $\varepsilon_n = \delta/L$, where A is the cross-sectional area of the nanotube, Eq. (3-3) is further expressed as:

$$T = \frac{EA}{L}\delta + \frac{\eta A}{L}\dot{\delta} \tag{3-4}$$

Applying Eq. (3-2) and its first derivative with respect to the time t (*i.e.*, $\dot{\delta} = x\dot{x} / \sqrt{L^2 + x^2}$) to Eq. (3-4) yields,

$$T = k_2\delta + c_2\dot{\delta} = k_2\left(\sqrt{L^2 + x^2} - L\right) + c_2\left(\frac{x\dot{x}}{\sqrt{L^2 + x^2}}\right) \tag{3-5}$$

where k_2 and c_2 are the axial stiffness and the viscous damping coefficient of the nanotube, respectively, and are expressed as:

$$k_2 = \frac{EA}{L},\ c_2 = \frac{\eta A}{L} \tag{3-6}$$

Noting that $\sin\theta = x / \sqrt{L^2 + x^2}$ from the geometry of the system, $T\sin\theta$ is expressed as:

$$T\sin\theta = k_2\left(x - \frac{Lx}{\sqrt{L^2 + x^2}}\right) + c_2\left(\frac{x^2\dot{x}}{L^2 + x^2}\right) \tag{3-7}$$

Expanding Eq. (3-7) in Taylor series about the equilibrium point x= 0 with the assumption that $x << L$, we get an approximate expression for $T\sin\theta$:

$$T\sin\theta = \frac{k_2}{2L^2}x^3 + \frac{c_2}{L^2}x^2\dot{x} + O(x^4) \tag{3-8}$$

By substituting Eq. (3-8) to Eq. (3-1) and neglecting higher-order terms, the final form of the equation of the motion can be derived as,

$$m\ddot{x} + c_1\dot{x} + k_1x + k_3x^3 + c_3x^2\dot{x} = F_0\cos\omega t \tag{3-9}$$

where a set of new parameters is introduced for simplicity, namely, $k_3 = k_2 / 2L^2$ and $c_3 = c_2 / L^2$. The final form of the equation of motion reveals that the integrated nanotube introduces geometric and kinematic nonlinearities, which are expressed through the third-order stiffness term, and the third-order damping term.

To facilitate the analysis, a normalization process is applied by introducing the following parameters in Eq. (3-9),

$$z = \frac{x}{L_0},\ \tau = \omega_0 t,\ \omega_0 = \sqrt{\frac{k_1}{m}} \tag{3-10}$$

where L_0, ω_0, τ and z are an arbitrary scaling length, the eigenfrequency (i.e., the natural frequency of the second bending mode of the linear microcantilever), the normalized time and the normalized displacement, respectively.

Then, the normalized form of Eq. (3-9) is expressed as,

$$z'' + \left(2\xi_1 + \xi_3 z^2\right)z' + z + \alpha z^3 = q_0\cos\Omega\tau \tag{3-11}$$

where the dimensionless parameters in Eq. (3-11) are defined as follows:

$$2\xi_1 = \frac{c_1}{m\omega_0},\ \xi_3 = \frac{c_3}{m\omega_0}L_0^2,\ \alpha = \frac{k_3}{k_1}L_0^2$$
$$q_0 = \frac{F_0}{k_1 L_0},\ \Omega = \frac{\omega}{\omega_0},\ (\ )' = d/d\tau \tag{3-12}$$

Here ξ_1 and ξ_3 are the normalized linear and nonlinear damping coefficients, respectively, and α is the normalized nonlinear cubic stiffness coefficient; also, q_0 and Ω are the normalized force and driving frequency, respectively.

3.2.3. MULTIPLE SCALES ANALYSIS

The method of multiple scales is employed to analytically estimate the frequency-amplitude response at the resonant mode of interest (Nayfeh and Mook, 1995). Before beginning the analysis, the parameters in Eq. (3-11) are rescaled by a small perturbation parameter $0 < \varepsilon << 1$, according to the following:

$$z \mapsto \sqrt{\varepsilon} z,\ \xi_1 \mapsto \varepsilon\xi_1,\ q_0 \mapsto \varepsilon^{3/2} q_0 \tag{3-13}$$

These rescalings denote that the oscillations of the system are of $O\left(\sqrt{\varepsilon}\right)$, the inherent structural dissipative term in the system is small (of $O(\varepsilon)$), and the applied harmonic base excitation is of $O\left(\varepsilon^{3/2}\right)$. Note that the considered system is subjected to the condition of weak linear damping ($\xi_1 \equiv 10^{-3} \sim 10^{-5}$), so it is quite reasonable to rescale ξ_1 using the small parameter $\varepsilon << 1$. The normalized oscillation amplitude, z, is then rescaled with $\varepsilon^{1/2}$ for the following reasons: (i) The approximate expansion of the nonlinear forcing terms is only

valid when the oscillation amplitude is small, so that the motion takes place close to the equilibrium position (z=0); and (ii) for consistency of the nonlinear dynamics, in our analysis we need to scale the third order terms (*i.e.*, z^3, z^2z') to be of the same order of the linear damping term which is of order ε. The normalized force constant, q_0, is also rescaled by $\varepsilon^{3/2}$ since it should be sufficiently small to give rise to small-amplitude oscillations. In addition, we note that the oscillation amplitude in the corresponding linear dynamical system is proportional to the magnitude of the force and the Q-factor (which is in the order $\varepsilon^{1/2}$ in the current rescaling postulation, that is, identical to the order of the rescaled z) (Lifshitz *et al.*, 2010).

The aforementioned set of rescaled parameters results in the following rescaled equation of motion:

$$z'' + 2\varepsilon\xi_1 z' + z + \varepsilon\xi_3 z^2 z' + \varepsilon\alpha z^3 = \varepsilon q_0 \cos\Omega\tau \tag{3-14}$$

In order to restrict the frequency of excitation to the neighborhood of resonance of the microcantilever mode of interest (the second linear bending mode), the normalized resonant frequency is modified by means of a frequency detuning parameter σ:

$$\Omega = 1 + \varepsilon\sigma \tag{3-15}$$

Then the multiple scales $T_n = \varepsilon^n \tau,\ n = 0,1,2,\ldots$ are introduced, denoting the different coexisting slow and fast dynamical processes that take place in the nonlinear response. In this context, T_0 represents the fast time scale and $T_n,\ n \geq 1$ the slow time scales, which become increasingly slower as the order n increases.

According to the method of multiple-scales the different time scales are treated as independent temporal variables, and the steady state response of the microcantilever is expressed in the following series form,

$$z(\tau;\varepsilon) = z_0(T_0, T_1, ...) + \varepsilon z_1(T_0, T_1, ...) + O\left(\varepsilon^2\right) \tag{3-16}$$

where the derivatives with respect to the normalized time (τ) are expressed in terms of the new time scales by the chain rule as follows,

$$\begin{aligned} d/d\tau &= \partial/\partial T_0 + \varepsilon\, \partial/\partial T_1 \equiv D_0 + \varepsilon D_1, \\ d^2/d\tau^2 &= \partial^2/\partial T_0^2 + 2\varepsilon\, \partial^2/\partial T_0 \partial T_1 + O\left(\varepsilon^2\right) \equiv D_0^2 + 2\varepsilon D_0 D_1 + O\left(\varepsilon^2\right) \end{aligned} \tag{3-17}$$

Substituting Eqs. (3-15) – (3-17) into (3-14) results in a nonlinear ordinary differential equation in terms of the small parameter ε, enabling the formulation of a hierarchy of sub-problems by matching coefficients of respective powers of ε.

At *O(1)*, the following equation is obtained,

$$O(\varepsilon^0): D_0^2 z_0 + z_0 = 0 \tag{3-18}$$

leading to the leading-order approximation of the steady state solution:

$$z_0 = A(T_1) e^{jT_0} + c.c. \tag{3-19}$$

In Eq. (3-19), $A(T_1)$ represents the slowly varying complex modulus of the amplitude with respect to slow time scale T_1 and *c.c.* is the abbreviation for the complex conjugate of the first term. By its form, this leading-order approximation denotes a slow/fast partition of the dynamics in terms of a fast oscillation with unit normalized frequency modulated by the slowly-varying complex envelope $A(T_1)$. This complex amplitude cannot be

determined at this order of approximation, and in order to compute it we need to consider the subproblem at the next order of approximation.

Accordingly, considering $O(\varepsilon^1)$ terms, we derive the equation for the second-order approximation as follows:

$$O(\varepsilon^1): D_0^2 z_1 + z_1 = -2D_0 D_1 z_0 - 2\xi_1 D_0 z_0 - \xi_3 z_0^2 D_0 z_0 - \alpha z_0^3 + q_0 \cos(T_0 + \sigma T_1) \tag{3-20}$$

Eq. (3-19) is then substituted to Eq. (3-20), and the coefficient of e^{jT_0} on the right-hand side is set equal to zero in order to eliminate the resulting secular term. This term is proportional to the fast normalized frequency equal to unity, and, if not eliminated, it can lead to non-uniformly valid solutions of (3-20) due to resonance. Hence, the following complex modulation equation governing the slow modulation of the amplitude of the leading order approximation is derived,

$$2jA' + 2j\xi_1 A + j\xi_3 A^2 \bar{A} + 3\alpha A^2 \bar{A} - \frac{1}{2} q_0 e^{j\sigma T_1} = 0 \tag{3-21}$$

which represents the complex *slow flow dynamics* of the response. Expressing the complex modulus of the amplitude in polar form,

$$A(T_1) = \tfrac{1}{2} A_0 e^{j\beta} \tag{3-22}$$

substituting into Eq. (3-21) and setting the real and imaginary parts of the resulting equations separately equal to zero, one obtains a set of real autonomous modulation equations, which represents the slow flow system in real coordinates:

$$
\begin{aligned}
A_0' &= -\xi_1 A_0 - \frac{\xi_3}{8} A_0^{\,3} + \frac{q_0}{2}\sin\gamma \\
A_0\gamma' &= A_0\sigma - \frac{3}{8}\alpha A_0^{\,3} + \frac{q_0}{2}\cos\gamma \\
\gamma &= \sigma T_1 - \beta
\end{aligned}
\tag{3-23}
$$

Here, γ is the phase difference between the excitation and the steady state response. Eq. (3-23) provides the steady state time-periodic response of the nonlinear model by assuming that the amplitude and the phase difference are constant ($A_0' = 0$ and $\gamma' = 0$), thus leading to the following frequency-amplitude relation at steady state,

$$
\left[\left(\xi_1 + \frac{\xi_3}{8} A_{ss}^{\,2}\right)^2 + \left(\sigma - \frac{3}{8}\alpha A_{ss}^{\,2}\right)^2\right] A_{ss}^{\,2} = \left(\frac{q_0}{2}\right)^2 \tag{3-24}
$$

where A_{ss} denotes the steady state amplitude.

It is well known (Nayfeh and Mook., 1995; Vakakis *et al.*, 2008) that the free oscillations of the corresponding Hamiltonian system (*i.e.*, the system with no damping or forcing terms) possess frequencies that depend on the amplitude of oscillations. This amplitude-frequency relationship can be depicted in the 'backbone' curve which does not depend on the level of forcing or the level of (linear and nonlinear) damping since it is a feature of the underlying Hamiltonian system. Yet, as pointed out in the literature (Vakakis *et al.*, 2008), for weak damping the corresponding forced and damped steady state response is expected to occur in the neighborhood of the Hamiltonian backbone branch. Consequently, Eq. (3-24) can produce the backbone curve equation for the underlying Hamiltonian system by setting the damping factors and the external force to zero

($\xi_1 = \xi_3 = q_0 = 0$) and analyzing the dependence of the amplitude of free oscillation with respect to the corresponding frequency:

$$A_{ss} = \left(\frac{8\sigma}{3\alpha} \right)^{1/2} \tag{3-25}$$

This is useful for anticipating the steady state responses and the drop (jump) frequencies at different excitation amplitudes and damping levels.

3.2.4. NONLINEAR DAMPING EFFECT

From Eq. (3-24), we can define an effective damping ratio coefficient ξ_{eff} through the relationship,

$$\xi_{eff} = \xi_1 + \frac{\xi_3}{8} A_{ss}^2 = \frac{1}{2}\left(\frac{1}{Q_0} + \frac{1}{Q_{nl}} \right) = \frac{1}{2Q_{eff}} \tag{3-26}$$

where Q_0 is the Q-factor for the linear damping term, $Q_{nl}^{-1}/2$ is the damping effect contributed by the nonlinear damping effect, and $Q_{eff}^{-1}/2$ is the representative overall damping of the system. In writing (3-26) we fitted an equivalent linear viscous damping model to the nonlinear dissipation effect, in order to derive an equivalent (effective) viscous damping ratio. It should be noted that Q_{nl} and Q_{eff} represent the nonlinear and overall effective Q-factors, respectively, adopted from the general linear concept of Q-factor (*i.e.*, $Q_0 = 1/(2\xi_1)$), in order to obtain a better quantitative measure of the contribution of the nonlinear damping term to the overall dissipation, compared to the linear damping term which is expected to persist in the dynamics independent of the energy and pressure

level. In our system, Q_0 arises from the viscous effect exerted on the microcantilever by the surrounding ambient gaseous environment and the intrinsic damping of the beam itself, whereas Q_{nl} arises due to geometric and kinematic nonlinearities; that is, it originates from the intrinsic nonlinear damping characteristic of the attached nanotube during the oscillation.

Applying Eq. (3-26) to Eq. (3-24) leads to the following expression, which relates the steady amplitude of forced oscillation with the magnitude of the excitation and the frequency detuning σ:

$$\left[\left(\frac{1}{2Q_{eff}}\right)^2+\left(\sigma-\frac{3}{8}\alpha A_{ss}{}^2\right)^2\right]A_{ss}{}^2=\left(\frac{q_0}{2}\right)^2 \tag{3-27}$$

Note that Eq. (3-27) has an identical form to that frequency-amplitude relation of a dynamic system with pure linear damping. One can thus employ the same approach as in the linear-damping case to extract Q_{eff} from the experimental result. Once the drop frequency and the resonant frequency are known from the dynamic response, and the other parameters are extracted by the methodology which will be elaborated in Section 3.4.2. It follows that Q_{eff} can be also estimated from the equation:

$$Q_{eff}=\left(\frac{8\sigma_{drop}}{3\alpha q_0^2}\right)^{1/2} \tag{3-28}$$

Eq. (3-28) can be derived by computing the intersection between the steady state solution derived from (3-27) and the backbone curve equation from (3-28). Once Q_{eff} is estimated from the experimental data, Q_{nl} can be found by Eq. (3-28) using the measured Q_0 at each level of vacuum pressure.

3.3 Device Fabrication

A series of experimental tests was performed in order to apply the aforementioned methodology. To this end an experimental fixture was constructed and dynamical experiments were conducted at different ambient conditions. The basic component of the experimental fixture, the nonlinear microcantilever system, was fabricated by modifying a commercially available AFM cantilever (Mikro-Masch, NSC-14). The inner paddle was carved out with a focused ion beam (FIB) based machining process. A multi-walled boron nitride nanotube was then manipulated and deposited across the gap by nanomanipulation inside an SEM, and was subsequently fixed on both ends through an electron beam induced platinum deposition process.

3.4. Experimental Results

3.4.1. Experimental Setup

The fabricated microcantilever system was mounted on a small piezoelectric stack and actuated by the piezoelectric stack with an applied sinusoidal signal of amplitude V_{pp}. The dynamic response of the microcantilever system was measured by a laser microvibrometer system (Polytec UHF-120 ultra high frequency vibrometer with bandwidth up to 1.2 GHz) with the laser light focused on the center of the inner paddle. During the measurement, the frequency was swept up and then down to acquire the full response spectrum. To investigate the effective damping of the overall system (which, as discussed above,

includes both linear and nonlinear components), the system was placed in a vacuum chamber where the vacuum pressure (P) was varied from 750 Torr down to 4.5 mTorr in order to realize the different ambient conditions necessary for the experiment. The ambient environment for the experimental tests ranged from ambient air pressure to conditions of high vacuum.

3.4.2. NONLINEAR FREQUENCY RESPONSE

Figure 3.2 shows the experimentally acquired response spectrum for a microcantilever system driven with an AC excitation amplitude of 1.5 V and at a vacuum pressure P of 4.5 mTorr. Note that our initial measurement of the first two bending modes of the system revealed that the free end of the inner paddle produced greater displacement relative to the neighboring point across the gap in the second bending mode than that in the first bending mode when driven with the same V_{pp}. We thus chose the second bending mode in our study in order to involve the stronger geometric nonlinearity due to the tensile stretching of the nanotube. As seen from the acquired response spectrum, abrupt transitions are observed between the upper and lower stable branches as a result of the nonlinear hysteresis, indicating the existence of strong geometric stiffness nonlinearity induced by the nanotube attachment.

The experimentally obtained results were compared with the results from the theoretical model developed previously. The inset of Figure 3.2 shows the measured response curve at increasing excitation amplitude V_{pp}. With the increase of V_{pp}, the

frequency band of resonant operation widens, and the drop frequency increases. The amplitude values at the drop frequency in these response curves fit precisely into the so-called 'backbone' curve (Eq. (3-25)). The nonlinear stiffness constant α and linearized resonant frequency f_0 in Eq. (1) were obtained through this fitting, which gave $\alpha = 8.52 \times 10^{-7}$ and $f_0 = 273.046$ kHz.

We then fit the whole response curve as shown in Figure 3.2 with our model result (*i.e.*, Eq. (3-24)). The dimensionless force constant, q_0, was extracted from fitting the response curve acquired at an ambient pressure environment (P = 750 Torr), where the nonlinear damping effect was negligible, because the amplitude of oscillation of the microcantilever was small due to strong (linear) viscous damping caused by the surrounding gaseous environment and intrinsic damping; in this case q_0 is measured to be 1.88×10^{-2} at a drive amplitude of V_{pp}=1.5 V. The effective damping coefficient was found to be $\xi_{eff} = 1.65 \times 10^{-4}$ (Q_{eff} = 3036) by fitting Eq. (3-24) (after applying Eq. (3-26)) to the response curve acquired at a vacuum pressure of 4.5 mTorr and at an excitation amplitude of 1.5 V. The fitting produced response curves that matched the experimental result quite well as shown in Figure 3.2.

3.4.3. ESTIMATION OF NONLINEAR DAMPING COEFFICIENT

We performed similar fitting procedures to extract the effective Q factor for a series of response curves acquired at different vacuum pressures and at different excitation amplitudes. The results are summarized in Figure 3.3a, in which we plot Q_{eff} as a function

of the vacuum pressure under four different drive amplitudes V_{pp}. Q_0 is defined in Eq. (3-26) and represents the contribution from the linear damping (such as the hydrodynamic viscous damping and the intrinsic thermoelastic damping). Q_{nl}, as defined in Eq. (3-26), represents the contribution from the nonlinear damping and is an amplitude-dependent quantity.

As expected, $Q_{nl}^{-1} << Q_0^{-1}$ when the device is resonating at small amplitude and the dynamic response is almost purely linear. For example, at an excitation of V_{pp}=0.1 V, the maximum oscillation amplitude reaches only to around a few nanometers even at high vacuum pressure; Q_{nl}^{-1} is thus negligible so $Q_{eff} \approx Q_0$. The measure of Q_0 as a function of the vacuum pressure acquired at a small excitation amplitude (*i.e.*, V_{pp}=0.1 V) is plotted in Figure 3.3a. It is noteworthy that the variation of Q_0 reveals the existence of three distinct linear or nonlinear dissipation regimes for varying level of vacuum pressure: Starting from the viscously damped regime at the level of high pressure (Kn<0.01, P>~100 Torr) where the linear dissipative effects are dominant, to the intermediate regime (0.01≤Kn≤10), and consequently transitioning to the free molecular flow regime as the vacuum pressure decreases (Kn>10, P<~0.1 Torr) (Bhiladvala *et al.*, 2004; Verbridge *et al.*, 2008). At large excitation amplitudes (where the oscillation amplitude of the inner cantilever can reach up to around 60 nm), the effective Q factor Q_{eff} decreases and saturates toward higher vacuum pressure.

The vacuum pressure is experimentally controlled within $\pm$10%, which, however, can introduce a certain degree of data scattering in the measured linear Q-factor (Q_0). We

generated a fitting function for the measured Q_0 as a function of vacuum pressure to smooth out the data scattering, as shown in Figure 3.4. The fitted function is defined as follows,

$$Q_0(P) = \frac{p_1}{\sqrt{P}} + \frac{p_2}{P} + \frac{p_3}{\sqrt{P - p_4}} + \frac{p_5}{P - p_6} \tag{3-29}$$

where the numerical values of the coefficients of the fit are given by:

$$p_1 = 1.3127 \times 10^2,\ p_2 = -4.9182,\ p_3 = 1.0627 \times 10^4$$
$$p_4 = -1.6113 \times 10^2,\ p_5 = 6.4786 \times 10^3,\ p_6 = -1.5174$$

Note that the fitted function (3-29) is developed relying on the understanding that the dependence of Q_0 on vacuum pressure typically exhibits the aforementioned three regimes reflecting the different physical mechanisms present in the experimental tests at different ambient conditions (Verbridge *et al.*, 2008).

Based on Eq. (3-29), Figure 3.3a is converted to Figure 3.3b where Q_{eff} is plotted against the corresponding Q_0. For reference, we performed the same measurement using the same microcantilever system without the nanotube attachment, and driven with the same set of excitation amplitudes and under the same set of vacuum pressures. The extracted Q_{eff} is plotted against Q_0 as shown in the inset in Figure 3.3b, exhibiting a completely linear damping response across the full range of the pressure and excitation amplitude variations, and showing no dependence on the oscillation amplitude as expected for a linear resonator. This underscores the necessity to model the mechanisms of nonlinear damping discussed previously.

Furthermore, the results demonstrate the critical importance of incorporating the nonlinear damping contribution into our nonlinear microcantilever resonance system. We

proceed to extract the nonlinear damping coefficient ξ_3 (*i.e.*, Q_{nl}^{-1}) based on Eq. (3-26). Figure 3.3c shows the dependence of the extracted Q_{nl}^{-1} as function of the amplitude at the drop frequency (A_{drop}) measured from the acquired response curves at an excitation amplitude of V_{pp}=1.5 V and at varying vacuum pressures. Recalling that $Q_{nl}^{-1} = \xi_3 A_{ss}^2 / 4$ according to Eq. (3-26), ξ_3 was estimated to be 2.1×10^{-7} by fitting the measured data in Figure 3.3c. As ξ_3 is directly linked to c_2 which is associated with the intrinsic viscoelastic property of the nanotube, it is reasonably expected that ξ_3 is also an intrinsic property and independent of the dynamics of our microcantilever system. This is confirmed by the excellent fit in Figures 3.3a,b between the experimental data and the solid fitting curves obtained by assuming the same estimated value of ξ_3, even though the experimental data are acquired at varying vacuum pressures and excitation amplitudes.

The saturation of Q_{eff} towards high vacuum pressures can thus be easily understood from the consideration of the linear and nonlinear damping mechanisms that co-exists in the experimental system. Indeed, towards high vacuum pressure operation the linear damping decreases (or the energy dissipation by linear damping becomes smaller), which leads to an increase of the oscillation amplitude. However, the increase of the oscillation amplitude aggravates the nonlinear damping effect through its amplitude-dependence. This counterbalance leads to the eventual saturation of Q_{eff} towards high vacuum pressures. This Q-factor saturation is also expected to occur in some recent studies on clamped-clamped nanoresonators (Sazanova *et al.*, 2004; Witkamp *et al.*, 2006; Garcia-Sanchez *et al.*, 2007;

Bunch *et al.*, 2007; Garcia-Sanchez *et al.*, 2008; Shivaraman *et al.*, 2009; Chen *et al.*, 2009; Singh *et al.*, 2010; Huttel *et al.*, 2009), although it was not directly reported in those studies.

3.4.4. FREQUENCY BANDWIDTH RESTRICTION

The existence of nonlinear damping also affects the bandwidth of the resonance operation of our nonlinear microcantilever system. Figure 3.5 shows the measured drop frequency (solid symbols) as function of vacuum pressure at various excitation forces. This drop frequency is defined as the frequency at which the bi-stability transition occurs and the oscillation abruptly transits to the lower stable branch during the forward frequency sweeping. Based on these measurements we define the resonance bandwidth as $\Delta f = f_{drop} - f_0$.

To validate that our model can predict the drop frequency depicted in Figure 3.5, the analytical expression for the drop frequency f_{drop} should be derived. The drop frequency is located where the steady state solution and the backbone curve equation intersect. Once the nonlinear damping coefficient ξ_3 is identified, along with the other parameters such as the linear damping coefficient and the force amplitude, one can analytically predict the frequency where the jumping from the higher branch to the lower branch will occur. The derivation for the drop frequency begins with substituting Eq. (3-25) into Eq. (3-24) in order to find the intersection, which results in the following relationship:

$$\left[\left(\xi_1 + \frac{\xi_3}{8}\left(\frac{8\sigma_{drop}}{3\alpha}\right)\right)^2\right]\left(\frac{8\sigma_{drop}}{3\alpha}\right) = \left(\frac{q_0}{2}\right)^2 \tag{3-30}$$

Eq. (3-30) is a third-order polynomial equation of the drop detuning parameter, σ_{drop}. By analytically solving σ_{drop} and choosing the real solution only, we obtain the drop frequency equation as,

$$\sigma_{drop} = \alpha\left(\Gamma^{1/2}\xi_1 - \Gamma^{-1/2}\xi_3^{-1}\right)^2 \tag{3-31}$$

where Γ is defined as:

$$\Gamma = \frac{4\times 6^{1/3}}{\left(9q_0\xi_3^2 + \sqrt{3}\sqrt{128\xi_1^3\xi_3^3 + 27q_0^2\xi_3^4}\right)^{2/3}} \tag{3-32}$$

The drop frequency can be then recovered by using Eqs. (3-12), (3-15) and (3-31), and is expressed by the following expression:

$$f_{drop} = f_0\left(1+\alpha\left(\Gamma^{1/2}\xi_1 - \Gamma^{-1/2}\xi_3^{-1}\right)^2\right) \tag{3-33}$$

For the case without nonlinear damping, f_{drop} can be derived by substituting Eq. (3-25) into Eq. (3-24) with ξ_3 assumed to be zero, which gives:

$$f_{drop} = f_0\left(1+\frac{3\alpha q_0^2}{32\xi_1^2}\right) = f_0\left(1+\frac{3}{8}\alpha q_0^2 Q_0^2\right) \tag{3-34}$$

However, the resonant frequency f_0 should also vary according to the vacuum pressure. In order to determine the relation between the vacuum pressure and the resonant frequency, f_0 is measured at different vacuum pressures, and is plotted in terms of Q_0, as shown in Figure 3.6. The data points in Figure 3.6 can be fitted by the following equation,

$$f_0(Q_0) = \gamma_1\sqrt{1-\gamma_2\left(\frac{1}{2Q_0}\right)^2} \tag{3-35}$$

where the fitted parameters are found to be:

$$\gamma_1 = 273.0074, \quad \gamma_2 = 2.3919 \times 10^3 \tag{3-36}$$

The analytical value of f_{drop} (we set ξ_3=2.1 × 10^{-7}) based on Eq. (3-33), as function of the vacuum pressure for different excitation forces is plotted (as solid line) in Figure 3.5. The results again shows excellent match between the theoretical nonlinear model with the experimental results. The dashed lines in Figure 3.5 represent the estimation of the drop frequency variation when only the linear damping is considered in the analysis of the theoretical model (*i.e.*, Eq. (3-34)). This leads to the infinite increase of the drop frequency and thus the infinite expansion of the resonance bandwidth towards higher vacuum pressures (*i.e.*, when $\xi_1 \to 0$); our experimental measurements clearly are at odds with this. We can thus obtain the upper limit of the drop frequency from Eq. (3-33) by taking $\xi_1 \to 0$, $f_{drop,\max} = f_0(1 + 0.95\alpha q_0^{2/3} \xi_3^{-2/3})$, which is a finite (saturation) value as long as the nonlinear damping effect exists. This again validates the importance of the inclusion of nonlinear damping in our theoretical model consideration, especially at high vacuum pressures.

3.4.5. NONLINEAR DAMPING AS MATERIAL PROPERTY

Although the nonlinear damping effect is proven to be amplitude-dependent, with the nonlinear damping force being estimated as $\xi_3 z^2 z'$ based on a viscoelastic mechanical model of the boron nitride (BN) nanotube, it is yet still possible that there might exist other contributing factors to this nonlinear damping. As postulated by a recent study on nanotube

resonators based on a single wall nanotube and graphene sheets, besides the contribution from the viscoelastic property of the nanostructure itself, nonlinear phonon-phonon tunneling or friction at the clamps might also be significant factors (Eichler *et al.*, 2011). Some studies even estimated that the contribution from the viscoelastic model can only provide a lower bound for the overall nonlinear damping effect in such resonators (Eichler *et al.*, 2011; Zaitsev *et al.*, 2012). In the following, we compare the nonlinear damping coefficient extracted from our measurement with existing values for a single wall carbon nanotube and a multi-walled boron nitride nanotube estimated in previous studies.

The nonlinear damping constant in real units, c_3, can be recovered through the use of Eq. (3-12). In order to proceed, we need to identify the effective spring constant, k_1. An estimate for k_1 can be retrieved from the nonlinear stiffness coefficient α, but k_3 should be estimated in advance. This is performed through Eqs. (3-6) and (3-8), where k_3 can be expressed as:

$$k_3 = \frac{k_2}{2L^2} = \frac{EA}{2L^3} \tag{3-37}$$

The measured diameter of the nanotube is approximately 120 nm, whereas its length is 4 μm. The Young's modulus of the BNNT used here is 0.926 TPa (Wei *et al.*, 2010). Using these parameters, k_3 is estimated as 1.0426×10^{14} N/m^3. By using the third equation in (3-12) along with the scaling length parameter L_0=1 nm, k_1 is estimated to be 96.04 N/m. Once k_1 is identified, the effective mass m can be found by letting $\omega_0 = 2\pi f_0 = 1.715 \times 10^6$ rad/s. Based on this value of ω_0, we estimate that $m = 3.26 \times 10^{-11}$ kg. With all these parameters

defined, c_3 can be found from the relation $c_3=\xi_3 m\ \omega_0$, and its value is estimated as 1.2×10^7 kg $m^{-2}s^{-1}$.

The estimated nonlinear damping coefficient c_3 turns out to be greater by three orders of magnitude than that of a single wall carbon nanotube, which is deduced to be 1×10^4 kg $m^{-2}s^{-1}$ from a previous work (Eichler *et al.*, 2011). This, however, is to be expected as the multiwall BN nanotube we used in the experiment is considerably larger than a single wall nanotube, and more defective; besides, the interlayer sliding interactions might also contribute to its viscoelastic response in a significant way (Sawaya *et al.*, 2011). A recent study on the interlayer frictional loss in a multi-walled BNNT revealed that its energy dissipation can be estimated in a form of viscosity whose measured value was 6.7×10^6 kg $m^{-2}s^{-1}$ (Nigues, *et al.,* 2014). Notably, the reported viscosity of a multi-walled BNNT is considerably close to our estimation, thus strongly supporting our conjecture that 1) BNNT can be modeled as a viscoelastic component by the effect from the interlayer frictional loss, and 2) the proposed system can serve as a platform to be utilized for characterizing the energy dissipation in the individual nanoscale component. Nevertheless, an extensive study on individual nanoscale component is further called for to clearly discriminate their viscoelastic properties with the damping contributions of the other possible dissipative terms mentioned previously.

3.5. Conclusions

In conclusion, we have introduced a practically designed microcantilever device with strong nonlinearity even at relatively small oscillation amplitudes below 100 nm, an

operating in absence of a nonlinear external potential. We developed an analytical model with the consideration of nonlinear damping originating from the viscoelastic property of a nanotube element that was directly integrated into the device. Systematic experimental studies at various vacuum pressures and different excitation forces validated our theoretical analysis, and demonstrated the importance of the contribution of the nonlinear damping effect on the overall dynamic behavior of this nonlinear resonating micro/nanosystem. It was found that it is the critical existence of nonlinear damping that limits the potentially unrestricted expansion of the bandwidth of the nonlinear resonance of this device towards higher vacuum pressure operation, and the corresponding saturation of both the overall effective Q-factor and the drop frequency at the bi-stable resonance branch transition. The intentionally designed nonlinear micro/nanocantilever system was also found to be a useful tool for quantitatively extracting the viscoelastic properties of the individual nanocomponents (nanowires, nanotubes or nanomembranes) integrated in the system, in this case, of an individual BN nanotube. As suggested further work it would be of interest to develop this nonlinear microcantilever system for broadband scanning probe microscopy applications.

FIGURES

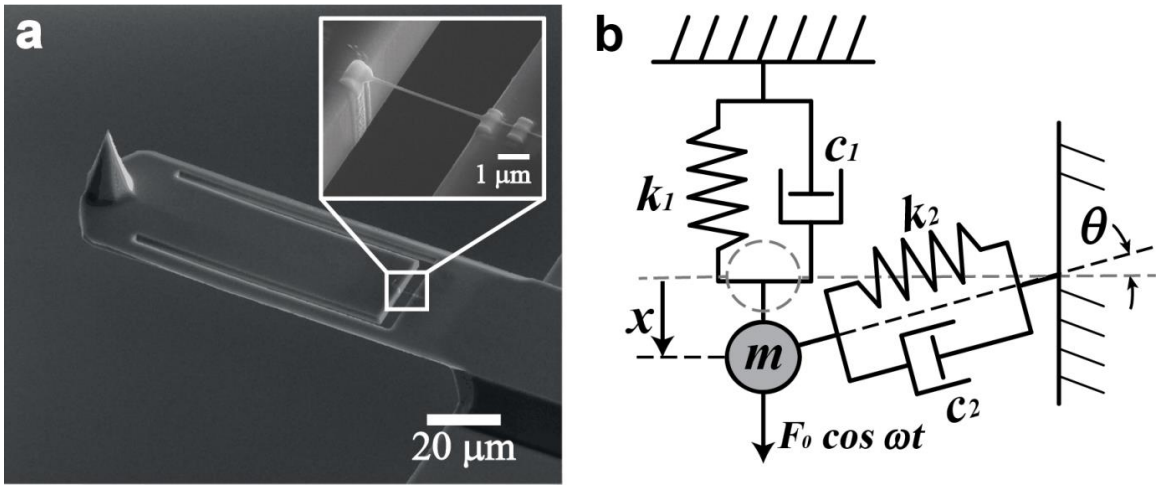

Figure 3.1. Fabricated nonlinear microcantilever and lumped-parameter model: (a) Scanning electron microscope image of the fabricated device. The microcantilever structure is 120 μm long, 40 μm wide and 2 μm thick, whereas the inner paddle is 75 μm long and 25 μm wide. The inset shows the attached BN nanotube, whose diameter and suspended length are 120 nm and 4 μm, respectively; (b) Simplified lumped-parameter model for the device. m denotes the effective mass of the system, and k_1 and c_1 represent the linear effective stiffness and the linear damping coefficient of the microcantilever, respectively. k_2 and c_2 are parameters arising from the nanotube attachment, standing for the axial stiffness and the viscous damping coefficient of the BN nanotube, respectively. The system is initially at the equilibrium position (denoted by a gray dashed line), and it moves by the displacement x once the system is subjected to the external force (to a configuration denoted by black dashed line). Consequently, the force acting on k_1 and c_1 changes linearly with x whereas the vertical portion of the force acting on k_2 and c_2 changes in accordance to the relation between x and θ, resulting in nonlinearity induced by the geometrical configuration and the kinematics.

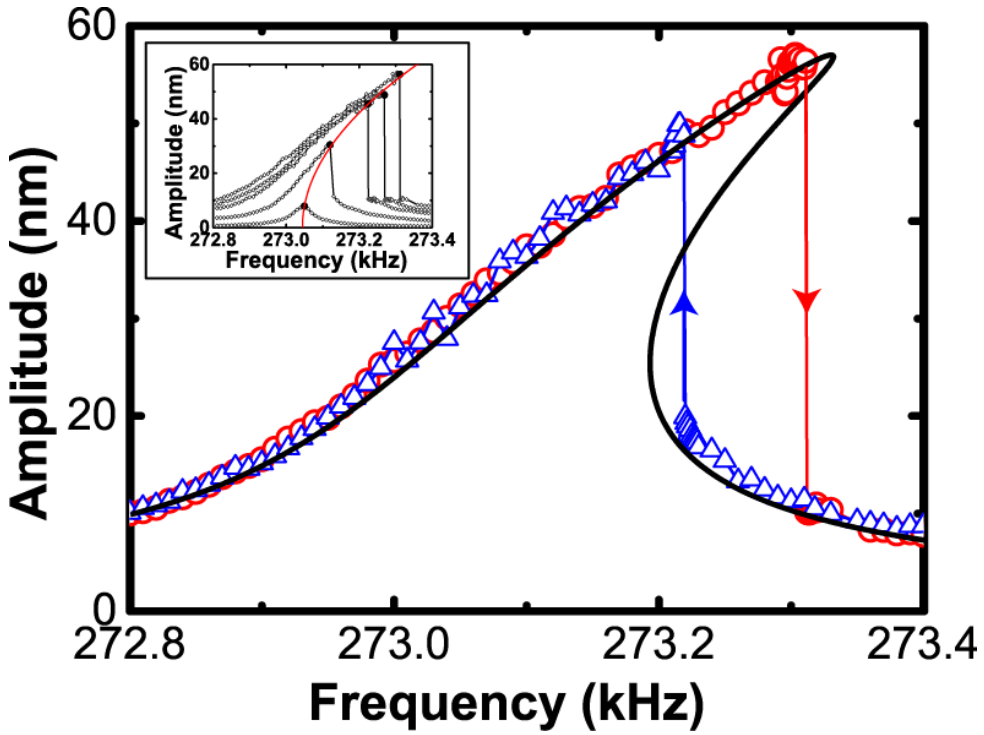

Figure 3.2. Nonlinear dynamical steady state response of the microcantilever with the attached BN nanotube. The frequency response spectrum is acquired with V_{pp}=1.5 V at a vacuum pressure of 4.5 mTorr. The red circles denote data points acquired when the frequency was swept upward (forward sweep), and the blue triangles downward (backward sweep). Due to the presence of the nonlinear stiffness, the system possesses two stable branches (*i.e.*, bi-stability) and jump phenomena occur as shown by the blue and the red arrows, resulting in nonlinear hysteresis. The black line is the analytical solution based on the extracted α, and is fitted onto the experimental measurement to extract Q_{eff}, which is found to be 3036 (ξ_{eff} = 1.65 × 10^{-4}), whereas Q_0 at V_{pp} = 0.1 V under the same vacuum pressure is 5847 (ξ_1 = 8.55 × 10^{-5}). The inset shows the corresponding nonlinear resonance curves at the same pressure level, and as the excitation amplitude was set to 0.1, 0.5, 1.0, 1.25 and 1.5 V. The amplitudes at the drop frequencies are fitted by the red line (the backbone curve), resulting in α = 8.52 × 10^{-7}.

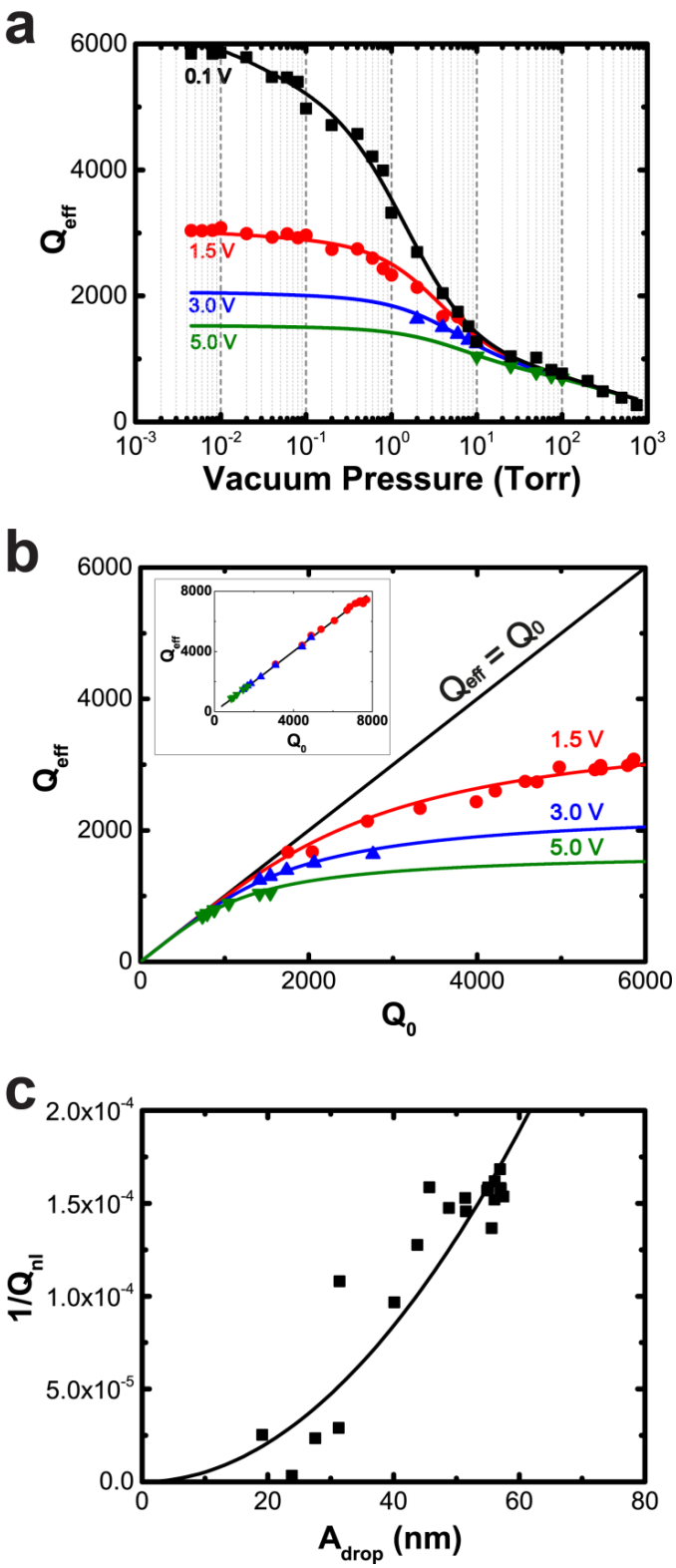

Figure 3.3. Nonlinear damping effect in the microcantilever with the attached BN nanotube: **(**a) Q_{eff} as a function of vacuum pressure. At the low excitation amplitude (V_{pp}=0.1 V), a linear damping response dominates (denoted by the black line); at higher excitation amplitude, the effective Q-factor shows saturation towards higher vacuum pressure (depicted by the red, blue and green solid lines for V_{pp}=1.5 V, 3.0 V and 5.0 V, respectively), reflecting the contribution of the nonlinear damping Q_{nl}; (b) Q_{eff} plotted against the corresponding Q_0 at each vacuum pressure; (c) Q_{nl}^{-1} as a function of the corresponding oscillation amplitude at the drop frequency (A_{drop}) when V_{pp}=1.5 V and the vacuum pressure is varied from 8 Torr to 4.5 mTorr.

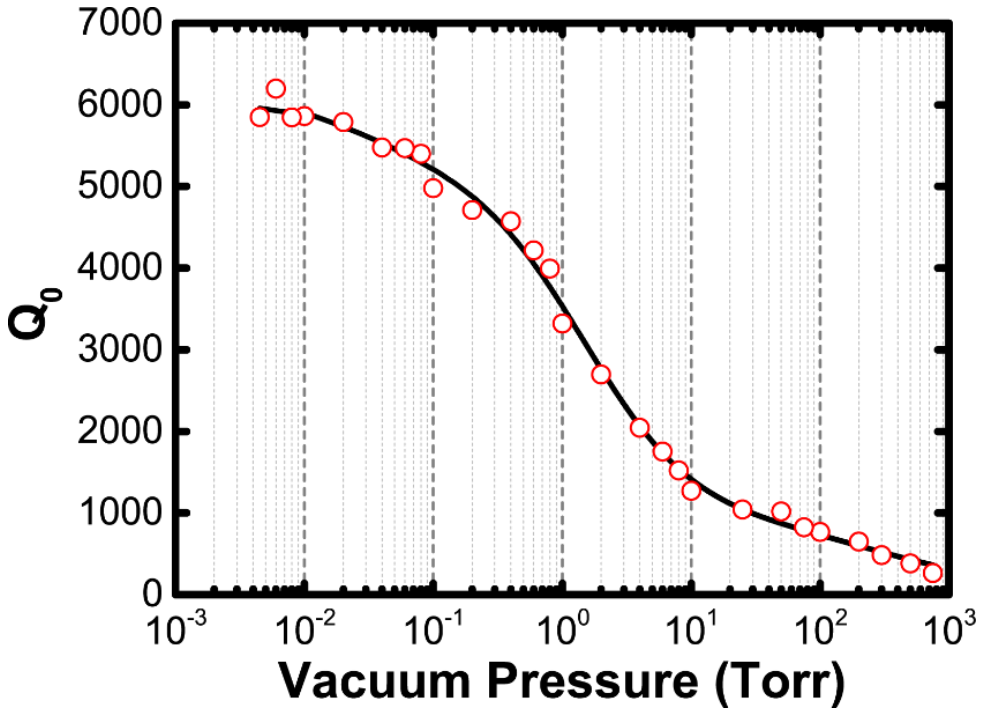

Figure 3.4. Q_0 measured at different vacuum pressures. The black solid line is the fitting to the data points (red circles) according to the function in Eq. (3-29).

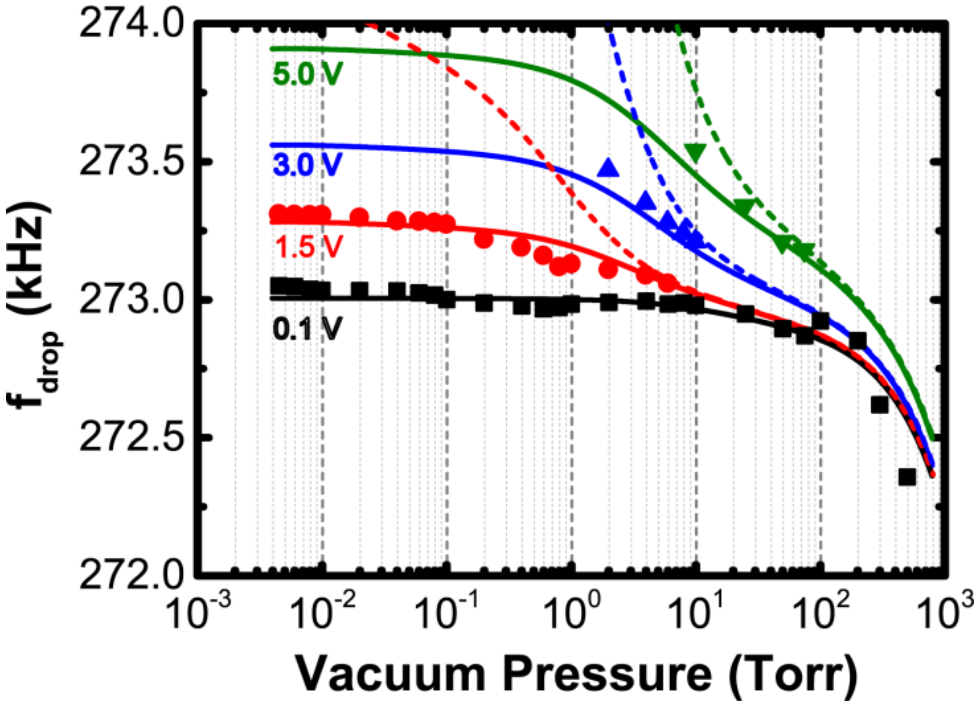

Figure 3.5. Drop frequency as a function of vacuum pressure. The drop frequencies (solid symbols) are measured at the points where the bi-stability occurs during the upward frequency sweep for the device operated at different vacuum pressure. The solid lines are fitting curves based on our nonlinear model (*i.e.*, Eq. (3-33) with $\xi_3=2.1 \times 10^{-7}$). The dashed lines are the corresponding model result when only the linear damping is included in the modeling.

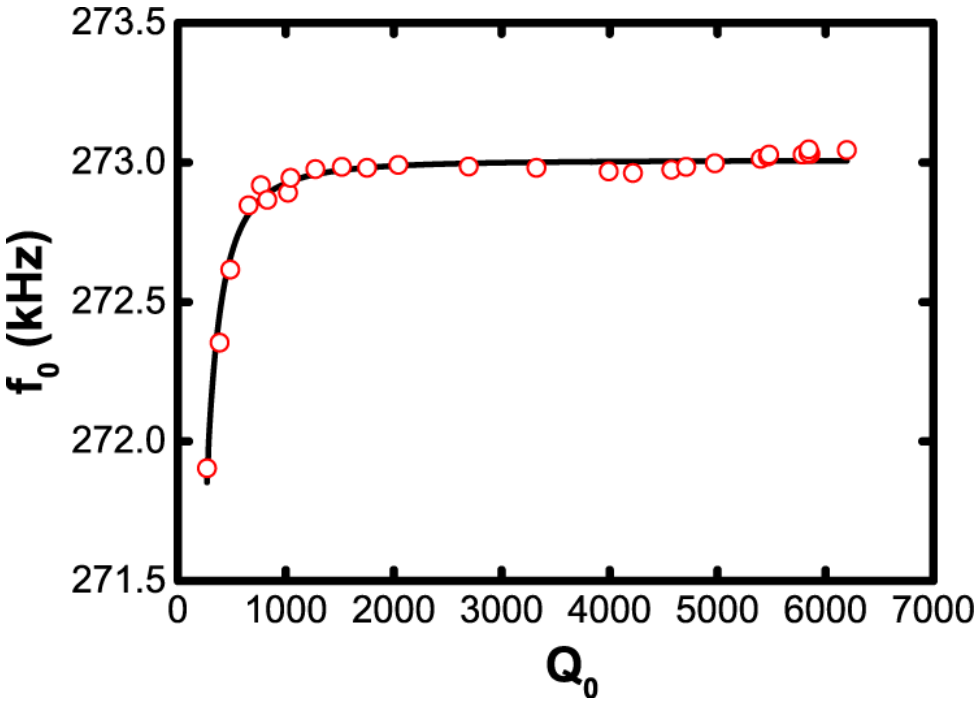

Figure 3.6. f_0 (red circles) measured at different vacuum pressures represented by the corresponding Q_0. The black solid line is the result of fitting according to Eq. (3-35).

REFERENCES

Anderson, D., Starosvetsky, Y., Vakakis, A. F., Bergman, L. A., Dynamic Instabilities in Coupled Oscillators Induced by Geometrically Nonlinear Damping, *Nonlinear Dyn.* 67, 807-827 (2012).

Bhiladvala, R. B., Wang, Z. J., Effect of Fluids on the Q Factor and Resonance Frequency of Oscillating Micrometer and Nanometer Scale Beams, *Phys. Rev. E*, 69, 036307 (2004).

Bunch, J. S., van der Zande, A. M., Verbridge, S. S., Frank, I. W., Tanenbaum, D. M., Parpia, J. M., Craighead, H. G., McEuen, P. L., Electromechanical Resonators from Graphene Sheets, *Science*, 315, 490-493 (2007).

Chen, C., Rosenblatt, S., Bolotin, K. I., Kalb, W., Kim, P., Kymissis, I., Stormer, H. L., Heinz, T. F., Hone, J., Performance of Monolayer Graphene Nanomechanical Resonators with Electrical Readout, *Nature Nanotech.*, 4, 861-867 (2009).

Cho, H., Jeong, B., Yu, M.-F., Vakakis, A. F., McFarland, D. M., Bergman, L. A., Nonlinear Hardening and Softening Resonances in Micromechanical Cantilever-Nanotube Systems Originated from Nanoscale Geometric Nonlinearities, *Int. J. Solids Struct.,* 49, 2059-2065 (2012).

Cho, H., Yu, M.-F., Vakakis, A. F., Bergman, L. A., McFarland, D. M., Tunable, Broadband Nonlinear Nanomechanical Resonator, *Nano Lett.*, 10, 1793-1798 (2010).

Chiu, H.-Y., Hung, P., Postma, H. W. Ch., Bockrath, M., Atomic-Scale Mass Sensing Using Carbon Nanotube Resonators, *Nano Lett.*, 8, 4342-4346 (2008).

Eichler, A., Moser, J., Chaste, J., Zdrojek, M., Wilson-Rae, I., Bachtold, A., Nonlinear Damping in Mechanical Resonators Made from Carbon Nanotubes and Graphene, *Nature Nanotech.,*, 6, 339-342 (2011).

Garcia-Sanchez, D., San Paulo, A., Esplandiu, M. J., Perez-Murano, F., Forro L., Aguasca, A., Bachtold, A., Mechanical Detection of Carbon Nanotube Resonator Vibrations, *Phys. Rev. Lett.*, 99, 085501 (2007).

Garcia-Sanchez, D., van der Zande, A. M., San Paulo, A., Lassagne, B., McEuen, P. L., Bachtold, A., Imaging Mechanical Vibrations in Suspended Graphene Sheets, *Nano Lett.*, 8, 1399-1403 (2008).

Gouttenoire, V., Barois, T., Perisanu, S., Leclercq, J.-L., Purcell, S. T., Vincent, P., Ayari, A., Digital and FM Demodulation of a Doubly Clamped Single-Walled Carbon-Nanotube Oscillator: Towards a Nanotube Cell Phone, *Small*, 6, 1060-1065 (2010).

Hüttel, A. K., Steele, G. A., Witkamp, B., Poot, M., Kouwenhoven, L. P., van der Zant, H. S. J., Carbon Nanotubes as Ultrahigh Quality Factor Mechanical Resonators, *Nano Lett.*, 9, 2547–2552 (2009).

Jensen, K., Kim, K., Zettl, A., An Atomic-Resolution Nanomechanical Mass Sensor, *Nature Nanotech.,* 3, 533-536 (2008).

Jensen, K., Weldon, J., Garcia, H., Zettl, A., Nanotube Radio, *Nano Lett.,* 7, 3508-3511 (2007).

Laird, E. A., Pei, F., Tang, W., Steele, G. A., Kouwenhoven, L. P., A High Quality Factor Carbon Nanotube Mechanical Resonator at 39 GHz, *Nano Lett.*, 12, 193-197 (2011).

Lassagne, B., Tarakanov, Y., Garcia-Sanchez, D., Bachtold, A., Coupling Mechanics to Charge Transport in Carbon Nanotubes Mechanical Resonators, *Science*, 325, 1107-1110 (2009).

Lifshitz, R., Cross, M. C., 2010. Nonlinear Dynamics of Nanomechanical Resonators. In *Nonlinear Dynamics of Nanosystems*; Radons, G., Rumpf, B., Schuster, H. G.; Wiley: New York.

Nayfeh, A. H., Mook, D. T, *Nonlinear Oscillations*, J. Wiley & Sons (1995).

Nigues, A., Siria, A., Vincent, P., Poncharal, P., Bocquet, L., Ultrahigh Interlayer Friction in Multiwalled Boron Nitride Nanotubes, *Nature Mat.*, 13, 688-693 (2014).

Poot, M., van der Zant, H. S. J., Mechanical Systems in the Quantum Regime, *Phys. Rep.*, 511, 273-335 (2012).

Sawaya, S., Arie, T., Akita, S., Diameter-Dependent Dissipation of Vibration Energy of Cantilevered Multiwall Carbon Nanotubes, *Nanotechnology*, 22, 165702 (2011).

Sazonova, V., Yaish, Y., Üstünel, H., Roundy, D., Arias, T. A., McEuen, P. L., A Tunable Carbon Nanotube Electromechanical Oscillator, *Nature*, 431, 284-287 (2004).

Shivaraman, S., Barton, R. A., Yu, X., Alden, J., Herman, L., Chandrashekhar, M., Park, J., McEuen, P. L., Parpia, J. M., Craighead, H. G. *et al.,* Free-Standing Epitaxial Graphene, *Nano Lett.*, 9, 3100-3105 (2009).

Singh, V., Sengupta, S., Solanki, H. S., Dhall, R., Allain, A., Dhara, S., Pant, P., Deshmukh, M. M., Probing Thermal Expansion of Graphene and Modal Dispersion at Low-Temperature Using Graphene Nanoelectromechanical Systems Resonators, *Nanotechnology*, 21, 165204 (2010).

Steele, G. A., Hüttel, A. K., Witkamp, B., Poot, M., Meerwaldt, B., Kouwenhoven, L. P., van der Zant, H. S. J., Strong Coupling between Single-Electron Tunneling and Nanomechanical Motion, *Science*, 325, 1103-1107 (2009).

Vakakis, A. F., Gendelman, O., Bergman, L. A., McFarland, D. M., Kerschen, G., Lee, Y. S., *Passive Nonlinear Targeted Energy Transfer in Mechanical and Structural Systems: I and II,* Springer Verlag (2008).

Verbridge, S. S., Ilic, R., Craighead, H. G., Parpia, J. M., Size and Frequency Dependent Gas Damping of Nanomechanical Resonators, *Appl. Phys. Lett.*, 93, 013101 (2008).

Wang, Z., Wei, J., Morse, P., Dash, J. G., Vilches, O. E., Cobden, D. H., Phase Transitions of Adsorbed Atoms on the Surface of a Carbon Nanotube, *Science*, 327, 552-554 (2010).

Wei, X., Wang, M.-S., Bando, Y., Golberg, D., Tensile Tests on Individual Multi-Walled Boron Nitride Nanotubes, *Adv. Mat.*, 22, 4895-4899 (2010).

Witkamp, B., Poot, M, van der Zant, H. S. J., Bending-Mode Vibration of a Suspended Nanotube Resonator, *Nano Lett.*, 6, 2904-2908 (2006).

Zaitsev, S., Shtempluck, O., Buks, E., Gottlieb, O., Nonlinear Damping in a Micromechanical Oscillator, *Nonlinear Dyn.*, 67, 859-883 (2012).

Chapter 4

System of Microcantilevers Coupled through a Nanomembrane[2]

4.1 Introduction

Microfabricated cantilever beams are ubiquitous in many MEMS/NEMS systems (Madou, 2011); *e.g.*, they are critical elements in atomic force microscopy (AFM), for sensing tip-sample interactions in the nano- to pico-Newton range needed for mapping topographical features of samples with sub-nanometer spatial resolution, or for directly measuring the local (nanoscale) mechanical properties of samples (Girssibl, 2003). Moreover, with surface functionalization, they are used as mass sensors of biomolecules or gas molecules in the zepto-, atto- or even yocto-gram range (Lavrik *et al.*, 2004; Li *et al.*, 2007; Goeders *et al.*, 2008; Naik *et al.*, 2009; Gruber *et al.*, 2011; Chaste *et al.*, 2012). These systems benefit from high resonant frequencies and Q-factors owing to their micro/nano scaling (*e.g.*, small dimensions and low energy dissipation properties), and their exceptional material properties (*e.g.,* newly discovered nanoscale components such as carbon-wall-nanotubes and graphene with high strengths and low material densities). Typical current devices based on microfabricated beams are mostly operated in their linear fundamental resonance modes with the above-mentioned benefits (Zhong *et al.*, 1993). However, as discussed previously in this Dissertation, their well-known narrow bandwidth (limited by

[2] B. Jeong, H. Cho, H. Keum, S. Kim, D.M. McFarland, L.A. Bergman, W.P. King, A.F. Vakakis, Complex Dynamics in the Limit of Weak Coupling of a System of Microcantilevers Connected by a Geometrically Nonlinear Tunable Nanomembrane, *Nanotechnology* (under review).

their linear resonances and high-Q operation) poses some limitations when broadband operating conditions are required.

The narrow bandwidth limitation of typical microfabricated beams can be eliminated through the introduction of intentional intrinsic nonlinearity (Vakakis *et al.*, 2008). This can be achieved by implementing strongly nonlinear flexible attachments of nanoscale size, such as nanotubes, nanowires or nanomembranes. The resulting microcantilever modified with the nanoresonator attachment is intrinsically broadband, and, hence, has the capacity to respond with high amplitude over broad frequency and energy ranges when subjected to complex external, self-excited or parametric excitations.

In recently considered designs such as the one discussed in the previous chapter, the required strongly nonlinear dynamic effects arise due to the high flexibility and small relative size of the nanoscale attachments, giving rise to geometric or kinematic nonlinearities. It is noted that while nonlinear dynamic behavior can be clearly detected and conveniently realized in these systems as a result of relatively high-amplitude oscillations of some of their components, most current studies remain in the framework of linear dynamics, with the nonlinear dynamic behavior either neglected or considered as detrimental to the design (Ekinci *et al.*, 2004; Ekinci and Roukes, 2005; Kacem and Hentz, 2009; Kacem *et al.*, 2010).

However, some recent studies have focused on exploiting nonlinearity toward addressing specific design goals, such as expanding the bandwidth (Cho *et al.*, 2010; Stanton *et al.*, 2010) or tuning the resonance frequencies (Rhoads *et al.*, 2005) of these devices. In Cho *et al.* (2012a), the concept of intentional nonlinearity for design was

implemented to predictively induce softening or hardening nonlinear effects in systems of microcantilever beams coupled by a tilted, flexible boron nitride nanotube. Whereas, as discussed in the previous chapter (see also Jeong *et al.* (2013)), a microcantilever with intentional geometric nonlinearity realized through an attached nanotube was designed and fabricated in order to accurately measure the linear and nonlinear damping properties of the attached nanotube under different ambient pressure conditions. These works demonstrated that intentional nonlinearity in the micro/nano scales is not only feasible and practical, but, in addition, it can pave the way for new types of strongly nonlinear designs with dynamics and performance that would not be attainable in conventional linear settings.

Among the various approaches for realizing (weak or strong) intentional nonlinearity in the dynamics of micro/nano mechanical resonators, the utilization of the geometry and kinematics of the response offers an advantage over other mechanisms. It provides intrinsic strong nonlinearity in the dynamics by producing tension (or/and compression) in one or more of its structural components during oscillation; moreover, the induced intrinsic geometric nonlinearity can be designed to be *non-linearizable*, - *i.e.*, the resulting force-response relationships will lack linear parts, which introduces important new features in the nonlinear design, such as the lack of preferential resonance frequencies and broadband passive adaptivity of the dynamics to various forcing environments (Vakakis *et al.*, 2008).

Unlike typical clamped-clamped microresonators where the geometrical nonlinearity is inherent, in designs based on microcantilever systems the utilization of intrinsic geometric nonlinearities requires special considerations. Indeed, as has been

shown in recent works, the introduction of intentional geometrical nonlinearity in microcantilever resonators by means of a very flexible nanoscale attachment can effectively convert the linear response of the microcantilever into strongly nonlinear (even non-linearizable) dynamics, exhibiting initiation of the nonlinear dynamic response even at relatively low amplitudes of oscillation (Cho *et al.*, 2010; Jeong *et al.*, 2013). In these works nanotubes were chosen for inducing the intrinsic geometric nonlinearity, which posed an inherent limitation in terms of the attainable yield rate due to an unreliable fabrication process through which the nanotube attachment is incorporated through manual integration by nano-manipulation. Considering that mass production is of great concern for the development of commercially realizable MEMS systems, it is clear that intentional incorporation of such strongly nonlinear designs calls for a reliable fabrication process.

In this work, we introduce a new way of implementing an intrinsically nonlinear microcantilever by utilizing a reliable batch-fabrication technique (Kim *et al.*, 2010) where a silicon membrane with nm-thickness is transferred and adhered onto a base silicon microcantilever structure. Although the flexibility (*e.g.*, measured by Young's modulus) of silicon is not as high as that of more widely used nanoscale components such as carbon nanotubes (CNTs) or boron nitride nanotubes (BNNTs), it has been validated by a number of researchers that silicon is an appropriate material for such nonlinear MEMS designs. Based on the developed device, the scope of the work presented in this chapter is, (i) to characterize the nonlinear dynamic response of a system of microcantilevers coupled by means of a nanomembrane with varying width; and (ii) to show that interesting and complex nonlinear dynamical phenomena are realized when the width of the membrane is

reduced, resulting in weak coupling between the two microcantilevers. Specifically, in the limit of weak coupling mode splitting is observed, leading to strong nonlinear localization phenomena in this system. Moreover, complexity in the oscillatory dynamics induced by the damping of the coupling nanomembrane drastically affects the steady state responses of the microcantilevers, introducing shifting of resonance peaks to different spatial locations on the microcantilevers. Hence, the overall aim of this work is to highlight the interesting and unexpected effects on the *global* dynamics of a weakly coupled multi-component microscale system, induced by intentional geometric nonlinearity implemented by a *local* nanoscale flexible component.

4.2 Theoretical Analysis

4.2.1. System Description

A schematic view of the system of two coupled microcantilevers considered in this work is depicted in Fig. 4.1a. By the construction of the experimental system, an identical harmonic base excitation is applied to both microcantilevers simultaneously. The uncoupled base system (*i.e.*, the system with no attached nanomembrane) is linear, with stiffness and damping nonlinearities generated by the coupling flexible nanomembrane due to geometric effects that arise from its high flexibility. The coupling nanomembrane is deposited through a fabrication process described in Section 4.3, and its geometry can be manipulated (altered) as described below.

The fundamental frequencies of the (linear) outer and inner cantilevers are estimated by finite element computations to be 46.87 kHz and 141.4 kHz, respectively. The nonlinear coupling between the inner and outer cantilevers is realized by incorporating a silicon membrane of thickness 300 nm across their gap, and patterning it through post-processing (denoted by the part in gray color in Fig. 4.1a). The corresponding strong geometric nonlinearity is generated due to the relative vertical displacement between the (more flexible) outer and inner cantilevers which leads to midplane stretching of the nanomembrane; similar nonlinear geometric effects were realized in previous studies through the use of ultraflexible nanowires and nanotubes (Cho *et al.*, 2012a, 2012b). In the system considered herein the strength of the coupling can be manipulated by controlling the width w of the coupling bridge (nanomembrane). In Fig. 4.1b a representative scanning electron microscope (SEM) image of the fabricated device with weak coupling strength ($w \sim 100$ nm) is shown. The accurate control of the width of the coupling bridge was a critical factor in this work, and dictated a new fabrication approach (elaborated in Section 4.3), which effectively realized the different specimens that were used in the tests performed.

4.2.2. EQUATIONS OF MOTION

Figure 4.2 depicts a representative lumped-parameter model of the system, assuming that each of the two microcantilevers oscillates in its fundamental mode. This assumption is expected to be valid as long as the frequency of the base excitation is away from higher

natural frequencies of the two microcantilevers, which is indeed the case in this study. Based on the simplified model, the equation of the motion of the system can be expressed as,

$$\begin{aligned} m_1\ddot{x}_1 + c_1\dot{x}_1 + k_1x_1 + T\cos\theta &= k_1x_0\cos\omega t - c_1x_0\sin\omega t \\ m_2\ddot{x}_2 + c_2\dot{x}_2 + k_2x_2 - T\cos\theta &= k_2x_0\cos\omega t - c_2x_0\sin\omega t \end{aligned} \tag{4-1}$$

where m_i, c_i and k_i are the effective mass, damping and stiffness coefficients of the *i-th* microcantilever when it oscillates in its fundamental mode, where $i = 1$ corresponds to the outer and $i = 2$ to the inner cantilever. The variables x_i denote the vertical displacements of the corresponding two microcantilevers, *T* denotes the (nonlinear) force generated in the coupling bridge due to axial stretching, and θ the angle formed between inner and outer microcantilevers due to discrepancy in their vertical displacements. The right-hand sides of Eqs. (4-1) represent forces generated by the harmonic base excitation of amplitude x_0.

The upper right schematic in Fig. 4.2 depicts the force interaction between the two masses under oscillation. Assuming that attached coupling bridge is composed of a viscoelastic material, we can write the stress-strain relation based on Kelvin-Voigt model as, $\sigma = E\varepsilon + \eta\dot{\varepsilon}$ where E is the elastic modulus of the material and η its viscosity. Next, the tension (*i.e.*, interaction force) T can be written as,

$$T = \sigma A = \frac{EA}{l_c}\delta + \frac{\eta A}{l_c}\dot{\delta} \tag{4-2}$$

where A denotes the cross-section area of the coupling bridge, and l_c the length of the coupling bridge. Geometric considerations based on Fig. 4.2 allow us to write the axial deformation δ as:

$$\delta = \sqrt{(x_1 - x_2)^2 - 2(x_1 - x_2) l_c \sin\varphi + l_c^2} - l_c \tag{4-3}$$

In Eq. (4-3), φ is the initial offset angle between the two microcantilevers at their equilibrium positions. The rate of the deformation with respect to time ($\dot{\delta}$) can be derived by differentiating Eq. (4-3) with respect to time t, as follows:

$$\dot{\delta} = \frac{(\dot{x}_1 - \dot{x}_2)(x_1 - x_2 - l_c \sin\varphi)}{\sqrt{(x_1 - x_2)^2 - 2(x_1 - x_2) l_c \sin\varphi + l_c^2}} \tag{4-4}$$

In addition, the term $\cos\theta$ can be also derived from geometric consideration and is expressed as:

$$\cos\theta = \frac{(x_1 - x_2 - l_c \sin\varphi)}{\sqrt{(x_1 - x_2)^2 - 2(x_1 - x_2) l_c \sin\varphi + l_c^2}} \tag{4-5}$$

Substituting (4-3), (4-4) and (4-5) into the vertical component of the interaction force $T\cos\theta$ leads to,

$$\begin{aligned} T\cos\theta = {} & k_c \left(1 - \frac{l_c}{\sqrt{(x_1 - x_2)^2 - 2(x_1 - x_2) l_c \sin\varphi + l_c^2}} \right) (x_1 - x_2 - l_c \sin\varphi) \\ & + c_c \frac{(\dot{x}_1 - \dot{x}_2)(x_1 - x_2 - l_c \sin\varphi)}{(x_1 - x_2)^2 - 2(x_1 - x_2) l_c \sin\varphi + l_c^2} \end{aligned} \tag{4-6}$$

where $k_c = EA/l_c$ and $c_c = \eta A/l_c$. Assuming that $x_1 - x_2 \ll 1$ and that $l_c = O(1)$, expanding expression (4-6) in Taylor series and retaining only third order terms, the term $T\cos\theta$ is approximated as:

$$
\begin{aligned}
T\cos\theta \approx\ & k_c \sin^2\varphi\left(x_1 - x_2\right) - \frac{3}{2}\frac{k_c}{l_c}\sin\varphi\left(x_1 - x_2\right)^2 + \frac{k_c}{2l_c^2}\left(x_1 - x_2\right)^3 \\
& + c_c \sin^2\varphi\left(\dot{x}_1 - \dot{x}_2\right) - 2\frac{c_c}{l_c}\sin\varphi\left(\dot{x}_1 - \dot{x}_2\right)\left(x_1 - x_2\right) + \frac{c_c}{l_c^2}\left(\dot{x}_1 - \dot{x}_2\right)\left(x_1 - x_2\right)^2
\end{aligned}
\tag{4-7}
$$

Further, we introduce the following parameters,

$$
\begin{aligned}
k_{1c} &= k_c \sin^2\varphi \qquad & c_{1c} &= c_c \sin^2\varphi \\
k_{2c} &= -\frac{3}{2}\frac{k_c}{l_c}\sin\varphi & c_{2c} &= -2\frac{c_c}{l_c}\sin\varphi \\
k_{3c} &= \frac{k_c}{2l_c^2} & c_{3c} &= \frac{c_c}{l_c^2}
\end{aligned}
\tag{4-8}
$$

and rewrite Eq. (4-7) as:

$$
\begin{aligned}
T\cos\theta \approx\ & k_{1c}\left(x_1 - x_2\right) + k_{2c}\left(x_1 - x_2\right)^2 + k_{3c}\left(x_1 - x_2\right)^3 \\
& + c_{1c}\left(\dot{x}_1 - \dot{x}_2\right) + c_{2c}\left(\dot{x}_1 - \dot{x}_2\right)\left(x_1 - x_2\right) + c_{3c}\left(\dot{x}_1 - \dot{x}_2\right)\left(x_1 - x_2\right)^2
\end{aligned}
\tag{4-9}
$$

Substituting the approximate expression (4-9) into the equations of motion (4-1), one derives the following set of equations of motion, which represents the reduced mathematical model of the system of nonlinearly coupled microcantilevers:

$$
\begin{aligned}
& m_1\ddot{x}_1 + c_1\dot{x}_1 + k_1 x_1 + k_{1c}\left(x_1 - x_2\right) + k_{2c}\left(x_1 - x_2\right)^2 + k_{3c}\left(x_1 - x_2\right)^3 \\
& + c_{1c}\left(\dot{x}_1 - \dot{x}_2\right) + c_{2c}\left(\dot{x}_1 - \dot{x}_2\right)\left(x_1 - x_2\right) + c_{3c}\left(\dot{x}_1 - \dot{x}_2\right)\left(x_1 - x_2\right)^2 \\
& = k_1 x_0 \cos\omega t - c_1 x_0 \sin\omega t \\
& m_2\ddot{x}_2 + c_2\dot{x}_2 + k_2 x_2 + k_{1c}\left(x_2 - x_1\right) - k_{2c}\left(x_2 - x_1\right)^2 + k_{3c}\left(x_2 - x_1\right)^3 \\
& + c_{1c}\left(\dot{x}_2 - \dot{x}_1\right) - c_{2c}\left(\dot{x}_2 - \dot{x}_1\right)\left(x_2 - x_1\right) + c_{3c}\left(\dot{x}_2 - \dot{x}_1\right)\left(x_2 - x_1\right)^2 \\
& = k_2 x_0 \cos\omega t - c_2 x_0 \sin\omega t
\end{aligned}
\tag{4-10}
$$

In the experimental tests that will be discussed in a forthcoming section, the dynamics of this system is examined at excitation frequencies lying in an intermediate range between the fundamental natural frequencies of the outer and inner microcantilevers.

It will be shown that provided that the nonlinear coupling force is weak, in that frequency range two localized frequency responses are detected, one localized to the outer microcantilever and the other to the inner one; in these localized responses one of the two microcantilevers oscillates with finite amplitude, whereas the other remains nearly stationary. It follows that in that intermediate frequency range one can approximately assume that either $x_1 \approx 0$ or $x_2 \approx 0$ (and $\dot{x}_1 \approx 0$ or $\dot{x}_2 \approx 0$ for each case) for these localized responses, and consider only one of equations (4-10). This would describe the nonlinear oscillation of the outer or inner microcantilever in the aforementioned localized state at the intermediate frequency range. In addition, considering that the experiment is performed under a condition of high vacuum, one may assume that $c_1,\ c_2 \ll 1$, so that the forcing terms $-c_1 x_0 \sin\omega t$ and $-c_2 x_0 \sin\omega t$ on the right-hand sides are small compared to the forcing terms $k_1 x_0 \cos\omega t$ and $k_2 x_0 \cos\omega t$, and, hence, can be neglected.

Accordingly, considering a steady state response localized to the outer microcantilever, one may approximately express the forced oscillation by the simplified governing equation,

$$m_1\ddot{x}_1 + (c_1 + c_{1c})\dot{x}_1 + (k_1 + k_{1c})x_1 + k_{2c}x_1^2 + c_{2c}\dot{x}_1 x_1 + k_{3c}x_1^3 + c_{3c}\dot{x}_1 x_1^2 = k_1 x_0 \cos\omega t \qquad (4\text{-}11)$$

with a similar expression holding for the localized forced response of the inner microcantilever.

4.2.3. MULTIPLE SCALES ANALYSIS

Note that Eq. (4-11) is similar to the equation of motion derived in previous studies (Cho *et al.*, 2012a; Jeong *et al.*, 2013), where a linear microcantilever attached to a grounded nanotube was studied. In this section, we perform the similar approach to derive the approximated steady state solution for Eq. (4-11). To facilitate the analysis, the normalization of Eq. (4-11) begins with introducing the following parameters:

$$\omega_1 = \sqrt{\frac{k_1 + k_c}{m_1}} \quad Q_1 = \frac{c_1 + c_c}{m_1 \omega_1} \quad \tau = \omega_1 t \quad \Omega = \frac{\omega}{\omega_1}$$
$$\omega_o = \sqrt{\frac{k_1}{m_1}} \qquad \Omega_o = \frac{\omega_o}{\omega_1} \tag{4-12}$$

Substituting (4-12) in (4-11), the equation of motion (4-11) is modified as,

$$x_1'' + \frac{1}{Q_1} x_1' + x_1 + \frac{1}{m_1 \omega_1^2}\left(k_{2c} x_1^2 + \omega_1 c_{2c} x_1' \; x_1 + k_{3c} x_1^3 + \omega_1 c_{3c} x_1' \; x_1^2\right) = \Omega_o x_0 \cos \Omega \tau \tag{4-13}$$

where prime denotes differentiation with respect to the new temporal variable τ. Eq. (4-13) is further normalized to a dimensionless form by introducing the characteristic length l_o and redefining the spatial amplitude $z_i \rightarrow x_i / l_o$. This leads to the following expression,

$$z_1'' + \frac{1}{Q_1} z_1' + z_1 + \alpha_{2c} z_1^2 + \eta_{2c} z_1' z_1 + \alpha_{3c} z_1^3 + \eta_{3c} z_1' z_1^2 = \Omega_o z_o \cos \Omega \tau \tag{4-14}$$

where a set of new parameters is expressed as:

$$\alpha_{nc} = \frac{k_{nc} l_o^{n-1}}{m_1 \omega_1^2} \quad \eta_{nc} = \frac{c_{nc} l_o^{n-1}}{m_1 \omega_1} \quad \text{for } n \in \{1, 2\} \tag{4-15}$$

To obtain the approximate solution of Eq. (4-14) in the vicinity of the linearized resonance (*i.e.*, $\Omega \approx 1$), the method of multiple scales (Nayfeh and Mook, 1995) is employed. The parameters in Eq. (4-14) are rescaled with respect to the small perturbation parameter ε as,

$$z_1 \mapsto \varepsilon z_1,\ \frac{1}{Q_1} \mapsto \frac{\varepsilon^2}{Q_1},\ \Omega_0 z_0 \mapsto \varepsilon^3 \Omega_0 z_0 \tag{4-16}$$

where ε denotes the smallness of the response. Substituting (4-16) in (4-14), we obtain

$$z_1'' + \frac{\varepsilon^2}{Q_1} z_1' + z_1 + \varepsilon \alpha_{2c} z_1^2 + \varepsilon \eta_{2c} z_1' z_1 + \varepsilon^2 \alpha_{3c} z_1^3 + \varepsilon^2 \eta_{3c} z_1' z_1^2 = \varepsilon^2 \Omega_o z_o \cos \Omega \tau \tag{4-17}$$

Moreover, the excitation frequency Ω is parameterized by the detuning parameter σ to restrict its range to the proximity to the linearized resonant frequency, *i.e.* $\Omega=1+\varepsilon^2\sigma$.

The multiple time scales are defined as $T_n=\varepsilon^n \tau$, $n=1,2,...$, and the time periodic solution of z_1 is expressed in the following form,

$$z_1(\tau;\varepsilon) = z_{1,0}(T_0,T_1,T_2) + \varepsilon z_{1,1}(T_0,T_1,T_2) + \varepsilon^2 z_{1,2}(T_0,T_1,T_2) + ... \tag{4-18}$$

where the derivative with respect to the dimensionless time t is expressed as:

$$d/d\tau = \partial/\partial T_0 + \varepsilon\, \partial/\partial T_1 + \varepsilon^2\, \partial/\partial T_2 + ... \equiv D_0 + \varepsilon D_1 + \varepsilon^2 D_2 + ... \tag{4-19}$$

Substituting Eqs. (4-18) and (4-19) into Eq. (4-17), a polynomial equation in terms of the small parameter ε is generated. By matching the coefficients of respective powers of ε, the following sub-problems are generated:

$$O(\varepsilon^0): D_0^2 z_{1,0} + z_{1,0} = 0 \tag{4-20a}$$

$$O(\varepsilon^1): D_0^2 z_{1,1} + z_{1,1} = -2D_0 D_1 z_{1,0} - \eta_{2c} D_0 {z_{1,0}}^2 - \alpha_{2c} {z_{1,0}}^2 \tag{4-20b}$$

$$O(\varepsilon^2): D_0^2 z_{1,2} + z_{1,2} = -2D_0 D_1 z_{1,1} - 2D_0 D_2 z_{1,0} - D_1^2 {z_{1,0}}^2 - D_0 {z_{1,0}}/{Q_1} - 2\alpha_{2c} z_{1,0} z_{1,1} - \alpha_{3c} {z_{1,0}}^3 - \eta_{2c} D_1 {z_{1,0}}^2 - 2\eta_{2c} D_0 z_{1,0} z_{1,1} - \eta_{3c} D_0 {z_{1,0}}^3 - \Omega_0 z_0 \cos(T_0 + \sigma T_2) \tag{4-20c}$$

• • •

The solution of Eq. (4-20a) is given by,

$$z_{1,0} = A_z(T_1, T_2) e^{jT_0} + c.c. \tag{4-21}$$

where $A_z(T_1,T_2)$ is a complex function representing the slowly varying modulus of the amplitude, and c.c. indicates its complex conjugate. Eq. (4-21) is substituted into Eq. (4-20b), followed by eliminating the secular term and letting $A_z=A_z(T_2)$, thus resulting in the solution of Eq. (4-20b) as follows:

$$z_{1,1} = -\alpha_{2c} A_z \bar{A}_z + \frac{1}{3} A_z^2 \left(\alpha_{2c} + 2j\eta_{2c}\right) e^{2jT_0} + c.c. \tag{4-22}$$

Eqs. (4-21) and (4-22) are then substituted to Eq. (4-20c), and the resulting secular term again is eliminated by setting the coefficient of e^{jT_0} zero. Accordingly, the complex modulation equation describing the slowly varying modulus is deduced as:

$$2jA_z' + j\frac{A_z}{Q_1} + j\left(\eta_{3c} - \frac{1}{3}\alpha_{2c}\eta_{2c}\right) A^2 \bar{A} + \left(3\alpha_{3c} - \frac{10}{3}\alpha_{2c}^2 - \frac{2}{3}\eta_{2c}^2\right) A^2 \bar{A} + \frac{1}{2}\Omega_0 z_0 e^{j\sigma T_2} = 0 \tag{4-23}$$

The complex modulus of the amplitude is then expressed in polar form $A_z(T_2) = {1}/{2}\,\alpha(T_2) e^{j\beta(T_2)}$, where α and β are the real valued functions with respect to the slowly varying time T_2, denoting the amplitude and the phase modulation, respectively.

Applying it to Eq. (4-23) and separating the resulting equation to the real and imaginary parts, one can obtain a set of real autonomous modulation equations as follows:

$$\begin{aligned}
\alpha' &= -\frac{\alpha}{2Q_1} - \frac{\alpha_{2c}\eta_{2c}}{24}\alpha^3 - \frac{\eta_{3c}}{8}\alpha^3 - \frac{\Omega_0 z_0}{2}\sin\gamma \\
\alpha\gamma' &= \alpha\sigma - \frac{3\alpha_{3c}}{8}\alpha^3 + \frac{5\alpha_{2c}}{12}\alpha^3 - \frac{\eta_{2c}}{12}\alpha^3 - \frac{\Omega_0 z_0}{2}\cos\gamma \\
\gamma &= \sigma T_2 - \beta
\end{aligned} \tag{4-24}$$

In Eq. (4-24), γ is the new parameter describing the phase shift in the steady state response to the excitation. Periodic steady state solutions and the frequency-amplitude relation of the steady state responses can be deduced from Eq. (4-24) by setting $\alpha' = \gamma' = 0$, and expressing the resulting equation in the form:

$$\left[\left(\frac{1}{2Q_1} + \frac{\alpha_{2c}\eta_{2c} + 3\eta_{3c}}{24}\alpha_{ss}^2\right)^2 + \left(\sigma - \frac{9\alpha_{3c} - 10\alpha_{2c} + 2\eta_{2c}}{24}\alpha_{ss}^2\right)^2\right]\alpha_{ss}^2 = \left(\frac{\Omega_0 z_0}{2}\right)^2 \tag{4-25}$$

Assuming now that the initial system is Hamiltonian (*i.e.*, unforced and undamped system), one can derive the following analytical asymptotic solution for the 'backbone' curve, *i.e.*, the relation describing the frequency-amplitude dependence of this dynamical system when it undergoes free undamped oscillations:

$$\alpha_{ss} = \left(\frac{24}{9a_{3c} - 10a_{2c}^2}\sigma\right)^{1/2} \tag{4-26}$$

Note that the overall nonlinear constant, which we define as $\mu = 9\alpha_{3c} - 10\alpha_{2c}^2$, is useful for determining the degree of the nonlinearity in the system, and, as explained in a forthcoming section, it can be derived by appropriately reconciling the experimental results with the reduced mathematical model (4-26).

4.3 Device Fabrication

The system of two coupled microcantilever beams was fabricated with conventional micromachining, transfer printing-based microassembly and ion-beam milling processing. The overall fabrication process is schematically depicted in Fig. 4.3. First, a set of two microcantilevers was fabricated on a Silicon-on-Insulator (SOI) wafer consisting of a stack of silicon layers (2 μm thick for the device layer and 400 μm thick for the substrate layer), with a silicon dioxide layer (2 μm thick) embedded between them, as shown in Fig. 4.3a. The formation of the cantilever structure on the device layer was implemented with a photolithography process, as shown in Figs. 4.3b,c, which was then followed by a deep reactive ion etching (DRIE) process to etch the silicon and remove the photoresist mask (this is shown in Fig. 4.3d). The same process was repeated for the backside of the SOI wafer to provide the necessary space for the cantilevers to oscillate freely (see Figs. 4.3e,g). Upon the completion of the patterning the fabricated structure, the processed wafer was immersed into a hydrofluoric acid (HF) solution to etch the remaining buried oxide layer (as shown in Fig. 4.3h), consequently forming a set of two free-standing microcantilevers.

After the set of microcantilevers was fabricated, the coupling bridge between them was implemented by means of a nanomembrane. Specifically, the coupling bridge between the fabricated two microcantilevers was produced by transfer-printing a thin silicon membrane with a thickness of 300 nm. The silicon ink, referring to the square-shaped thin silicon membrane, was prepared with a conventional mircofabrication process on a

different SOI wafer, which was then picked up and transferred by a elastomeric stamp onto the pre-fabricated microcantilevers (as shown in Fig. 4.3i). The bonding between the microcantilevers and the transferred silicon ink was implemented by a subsequent annealing process which induced silicon fusion bonding (Keum *et al.*, 2012) between them. In the next step, ion-milling processing by a Focused-Ion-Beam (FIB) machine was performed to remove the unnecessary part of the silicon layer and to pattern a narrow bridge connecting each end of the two microcantilevers, thus forming the system of two coupled microcantilevers (see Fig. 4.3j).

Although we have utilized a serial process where the integration of the silicon membrane was performed on a single set of microcantilevers by a single stamp and the coupling bridge was patterned through ion-milling, the aforementioned fabrication process can be realized as a batch process. The formation of the bridge component can be achieved during the preparation of the silicon ink as an embedded pattern, and the transfer of the patterned silicon membranes can be performed by an array of stamps for a parallel printing process potentially on a wafer scale or for a continuous roll-to-roll printing process (Yang *et al.*, 2012). Hence, fabrication of this system can be conveniently performed on a mass scale, in contrast to systems considered in previous works (Cho *et al.*, 2012a; Jeong *et al.*, 2013) where nanotubes were utilized as elements coupling disjoint microsystems.

4.4. Experimental Results

4.4.1. Experimental Setup

A schematic diagram describing the experimental setup is depicted in Fig. 4.4. The fabricated microcantilever system consisting of the two microcantilevers with the coupling nanomembrane was mounted and clamped on a stack of the piezoelectric actuator, with the actuation in the form of a base excitation driven by an AC signal of a constant amplitude V_{pp}. Measurement of the response of the system was performed after it reached steady state oscillation so that the initial transient response would not interfere with the measured dynamics.

The steady state dynamic response was measured by light interferometry using the laser microvibrometer that used also in the previous application (Chapter 3), whose acquired signal was fed to an oscilloscope along with the signal from the function generator, which was used as a reference. The set of measured electrical signals, in the form of time series responses, was then stored in the main control computer, where digital Fourier transforms were performed in order to study the harmonic contents of the inputs and outputs, as well as the corresponding phases at steady state with respect to the driving frequency.

In order to investigate the steady state dynamic response of the system over the entire frequency range of interest, the driving frequency was swept forward (up) and then backward (down) during testing. Moreover, in order to minimize dissipation effects in the tested microsystem due to ambient pressure, the test samples were placed inside a vacuum chamber where the pressure (P) was reduced to the constant level of 8.0 mTorr, so that

conditions of high vacuum were realized. It was assumed that at this low level of ambient pressure the corresponding ambient dissipation effects on the samples were much smaller (and, hence, negligible), compared to the inherent internal dissipation resulting from inherent structural damping of the microcantilevers and, more important, the coupling nanomembrane. Finally, the specific locations of the measurement (sensing) points where the steady state oscillation of the test sample was recorded were controlled by a mechanical stage installed beneath the vacuum chamber.

4.4.2. TRANSITION FROM LINEAR TO NONLINEAR DYNAMICS

Before attaching the nonlinear bridge component (the nanomembrane), the dynamic response of each of the two uncoupled microcantilevers was characterized in the region of its own fundamental resonance in order to confirm the linear dynamics of the microcantilevers in the amplitude and frequency ranges of interest. Indeed, the experimental steady state frequency responses shown in Fig. 4.5, measured at different levels of input base excitation, indicate that the dynamics of the system of uncoupled microcantilevers is linear; this is mainly deduced by the fact that no nonlinear hysteresis loops are observed in the resonance region for increasing input voltage V_{pp} (*i.e.*, amplitude of input base excitation).

These measurements prove conclusively that *the exclusive source of the nonlinear effects in the coupled system that will be considered below is the nanoscale bridge (nanomembrane) that is integrated between the two microcantilevers*. Moreover, from

these measurements the fundamental modal frequencies of the inner and outer microcantilevers were measured at 139.52 kHz (Fig. 4.5a) and 50.09 kHz (Fig. 4.5b), respectively, which are close to the estimated values from FEM simulations reported in Section 4.2.1. The inset in each plot shows that, in the absence of the bridge component, in the resonance region of each of the two microcantilevers the other microcantilever is in a state of off-resonance and thus remains nearly stationary. This is caused by the wide frequency separation of the fundamental modes of the inner and outer microcantilevers, and confirms that in the absence of the nanoscale bridge there is negligible coupling between the two microcantilevers through the common base to which they are connected.

Considering now the coupled system after the addition of the nanobridge, one anticipates that due to its flexibility the connecting nanomembrane will induce geometric stiffness nonlinearity in the system. In order to characterize the effect of the nonlinear coupling stiffness on the dynamic response, the width of the nanomembrane was systematically reduced in a controlled fashion from 20 μm to 0.10 μm by gradually cutting transversely the coupling bridge through FIB ion milling. Taking into account that the rectangular cross-sectional area of the coupling bridge is proportional to its (nominally linear) axial stiffness, one anticipates that this stiffness would change linearly with the width of the coupling bridge as long as its length and thickness remain unchanged. In all tested samples the length of the coupling bridge was maintained at 5 μm.

In the plots of Fig. 4.6 the frequency responses measured at the tip of the outer microcantilever of the coupled system are depicted for decreasing width of the coupling bridge, *i.e.*, for decreasing coupling strength. In the experimental tests shown only forward

frequency sweeps are presented, at intermediate frequency ranges between the two fundamental natural frequencies of the outer and inner microcantilevers, since it was found that in that frequency range complex nonlinear dynamical phenomena take place.

Focusing on the responses of the outer microcantilever of Fig. 4.6, the SEM images included in the insets of the plots depict the nanoscale bridge implemented for each sample. For the cases of relatively strong coupling depicted in Figs. 4.6a-c the frequency responses appear to be linear (similar to the plots depicted in Fig. 4.5), and do not exhibit any nonlinear dynamical features, such as hardening/softening resonance curves, jump phenomena or hysteresis loops (Cho *et al.*, 2010, 2012a,b).

However, as coupling decreases (*cf.* Fig. 4.6d-e), the nonlinearity induced in the system by the nanomembrane (which now possesses enhanced flexibility generating strong geometric stiffness nonlinearities) affects the dynamic frequency responses, with clear transitions between the stable steady state branches in the bi-stable regions as the driving frequency is swept forward. The red markers in each of the plots of Fig. 4.6 denote the maximum oscillation amplitudes at the set of considered excitation amplitudes (V_{pp}) when the driving frequency is swept forward. These points are selected to numerically fit backbone curves in the experimental plots using equation Eq. (4-26) of the mathematical model derived in Section 4.2.3; the resulting fitted curves are shown in red curves of Fig. 4.6. The backbone curves provide the frequency-amplitude relations of the corresponding unforced and undamped (Hamiltonian) systems at each of the considered widths of the coupling nanomembrane, and can be approximated by the loci of the maxima of the frequency responses as the input amplitude increases.

It is noteworthy that these numerical fits show that there exist two different regions of nonlinear behavior, namely a *softening* behavior where the fitted backbone curves veer to the left (i.e., towards lower frequencies), and a *hardening* behavior where the backbone curves veer to the right (towards higher frequencies). Hence, there appears to be *co-existence of softening and hardening nonlinear behavior* in these frequency responses. The observed transition from initially softening to hardening nonlinear behavior occurs above a threshold amplitude, and signifies the presence of two different nonlinear dynamical mechanisms in the weakly coupled system as the energy of oscillation varies. We conjecture that this might be due to a vertical offset between the two microcantilevers, which may vary at different oscillation levels and, as shown in Cho *et al.* (2012a) can lead to softening or hardening nonlinear behavior. An additional possibility might be the interchange between a state of local buckling (leading to nonlinear softening behavior) and nonlinear axial stretching (leading to nonlinear hardening behavior) of the flexible nanomembrane as the amplitude of oscillation varies from low to high values.

The bifurcation (jump) between two stable branches, marked by the sharp transition at the drop frequency, becomes clearer in Figs. 4.6f-h, as the width of the nanomembrane decreases further, leading to further decrease of the coupling strength between the two microcantilevers. The most drastic transition between the stable points in the frequency response was observed for the system with a bridge width of 350 nm, depicted in Fig. 4.6g. Unlike in the other cases tested, a different series of jump phenomena appear as V_{pp} increases, and the high-amplitude branch of the stable frequency responses follows a trend of hardening behavior. It evidently shows (perhaps more clearly than the other cases) that

there exist two distinct dynamical mechanisms of hardening and softening nonlinearity in the system, potentially forming S-shaped backbone curves (see, for example, the plot of Fig. 4.6g).

The parameter μ for the degree of the nonlinearity of Eq. (4-26) is derived directly from the fitted backbone curves and summarized with respect to the axial stiffness of the coupling bridge in Fig. 4.7. In both of the hardening (Fig. 4.7a) and softening regimes (Fig. 4.7b), one can observe that the nonlinear effects are nearly negligible when the axial stiffness of the coupling bridge is greater than 50 kN/m, whereas they increase significantly for smaller values of the axial stiffness when the coupling between the two microcantilevers becomes increasingly weaker. This can be explained by noting that for larger widths (leading to stronger coupling axial stiffness) the nanomembrane is less flexible so that geometric nonlinear effects such as buckling (leading to softening behavior) or finite curvature and midplane stretching effects (leading to hardening behavior) are negligible, so the dynamics of the system is almost linear. However, for smaller widths of the nanomembrane the previous geometric nonlinear effects are enhanced due to its increased flexibility, giving rise to the observed strongly nonlinear dynamical responses of the frequency responses of Fig. 4.6. As mentioned previously, a possible cause of the two co-existing nonlinear mechanisms is the vertical offset between the two microcantilevers, which, as shown in Cho *et al.* (2012a), can lead to either softening or hardening nonlinear behavior, depending on the angle of orientation of the connecting nanomembrane.

4.4.3. RESONANT PEAK SEPARATION

The experimental results of Figs. 4.6 and 4.7 conclusively show that the addition of the highly flexible nanomembrane can lead to strongly nonlinear dynamic behavior of the system of microcantilevers at an intermediate frequency range between their fundamental natural frequencies. Moreover, judging from the insets of Fig. 4.6 where the dynamic response of the inner cantilever at the same intermediate frequency range corresponding to each considered width of the nanomembrane, one deduces that the nonlinear dynamical response is localized to the outer microcantilever since the corresponding frequency responses of the inner microcantilever are negligible. These results demonstrate in part the highly complex nonlinear dynamics of the weakly coupled system.

However, even more interesting nonlinear dynamical phenomena are revealed when one considers the frequency responses of the inner microcantilever at the same intermediate frequency regime, revealing the existence of an additional family of responses localized to the inner microcantilever when the width of the nanomembrane is reduced below a critical threshold. This interesting nonlinear dynamics is discussed below.

In Fig. 4.8 an additional series of frequency response plots is presented, showing forward frequency sweeps of dynamical responses measured at the tip of the inner microcantilever at the same intermediate frequency range, for varying forcing amplitudes and for decreasing width of the coupling nanomembrane (only small widths $0.1\ \mu m \leq w \leq 5\ \mu m$ are considered in Fig. 4.8). As shown in the insets where the frequency spectra of the responses at the tip of the outer microcantilever at the same frequency ranges are shown, the nonlinear responses of Fig. 4.8 are strongly localized to the inner cantilever, in

contrast to the responses of Fig. 4.6, which are localized to the outer microcantilever. Hence, a pair of localized nonlinear modes is realized in the intermediate frequency range between the natural frequencies of the two microcantilevers, when the width of the nanomembrane (or, equivalently, the axial coupling stiffness) decreases below a critical value and conditions of weak coupling are realized.

Considering in more detail the frequency responses of Fig. 4.8, we note that in similarity to the localized response of the outer microcantilever of Fig. 4.6 the localized response of the inner microcantilever exhibits both hardening and softening nonlinearity, the latter appearing only for exceedingly small widths of the nanomembrane (cf. Fig. 4.8d and e). Moreover, complex nonlinear response is observed in Fig. 4.8d, where two disjoint (high- and low-amplitude) stable branches are realized, similar to the set of disjoint branches of Fig. 4.6g for the outer microcantilever. Again, we emphasize that this complex nonlinear dynamics is caused entirely by the geometric nonlinearity induced by the nanomembrane to the system of coupled microcantilevers, since, as shown in Fig. 4.5, in the absence of the coupling bridge the uncoupled microcantilevers exhibit linear dynamics.

4.4.4. Nonlinear Complex Mode and Frequency-splitting for Weak Coupling

The mode splitting generating the aforementioned nonlinear localized modes is more clearly deduced in the experimental frequency responses of Fig. 4.9. These plots depict the dynamic responses of the tips of the inner (red markers) and outer microcantilever (blue markers) for different widths of the coupling bridge, for forward driving frequency sweeps,

and at fixed vacuum pressure of 8.0 mTorr. At the strong coupling case (see Fig. 4.9a and Fig. 4.9c for $w = 20\mu m$), the dynamic responses of the inner and the outer cantilevers are synchronized since their resonant peaks coincide and the corresponding phase transitions appear at nearly identical frequencies. However, as the frequency responses of Fig. 4.9c show, when the coupling width decreases this synchronized mode can no longer exist. Indeed a mode splitting occurs, evidenced by resonance peak separation, which gives rise to nonlinear localization as described previously. To better represent this mode splitting in Fig. 4.9c, for each width the frequency is normalized with respect to the frequency of maximum response of the outer cantilever, whereas the amplitudes are normalized by the maximum amplitudes.

With decreasing width (or coupling) the frequency split between the two localized responses increases until it reaches a maximum frequency separation for $w = 0.35\,\mu m$. However, for the smaller width of $w = 0.1\,\mu m$ the frequency split decreases, indicating that at a certain coupling strength, the frequency deviation and resulting nonlinear localization in the coupled system reaches a maximum.

In Fig. 4.10a the resonance frequencies of the two localized modes that are generated by the mode splitting in the weakly coupled system are depicted, whereas in Fig. 4.10b the corresponding ratio of the amplitude of the outer cantilever to that of the inner at each resonance frequency is shown as a function of the width of the nanomembrane. As the coupling strength between the microcantilevers decreases, the resonance frequencies of the two localized modes also decrease, but the splitting between these frequencies increases until it reaches a maximum at a width of $w = 0.35\,\mu m$. The resulting

localization of the responses to the outer and inner microcantilevers is highlighted in Fig. 4.10b. It is noted that localization becomes stronger with decreasing nanomembrane width (weaker coupling), in contrast to the case of relatively large widths (stronger coupling), where the amplitudes of the two microcantilevers are comparable.

Even more interesting features of the nonlinear dynamics of the weakly coupled system are deduced when one considers the (forward sweep) frequency responses and the corresponding deflection shapes of the microcantilevers at different sensing positions on the two microcantilevers. In Figs. 4.11a,b the asynchrony of the two localized modes of the system with weak coupling (w =0.35 μm) is investigated by depicting the frequency responses and phases for fixed input voltage $V_{pp} = 80\,mV$ and small width of the coupling bridge, w =0.35 μm. It is noted that each point on the microcantilever system exhibits a different frequency peak and drop frequency, indicating a shift of the resonance frequencies of the two modes at different locations on the system. As studied in Blanchard *et al.* (2014), this effect is due to mode complexity in the steady state dynamics, and results from non-proportional damping distribution in the system. In particular, the local damping introduced by the oscillation of the nanomembrane perturbs the uniform distribution of damping in the elastic system of the two microcantilevers and gives rise to mode complexity, *i.e.*, asynchronous oscillation patterns where different points of the system oscillate with non-trivial phase differences. This mode complexity produces a shift of the resonance peaks of the two localized modes, as evidenced by the results of Figs. 4.11a,b. Hence, the appearance of these shifts in the resonance peaks measured at different sensing

locations on the two microcantilevers is attributed to the (strong) localized damping induced in the system by the oscillating nanomembrane.

Based on these observations we conjecture that a possible cause for the mode splitting at the intermediate frequency range depicted in Fig. 4.10 might be the aforementioned mode complexity that leads to a shift of the resonance peaks measured at different spatial locations in the weakly coupled system of microcantilevers. Indeed, for small widths of the coupling nanomembrane its axial stiffness decreases, but, at the same time, it provides a local source of damping that perturbs the overall proportional damping distribution in the system, causing mode complexity in the frequency responses and shifting the resonance peaks at different measurement locations in the inner and outer microcantilevers. This mode complexity and the ensuing localization of the steady state responses may lead to the aforementioned mode splitting in the weakly coupled system.

The localized patterns of the corresponding deflection shapes of the system at each of the seven resonance peaks (corresponding to each of the sensing locations) are evident in the reconstructions of Fig. 4.11c. To perform these reconstructions, the steady state amplitude and phase measured at the set of selected points on the microcantilever system were used to estimate the spatial distributions of vertical deflections of the inner and outer microcantilevers. Note the relatively large deflections of the outer microcantilever at the sensing locations 1-4 and of the inner microcantilever at the points 5-7, highlighting the strong localization features of the two bifurcating modes at that weak value of the coupling.

4.5. Conclusions

This was the second study of implementation of intentional strong nonlinearity in a microstructure with coupling between components provided by a nanoscale flexible component. Compared to the first application, the system studied in this Chapter was more complex, as it involved a nonlinearly coupled system of microcantilevers. The overall aim of the study was to study the combined effects of weak coupling and strong nonlinearity in the dynamics of this system, and show that complex and unexpected dynamics are realized in the limit of weak coupling (see Table 4.1 for the tabularized summary of the experiment). These include co-existence of softening and hardening nonlinear dynamic behaviour, mode splitting leading to nonlinear motion localization, and resonance peak shifting due to non-proportional damping distribution. It is interesting that all these effects are induced solely by the oscillation of the nanomembrane, which provides a local source of strong nonlinearity and damping in the overall micro-scale system.

Moreover, compared to the system considered in Chapter 3, the coupled system of microcantilevers considered in this application is more practical since it can be conveniently reproduced on a mass-scale. Indeed, transfer printing-based microassembly was effectively utilized for implementing strong intentional geometrical nonlinearity in this microscale system. To this end, the nanomembrane was fabricated and attached in the gap between the two linear microcantilevers, introducing, in effect, a tunable nanoscale bridge between them. By systematically reducing the width of the nanomembrane in a controlled fashion, one is able to predictably reduce the axial coupling stiffness between the two

microcantilevers and study the effect of varying coupling on of the dynamics of the system. Moreover, geometric nonlinearities induced by the transverse oscillation of the flexible nanomembrane represent a local source of intentional strong nonlinearity in the system. Compared to analogous nanotube integrations considered in the previous Chapter and previous works, the fabrication method used in the present work provides a convenient, yet reliable, means of implementing the nanoscale bridge in a controlled manner. This is markedly different compared to manual integration of nanotubes used in previous studies, that resulted in unavoidable uncertainties in the fabrication process, and posed difficulties in the manipulation (and tunability) of the coupling bridge after its initial synthesis. Hence, the proposed fabrication scheme of a microscale system with a nonlinear nanocomponent incorporating intentional strong nonlinearity holds promise for a new way to conveniently and reliably manufacture such systems.

The nanoscale flexible bridge introduces interesting and complex nonlinear dynamical phenomena in the microcantilever system. Indeed, both hardening and softening nonlinear dynamic responses are realized, depending on the energy of the oscillation and the strength of the coupling. This indicates co-existence of different nonlinear dynamical mechanisms caused by the oscillations of the flexible nanomembrane; namely, hardening stiffness nonlinearity due to axial stretching and softening stiffness nonlinearity caused by local buckling. These co-existing strongly nonlinear dynamical mechanisms are generated exclusively by the flexibility of the nanomembrane and by the possible initial vertical offset of the two microcantilevers.

In addition, an unexpected mode splitting leading to nonlinear localization was experimentally observed when the coupling stiffness was reduced below a critical threshold, at an intermediate frequency range between the frequencies of the fundamental bending modes of the two uncoupled microcantilevers. In particular, for sufficiently weak coupling (or width of the nanomembrane) an in-phase vibration mode appeared to split into two modes, each predominantly localized to one of the microcantilevers. The localized modes exhibited strongly nonlinear dynamic behavior, possessing both softening and hardening features depending on the energy level of the oscillation. Moreover, for each localized mode a shifting of the resonance peaks along different locations of the system was detected, attributed to mode complexity in the dynamics caused by the strong local damping induced by the oscillating nanomembrane, and rendering the damping distribution in the system non-uniform (non-proportional).

The experimental results reported in this work demonstrate that weakly coupled flexible microresonators with nanoscale connecting bridges may possess highly complex nonlinear dynamics which need to be taken into account in the design of such systems. Indeed, otherwise linear microresonators can possess highly complex nonlinear dynamical behavior caused by geometric nonlinearities when they are coupled by flexible nanoscale bridges.

FIGURES

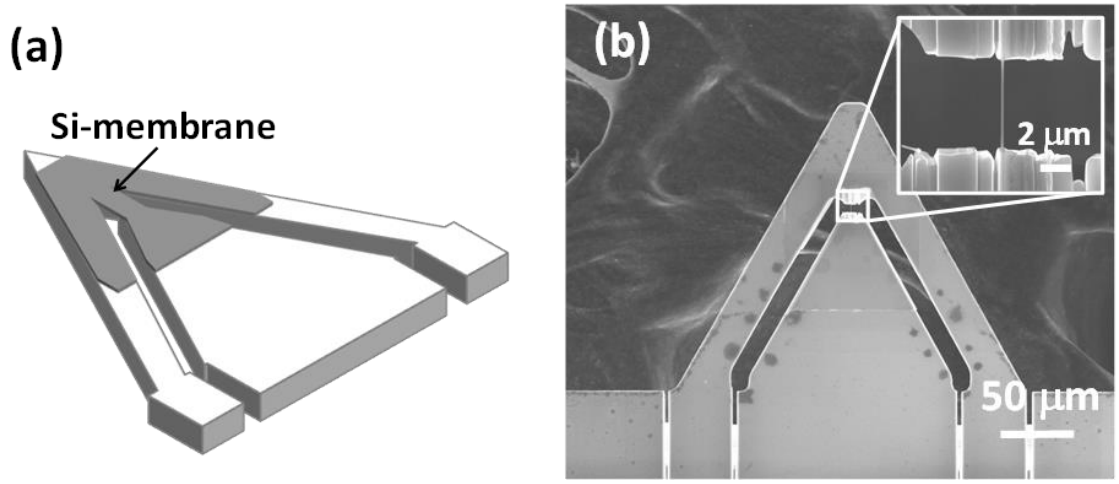

Figure 4.1. System under consideration: (a) Schematic view of the device, with the basic structure (indicated by the light color) composed of two microcantilevers with coupling between them provided by a silicon membrane (indicated by the shaded region) with the patterned nanoscale bridge; (b) Scanning Electron Microscope (SEM) image of the device after fabrication, with the width, thickness and length of the reduced coupling bridge (nanomembrane) being 0.35 μm, 0.3 μm and 5 μm, respectively.

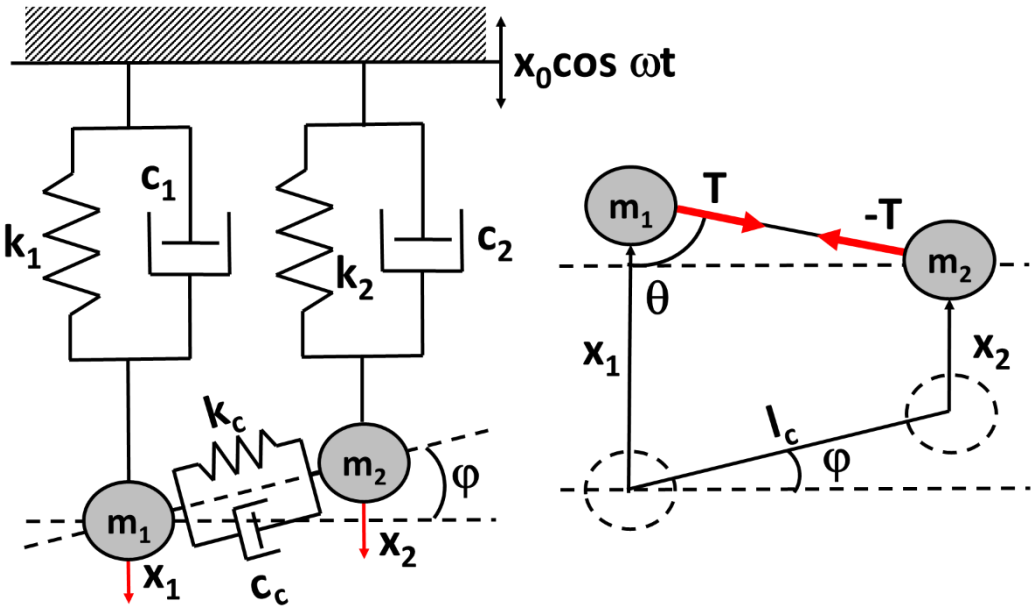

Figure 4.2. Lumped-parameter two-degree-of-freedom model of the system of Fig. 4.1, with both cantilevers assumed to oscillate close to the linearized natural frequency of the inner cantilever; the upper right figure is a schematic view of the force interaction between the two discrete oscillators.

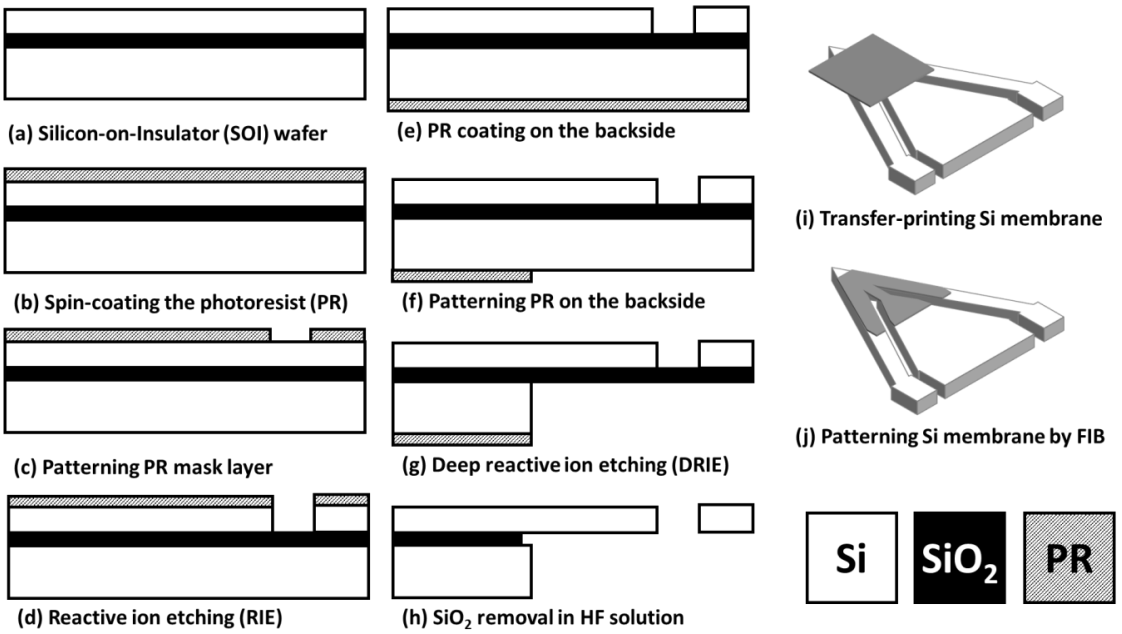

Figure 4.3. Fabrication flow chart: The implementation involves conventional microfabrication techniques (a-h), followed by transfer-printing (i); the coupling bridge (nanomembrane) is constructed on the transferred Si-membrane by an ion-milling process (j).

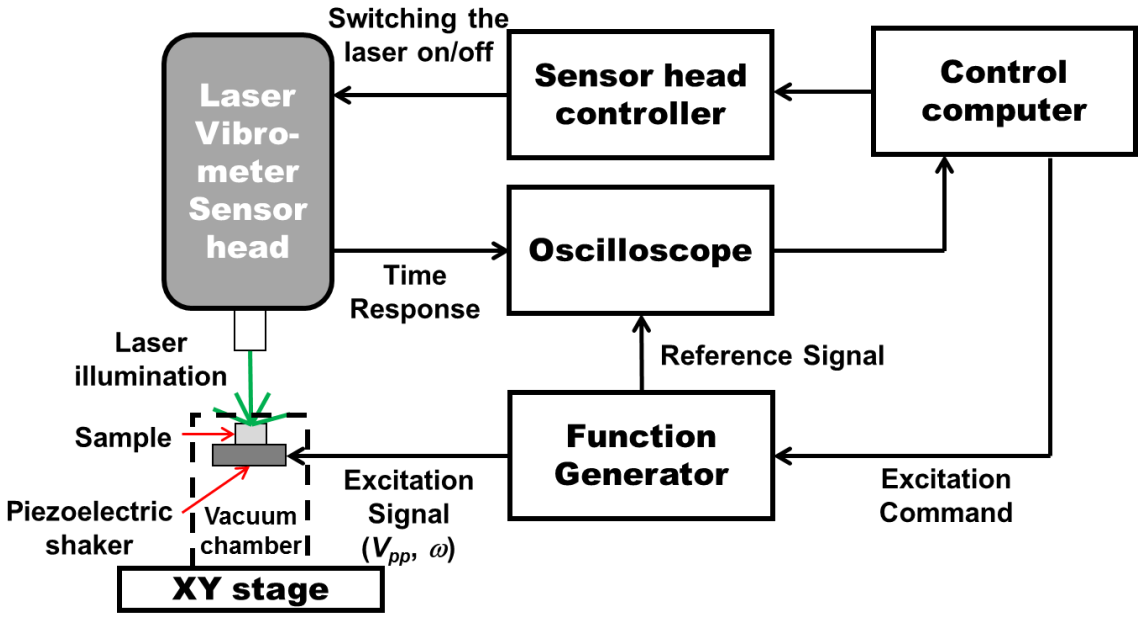

Figure 4.4. Block diagram of the experimental setup showing the data acquisition system based on microlaser vibrometry.

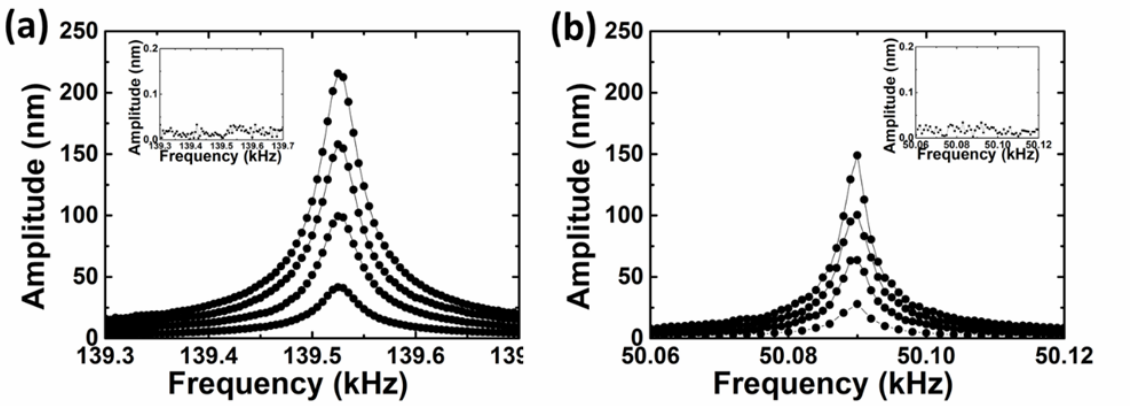

Figure 4.5. Experimental linear dynamical response of the uncoupled system of microcantilevers in the absence of the coupling bridge (nanomembrane): Linear frequency response of the (a) inner cantilever, and (b) outer cantilever. In each case the inset depicts the frequency response of the other microcantilever in the same frequency range in order to highlight its off-resonance state. The measurements depicted in these plots were performed at fixed levels of input voltage, $V_{pp} =$ 30, 70, 110 and 150 mV for the main plots, and V_{pp}=80 mV for the insets.

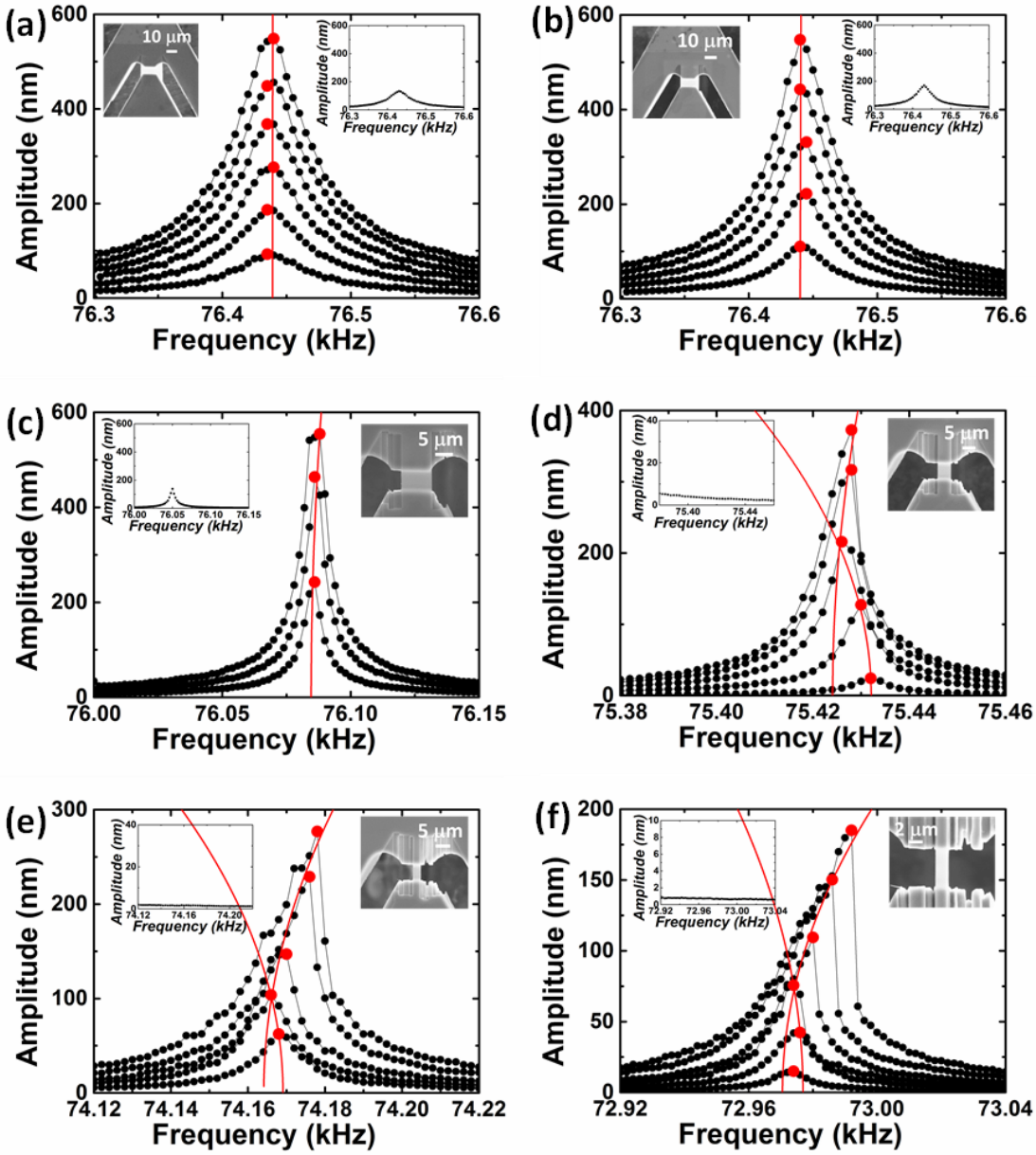

Figure 4.6. (cont.)

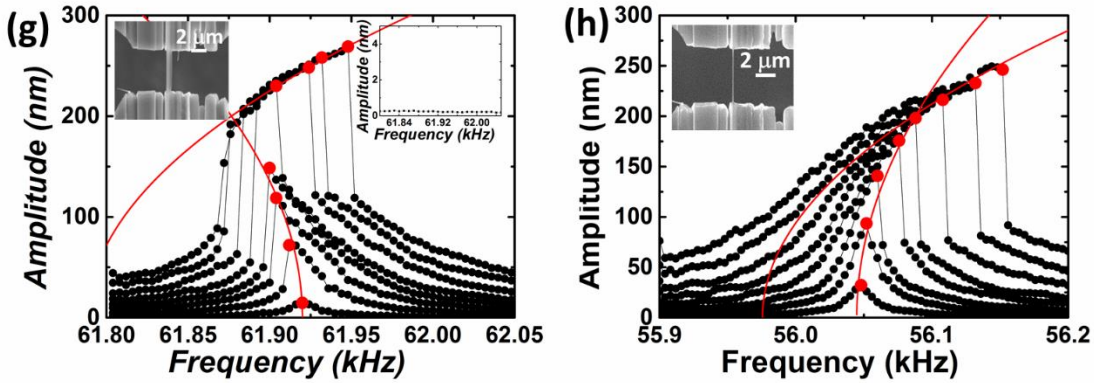

Figure 4.6. Nonlinear dynamic responses at the tip of the outer microcantilever for decreasing width w of the coupling bridge (nanomembrane) when the frequency is swept forward in a range close to the frequency of the in-phase mode: (a) $w = 20$ μm, (b) $w = 12$ μm, (c) $w = 8$ μm, (d) $w = 5$ μm, (e) $w = 3$ μm, (f) $w = 2$ μm, (g) $w = 0.35$ μm and (h) $w = 0.1$ μm. In a set of insets the frequency spectra of the responses of the inner microcantilever at the same frequency range are shown, whereas in another set of insets the corresponding SEM images of the coupling bridges are presented. In each case the driving voltage (V_{pp}) is gradually increased from a small to the large value in order to observe the transition of the nonlinear dynamic response under different forcing amplitudes, whereas the vacuum pressure (P) was kept constant at 8.0 mTorr. The nonlinear constant μ, derived from the corresponding backbone curves (red lines) fitted to the drop amplitudes (red circles), was estimated as, (a) $\mu = 0$, (b) $\mu = 0$, (c) $\mu = 3.45 \times 10^{-9}$, (d) $\mu = -4.80 \times 10^{-8}$, 1.04×10^{-8}, (e) $\mu = -9.46 \times 10^{-8}$, 6.47×10^{-8}, (f) $\mu = -1.67 \times 10^{-7}$, 2.28×10^{-7}, (g) $\mu = -4.21 \times 10^{-7}$, 8.52×10^{-7} and (h) $\mu = 4.61 \times 10^{-7}$, 1.18×10^{-6} (in order to fit the backbone curves to the experimental data the reduced model (4-26) is used with l_0=1 nm).

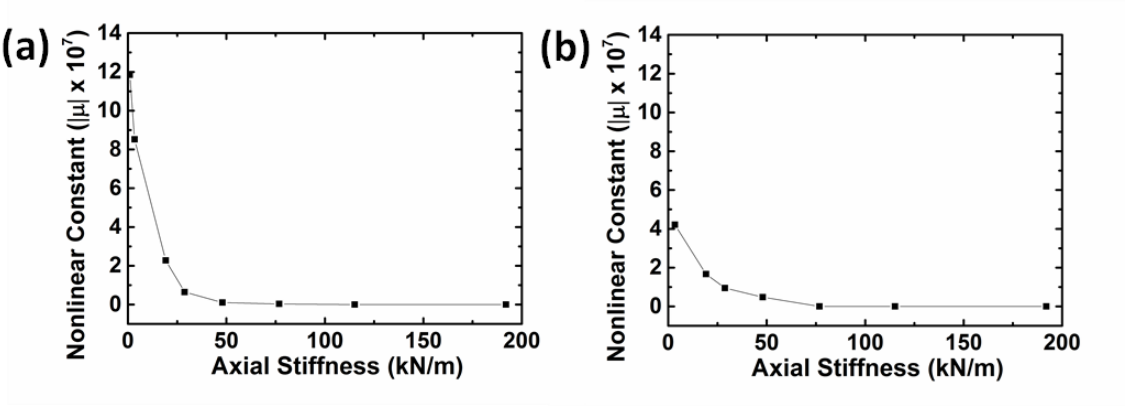

Figure 4.7. Estimated hardening and softening nonlinear constant μ as function of the axial stiffness of the coupling bridge, based on analysis of the dynamic response measured at the tip of the outer microcantilever: (a) Stiffness-hardening, and (b) stiffness-softening regions showing the generation of the nonlinear effects in the system for weak coupling (*cf.* Fig. 4.6); in these plots the absolute values of μ are depicted for better visualization, whereas the axial stiffness of the nanomembrane is estimated from its width using the equation $k_c=Etw/L$, with E=160 GPa, t=300 nm and L=5 μm, respectively.

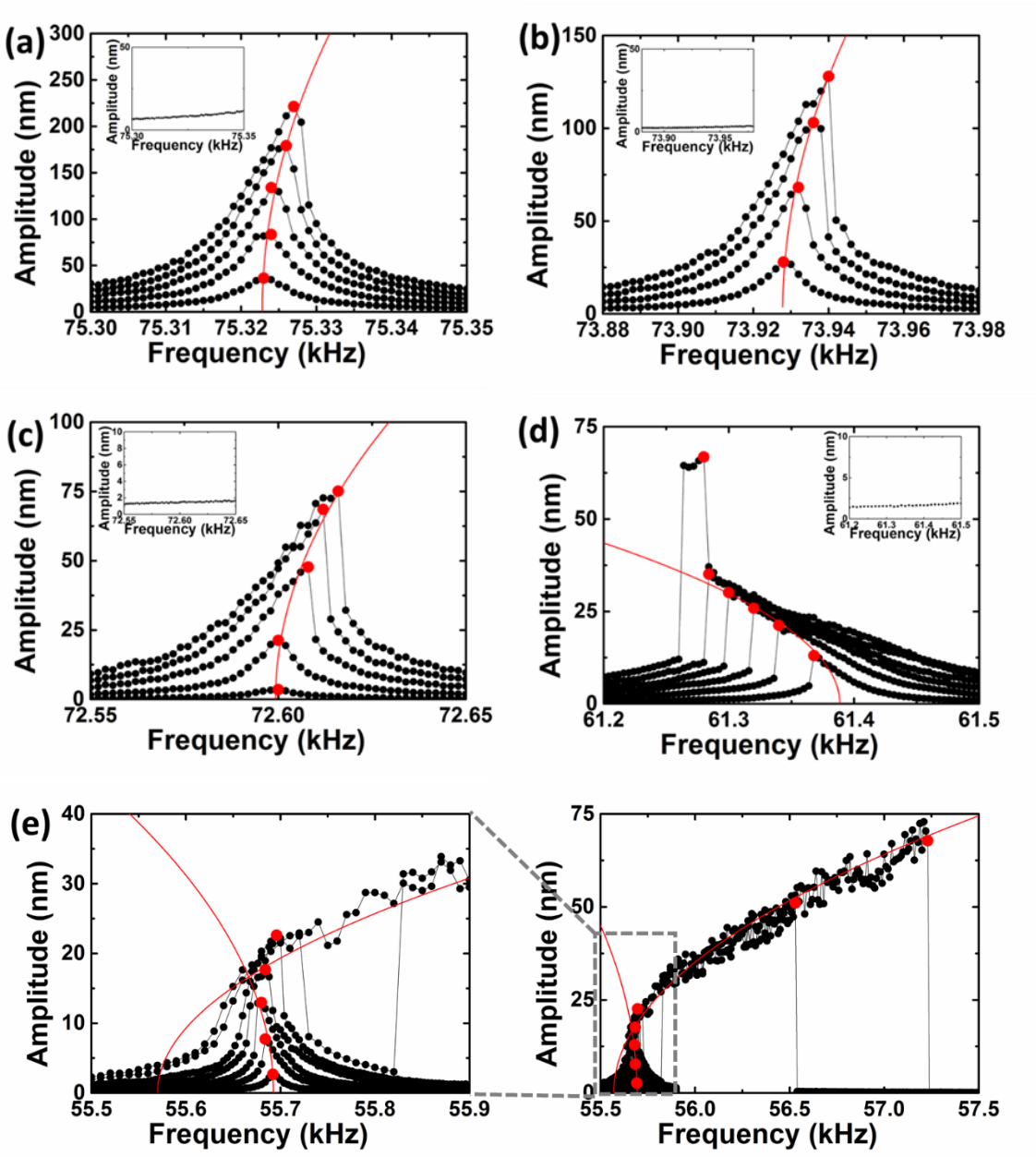

Figure 4.8. Nonlinear dynamic responses at the tip of the inner microcantilever for decreasing width w of the coupling bridge (nanomembrane) when the frequency is swept forward in a range close to the frequency of the in-phase mode: (a) w =5 μm, (b) w =3 μm, (c) w =2 μm, (d) w = 0.35 μm, and (e) w =0.1 μm (the plot on the left provides a magnified view of the plot in the right). In the insets the frequency spectra of the responses of the outer microcantilever at the same frequency range are shown. In each case the driving

voltage (V_{pp}) is gradually increased from a small to the large value in order to observe the transition of the nonlinear dynamic response under different forcing amplitudes, whereas the vacuum pressure (P) was kept constant at 8.0 mTorr. The nonlinear constant μ derived from the corresponding backbone curves (red lines) fitted to the drop amplitudes (red circles), was estimated as (a) $\mu = 3.18 \times 10^{-8}$ (b) $\mu = 2.43 \times 10^{-7}$, (c) $\mu = 9.98 \times 10^{-7}$, (d) $\mu = -3.89 \times 10^{-5}$ and (e) $\mu = -4.10 \times 10^{-5}$, 1.50×10^{-4} (for fitting the backbone curves the model (4-26) was used with l_0=1 nm).

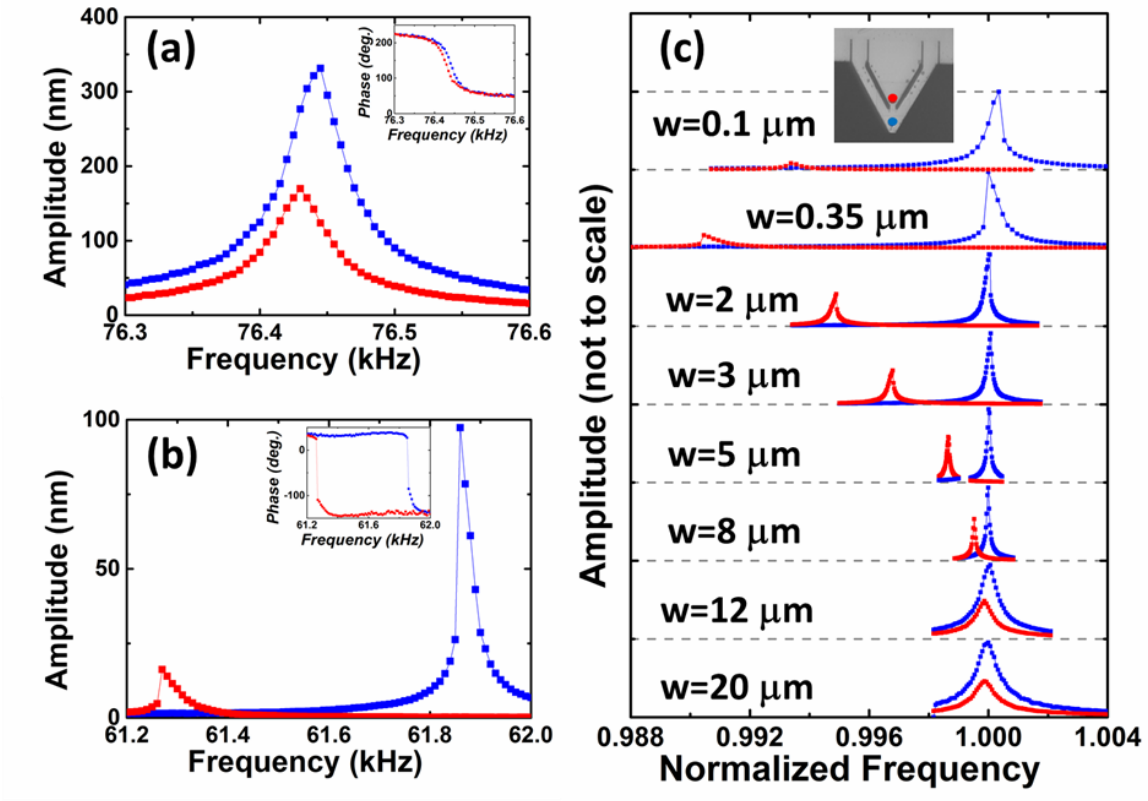

Figure 4.9. Dynamic response of the inner (red markers) and outer (blue markers) microcantilevers corresponding to different widths of the coupling bridge, showing the mode splitting giving rise to nonlinear localization in the limit of small widths: (a) w =12 μm (input voltage $V_{pp} = 300\ mV$) and (b) w =0.35 μm ($V_{pp} = 80\ mV$) (the insets depict the corresponding phases in the same frequency range); (c) normalized nonlinear dynamic responses of the two coupled microcantilevers for different widths of the coupling bridge, for forward frequency sweeps, at input voltages V_{pp}= 300 mV (for $w = 20$ mm and 12 mm), 100 mV (at $w = 8$ mm), 90 mV (at $w = 5$ mm), 80 mV (at w =3 mm, 2 mm and 0.35mm) and 50 mV (at $w = 0.1$ mm), and fixed vacuum pressure P = 8.0 mTorr; to better represent the mode splitting in (c), in the plot corresponding to each width the frequency is normalized with respect to the frequency of maximum response of the outer cantilever, and the amplitudes are normalized in the same manner (the inset in (c) shows the measurement points).

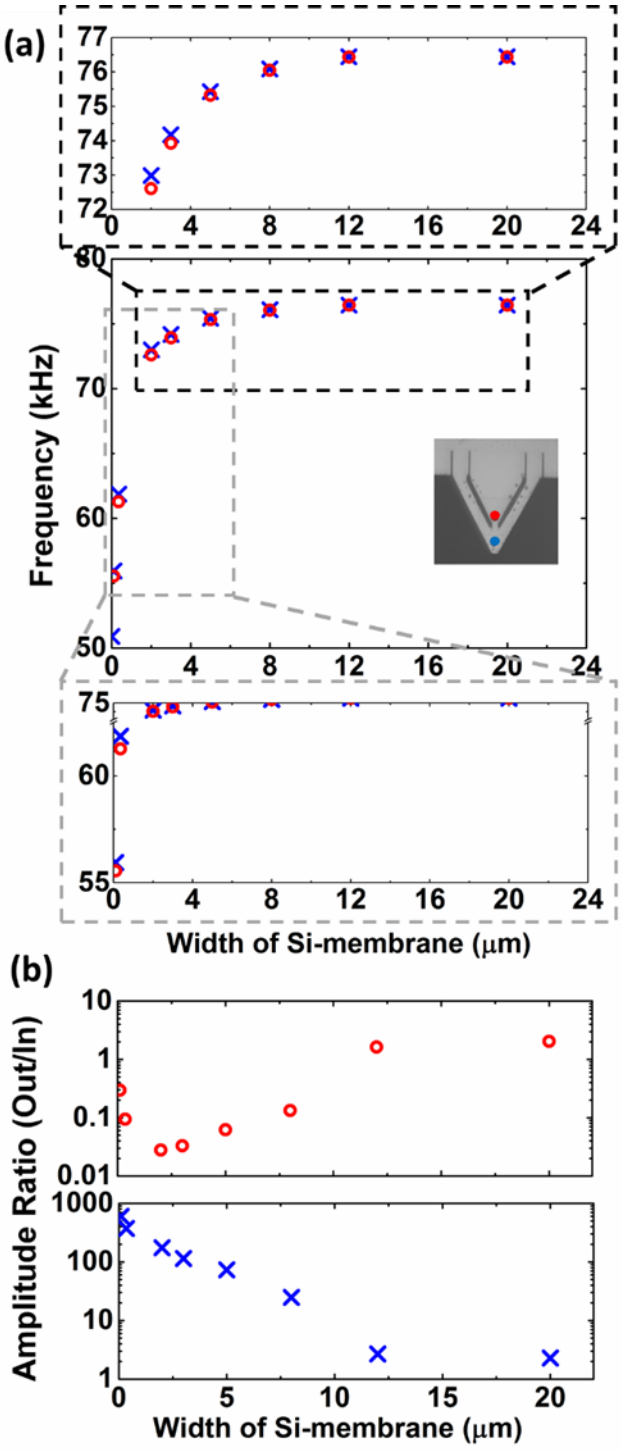

Figure 4.10. Mode splitting in the weakly coupled system: (a) Resonant frequencies of the inner (○) and the outer (×) microcantilevers for different widths of the coupling bridge (plots are magnified to provide better visualization of the resonant peak separation); (b) ratio of the amplitude of the outer cantilever to the amplitude of the inner cantilever at the corresponding resonant frequency as a function of the width of the nanomembrane; upper figure depicts localization of the response to the inner microcantilever, and lower figure localization to the outer microcantilever.

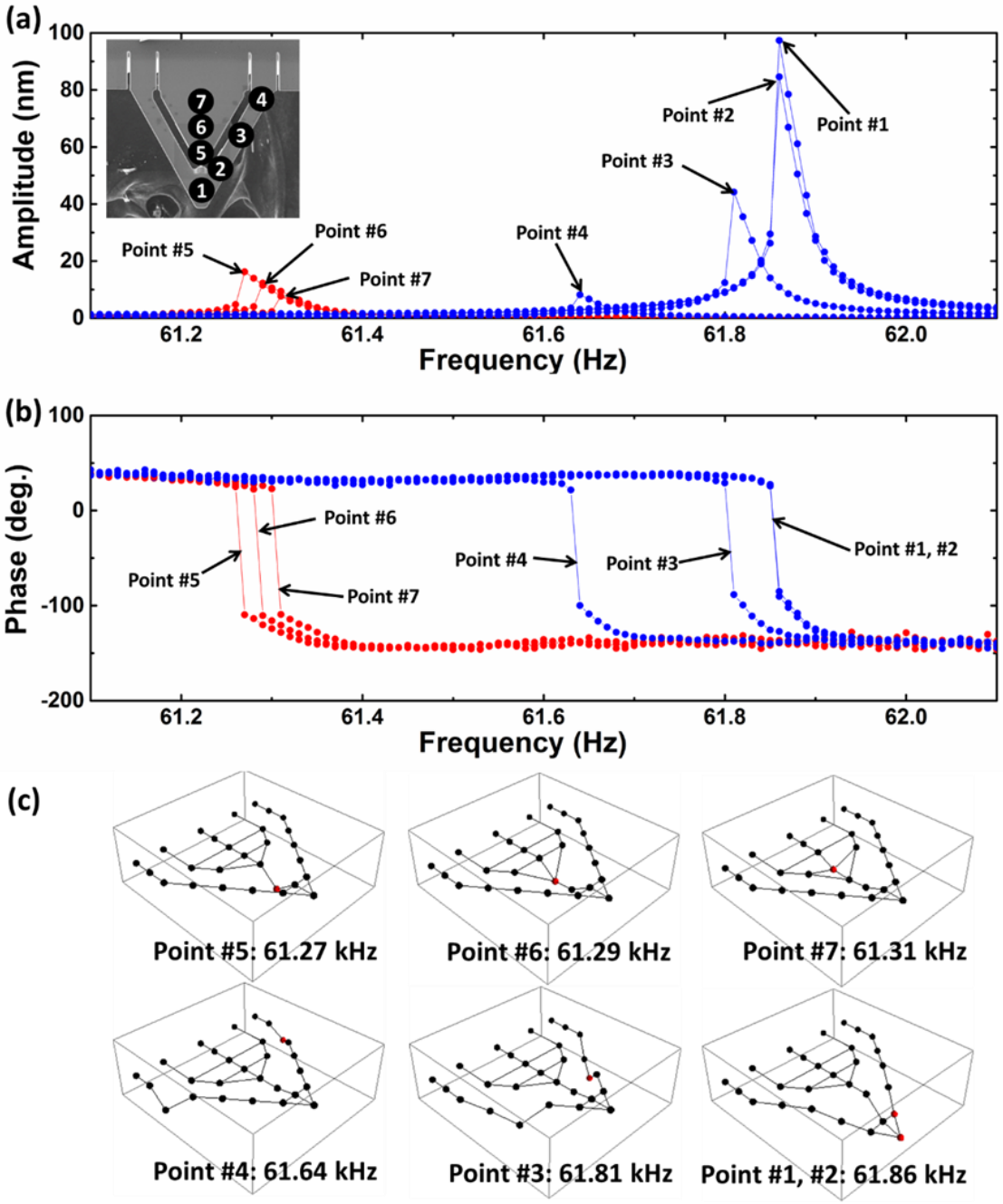

Figure 4.11. Shifting of the frequency responses, magnitudes and phases leading to mode splitting in the weakly coupled system for fixed input voltage $V_{pp} = 80\,mV$ and width of the coupling bridge w =0.35 μm, at seven sensing positions on the two microcantilevers shown in the inset (blue and red markers indicate the responses of the outer and the inner cantilevers, respectively): (a) Amplitudes, and (b) phases; (c) measured deflection shapes

of oscillation of the two microcantilevers at the resonance peak frequencies of each of the frequency responses of (a) and (b) (indicated by Points 1-7, corresponding to the different sensing locations), reconstructed from the frequency responses measured experimentally using laser microvibrometry.

TABLE

Sample No.	***w***	f_{p1}	f_{p2}	f_{p1}- f_{p2}	μ **(External cantilever)**	μ **(Inner cantilever)**
1	20 μm	76.44 kHz	76.43 kHz	0.01 kHz	0	N/A
2	12 μm	76.44 kHz	76.43 kHz	0.01 kHz	0	N/A
3	8 μm	76.09 kHz	76.05 kHz	0.04 kHz	3.45×10^{-9}	
4	5 μm	75.43 kHz	75.32 kHz	0.11 kHz	-4.80×10^{-8} $\rightarrow 1.04 \times 10^{-8}$	3.18×10^{-8}
5	3 μm	74.17 kHz	73.93 kHz	0.25 kHz	-9.46×10^{-8} $\rightarrow 6.47 \times 10^{-8}$	2.43×10^{-7},
6	2 μm	72.98 kHz	72.60 kHz	0.38 kHz	-1.67×10^{-7} $\rightarrow 2.28 \times 10^{-7}$	9.98×10^{-7}
7 (1st data)	0.35 μm	61.92 kHz	61.39 kHz	0.53 kHz	-4.21×10^{-7} $\rightarrow 8.52 \times 10^{-7}$	-3.89×10^{-5}
(2nd data)		61.86 kHz	61.27 kHz	0.59 kHz	N/A	N/A
8 (1st data)	0.1 μm	56.05 kHz	55.69 kHz	0.36 kHz	4.61×10^{-7} $\rightarrow 1.18 \times 10^{-6}$	-4.10×10^{-5} $\rightarrow 1.50 \times 10^{-4}$
(2nd data)		55.94 kHz	55.55 kHz	0.39 kHz	N/A	N/A

Table 4.1. Summary of key dimension and experimentally measured parameters for each sample; *w* is the width of the coupling membrane, f_{p1} the peak frequency at the external cantilever, f_{p2} the peak frequency at the internal cantilever, and μ the degree of the nonlinearity. Note that there exists 2 data sets for samples 7 and 8; the major difference in these data sets is the shift in the region of the resonance, potentially arising from the plastic elongation of the coupling membrane due to the excessive oscillation. Nonetheless, the peak frequency deviation f_{p1}- f_{p2} does not exhibit considerable change. The 1st data set is utilized for plotting Figs. 4.6 and 4.8, whereas Figs. 4.9 and 4.10 employed the 2nd data set.

REFERENCES

Blanchard, A., Gendelman, O., Bergman, L.A., McFarland, D.M., Vakakis, A., Boundary Layers of Mode Complexity in an Elastic Continuum with Discrete Damping, *J. Sound Vib*., in press (2014).

Chaste, J., Eichler, A., Moser, G., Ceballos, G., Rurali, R., Bachtold, A., A Nanomechanical Mass Sensor with Yoctogram Resolution, *Nature Nanotech.*, 7, 301-304 (2012).

Cho, H., Yu, M.-F., Vakakis, A.F., Bergman, L.A., McFarland, D.M., Tunable, broadband nonlinear nanomechanical resonator, *Nano Lett.*, 10, 1793-1798 (2010).

Cho, H., Jeong, B., Yu, M.-F., Vakakis, A., McFarland, D. M., Bergman, L., Nonlinear hardening and softening resonances in micromechanical cantilever-nanotube systems originated from nanoscale geometric nonlinearities, *Int. J. Sol. Struct.*, 49, 2059-2065 (2012a).

Cho H., Yu M.-F., Vakakis A., McFarland D.M., Bergman L.A., Dynamics of microcantilever integrated with geometric nonlinearity for stable and broadband nonlinear atomic force microscopy, *Surf. Science*, 606, 74-78 (2012b).

Ekinci, K.L., Yang, Y.T., Roukes, M.L., Ultimate limits to inertial mass sensing based upon nanoelectromechanical systems, *J. Appl. Phys.*, 95, 2682–2689 (2004).

Ekinci, K.L., Roukes, M.L., Nanoelectromechanical systems, *Rev. Sci. Instr*., 76, 061101 (2005).

Girssibl, F.J., Advances in Atomic Force Microscopy, *Rev. Mod. Phys*. 75, 949-983 (2003).

Goeders, K.M., Colton, J.S., Bottomley L.A., Microcantilevers: Sensing Chemical Interactions via Mechanical Motion, *Chem. Rev*., 108, 522-542 (2008).

Gruber, K., Horlacher, T., Castelli, R., Mader, A., Seeberger, P.H., Hermann, B.A., Cantilever Array Sensors Detect Specific Carbohydrate-Protein Interactions with Picomolar Sensitivity, *ACS Nano* 5, 3670-3678 (2011).

Jeong, B., Cho, H., Yu, M.-F., Vakakis, A., McFarland, D. M., Bergman, L.A.; Modeling and measurement of geometrically nonlinear damping in a microcantilever-nanotube system, *ACS Nano*, 10, 8547-8553 (2013).

Kacem, N., Hentz, S., Bifurcation topology tuning of a mixed behavior in nonlinear micromechanical resonators, *Appl. Phys. Lett.*, 95, 183104 (2009).

Kacem, N., Arcamone, J., Perez-Murano, F., Hentz, S., Dynamic range enhancement of nonlinear nanomechanical resonant cantilevers for highly sensitive NEMS gas/mass sensor applications, *J. Micromech. Microeng.*, 20, 045023 (2010).

Keum, H., Carlson, A., Ning, H., Mihi, A., Eisenhaure, J., Braun, P.V., Rogers, J.R., and Kim, S., Silicon Micro-Masonry Using Elastomeric Stamps for Three-Dimensional Microfabrication, *J. Micromech. Microeng.*, 22, 055018 (2012).

Kim, S., Wu, J., Carlson, A., Jin, S. H., Kovalsky, A., Glass, P., Liu, Z., Ahmed, N., Elgan, S.L., Chen, W., Ferreira, P.M., Sitti, M., Huang, Y., Rogers, J.A.; Microstructured elastomeric surfaces with reversible adhesion and examples of their use in deterministic assembly by transfer printing, *Proc. Natl. Aca. Sci. U. S. A.*, 107, 17095-17100 (2010).

Lavrik, N.V., Sepaniak, M.J., Datskos P.G., Cantilever Transducers as a Platform for Chemical and Biological Sensors, *Rev. Sci. Instrum*., 75, 2229-2253 (2004).

Li, M., Tang, H.X., Roukes, M.L., Ultra-Sensitive NEMS-based Cantilevers for Sensing, Scanned Probe and Very High-Frequency Applications, *Nature Nanotech*., 2, 114-120 (2007).

Madou, M.J., *Fundamentals of Microfabrication and Nanotechnology*, CRC Press (2011).

Naik A. K., Hanay M. S., Hiebert W. K., Feng X. L., Roukes M. L., Towards Single-Molecule Nanomechanical Mass Spectrometry, *Nature Nanotech*. 4:7, 445-450 (2009).

Rhoads, J., Shaw, S., Turner, K., Baskaran, R., Tunable microelectromechanical filters that exploit parametric resonance, *J. Vib. Acoust.*, 127, 423–430 (2005).

Stanton, S., McGehee, C., Clark, C.M., Mann, B.P., Nonlinear dynamics for broadband energy harvesting: Investigation of a bistable piezoelectric inertial generator, *Physica D*, 239, 640–653 (2010).

Vakakis, A.F., Gendelman, O., Bergman, L.A., McFarland, D.M., Kerschen, G., Lee, Y.S., *Passive Nonlinear Targeted Energy Transfer in Mechanical and Structural Systems*, Springer Verlag (2008).

Yang, S.Y., Carlson, A., Cheng, H., Yu, Q., Ahmed, N., Wu, J., Kim, S., Sitti, M., Ferreira, P.M., Huang, Y., Rogers, J.A., Elastomer surfaces with directionally dependent adhesion strength and their use in transfer printing with continuous roll-to-roll applications, *Adv. Mater.* 24, 2117-2122 (2012).

Zhong, Q., Innis, D., Kjoller, K., Elings, V.B., Fractured Polymer/Silica Fiber Surface Studied by Tapping Mode Atomic Force Microscopy, *Surf. Sci. Lett*. 290, L688 (1993).

Chapter 5

Concept for Nonlinear High-Frequency Atomic Force Microscopy: Microcantilever Coupled to a Nanomembrane

5.1 Introduction

In the third and final application considered in this work, we propose a new concept for high-frequency atomic force microscopy (AFM) based on the structural modification of a typical microcantilever used in AFM operations and coupling it with a nanomembrane that introduces strongly nonlinear effects through geometric nonlinearities. Special attention is given with respect to the practical implementation of this system by means of a feasible and convenient microfabrication process. Since its first introduction in 1986 (Binnig *et al.*, 1986), AFM has been studied in depth to investigate its underlying physics, and extend its capability as an advanced metrological tool at the atomic scale. Research efforts in the past few decades have proved that AFM is not only an effective yet accurate topography measurement tool with nanometer resolution, but also a tool that is capable of quantitative characterization and identification of the mechanical, electrical, thermal, and optical properties of tested samples (*e.g.*, temperature, optical transmittance, magnetic property and charge distribution).

One notable milestone in the advance of AFM was the development of tapping mode operation, also known as amplitude-modulated AFM (AM-AFM) (Martin *et al.*, 1987). In AM-AMF, the amplitude of the oscillation is kept nearly constant via a feedback

loop control as the microcantilever is harmonically driven. In this mode of operation, unlike contact mode operation, the stiction between the tip and the surface can be avoided, yet, unlike noncontact mode operation, the information on the composition underlying the superficial layer can be provided as the tip impacts the surface. In addition, measurement is accomplished in a non-destructive manner as the tip barely touches the surface in a short time scale. Thanks to the aforementioned advantages, AM-AFM has been widely utilized in studying biological structures such as DNA structure (Lyubchenko *et al.*, 1997), and proteins (Fritz *et al.*, 1995; Radmacher *et al.*, 1994).

A current limitation of AM-AFM is that the measurements upon which its operation is based, are performed at the frequency of base motion of the microcantilever. Hence, a recent research trend in AM-AFM focuses on the utilization of multiple frequencies, in particular harmonic frequencies that are above the main driving frequency, for simultaneous compositional mapping and topographic imaging. Early studies show that responses at higher harmonics are enhanced by the nonlinearity in the tip-sample interaction due to the contribution of external repulsive forces (Stark *et al.*, 2000). Intrinsic enhancement of higher harmonics due to nonlinearity in liquid environment was reported and utilized to generate the images of biological membranes with improved resolution (Preiner, *et al.*, 2007), and of mica (Xu, et al., 2009). Other work on multi-frequency AM-AFM intentionally excites higher harmonics; this concept was first introduced in so-called 'bi-modal AFM operation', where the 2^{nd} flexural mode of the microcantilever was intentionally excited to map the composition of the specimen surface through the enhanced contrast in the phase image of the 2^{nd} mode (Rodriguez *et al.*, 2004; Martinez *et al.*, 2006).

Bi-modal AFM has been adopted to generate high contrast images of DNA (Proksch, 2006) and anti-bodies (Martinez *et al.*, 2008), for nanotomography of elastomeric polypropylene (Dietz *et al.*, 2008), for identifying surface charges (Baumann *et al.*, 2010), and for testing protein structural flexibility (Martinez-Martin *et al.*, 2011). Current research in bi-modal AFM has been extended to utilize three eigenmode frequencies, where the 3rd harmonic excitation was employed as a 'knob' to control the penetration depth below the surface, in order to map the subsurface of soft materials (Solares *et al.*, 2010a and 2010b; Ebeling *et al.*, 2013).

The aforementioned approaches of utilizing the higher harmonics in AFM operation, however, bear a few limitations: The AFM system needs to be driven in a confined environment (liquid), or requires additional design of the electrical components of the system to drive the system intentionally at higher harmonic frequencies. In an effort to overcome these limitations, microcantilevers with specialized designs have been developed to intrinsically enhance the amplitudes of higher harmonics. One representative design has been presented where the tip of the microcantilever was placed off the central axis to intentionally generate a torsional mode (Sahin *et al.*, 2007) and hence to a harmonic other than the harmonic of the fundamental bending mode; this torsional AFM microcantilever successfully generated resolution-enhanced images based on which protein structural flexibility could be studied (Dong *et al.*, 2009). Another design has been suggested in a form of a two-field AFM cantilever (Sadewasser *et al.*, 2006), based on enhancement of the higher harmonics of the measured response through internal resonance

activated by the nonlinear tip-sample interaction, and in the design has been studied numerically for non-contacting mode of AFM operation (Hacker *et al.*, 2012).

In this Chapter we propose a new design for an AFM cantilever system, where nonlinear *1:n* internal resonance is intentionally implemented and utilized to enhance the n^{th} harmonic component of the measured response during AM-AFM operation with a single driving frequency. To imbue the microcantilever with a *1:n* eigenfrequency ratio, an inner paddle consisting of a silicon nanomembrane is integrated on a commercially available AFM cantilever by the transfer-printing technique (Kim *et al.*, 2010). In turn, the dimensions of the inner paddle is controlled to accomplish the desired *1:n* eigenfrequency ratio based on a representative analytical model of the system. The enhancement of the n^{th} harmonic component by the internal resonance is confirmed by numerical simulation and experimental measurements. Moreover, the developed microcantilever system is further tested with a heterogeneous sample consisting of two different polymers, to validate the capability of this new design for generating a high contrast compositional map of the target specimen.

5.2 Theoretical Analysis

5.2.1. System Description and Proposed Concept

Figure 5.1 depicts the schematic view of the proposed nonlinear AFM design. It consists of a base microcantilever with an internal paddle in the form of an attached nanomembrane. The base cantilever depicted in light gray in the Figure resembles the physical

configuration and dimensions of a typical commercially available AFM cantilever, except its structural modification by a middle cavity. The nanomembrane, depicted in dark gray in Fig. 5.1, is placed above this cavity forming another (inner) clamped-free cantilever coupled to the base microcantilever. These two components behave like a system of two coupled oscillators, involving in-phase and out-of-phase modes between the base microcantilever and the inner nanoscale paddle when the integrated flexible system oscillates.

The geometry of the inner paddle is carefully designed to enforce a 1:*n* resonance between two selected bending modes of the integrated system. When in tapping-mode AFM operation, the nonlinear interactions between the system and the surface of the specimen activate a nonlinear internal resonance between the two bending modes, whereby nonlinear energy transfer from the directly excited lower (fundamental) in-phase bending mode to the higher out-of-phase bending mode takes place; in turn, this low-to-high frequency energy transfer enhances the *n*-th harmonic response of the inner paddle response which is measured for post-processing. We note that the much smaller thickness of the nanoscale paddle enables the design of the surface area of the paddle to be large enough in order to perform the required non-contacting AFM laser measurements upon which the operation of the proposed system relies. As a result, the imaging and mapping operation of the nonlinear AFM system is based on the amplitude, and, more importantly, on the phase of the *n*-th harmonic, in contrast to current AFM operation which is based on the fundamental harmonic, *i.e.*, the frequency of base excitation. As shown in this Chapter, this greatly enhances the resolution capacity of the proposed AFM system.

5.2.2 EQUATIONS OF MOTION

The representative lumped-parameter reduced-order model of the system is depicted in Fig. 5.2. Assuming that the base microcantilever and the inner nanoscale paddle oscillate in their fundamental bending modes, and due to the large discrepancy in their dimensions, each structural component is regarded as a discrete spring-mass system. Here, m, k, c, and x denote the effective mass, stiffness, damping coefficient, and displacement, where the subscripts 1 and 2 denote the base microcantilever and inner paddle, respectively. The system is driven by a harmonic base excitation during practical AFM operation, expressed as $y_0 \cos \omega t$. Additionally, the mass m_1 of the base microcantilever is misplaced by an amount equal to x_0, which represents the static misalignment between the tip and the sample at their equilibrium positions.

Based on this simplified model the equations of the motion are expressed as:

$$\begin{aligned} m_1\ddot{x}_1 + c_1\dot{x}_1 + k_1x_1 + k_2(x_1 - x_2) + c_2(\dot{x}_1 - \dot{x}_2) &= k_1y_0\cos\omega_d t + c_1y_0\omega\sin\omega_d t + F_{ts}(x_1) \\ m_2\ddot{x}_2 + k_2(x_2 - x_1) + c_2(\dot{x}_2 - \dot{x}_1) &= 0 \end{aligned} \tag{5-1}$$

In Eq. (5-1), $F_{ts}(x_1)$ is the nonlinear force generated by the interaction between the tip of the base cantilever and the surface of the target specimen. This interaction force depends on the conditions of AFM operation and the surface of the sample; that is, whether the tip is in the range of an attractive or repulsive interaction force, whether the environment is humid or not (or if the specimen is in liquid or in air), or whether the surface is charged or not.

In the following discussion we consider the case when the tip is tapping the surface without static charge, *i.e.*, undergoing an attractive force due to the van der Waals

interaction and a repulsive force generated due to the contact of the AFM tip and the compliant sample. These two forces can be mathematically modeled by employing the Derjaguin-Müller-Toporov (DMT) contact model (Derjaguin *et al*., 1980; Müller *et al*., 1980), and expressing $F_{ts}(x_1)$ as follows,

$$F_{ts}(x_1) = \begin{cases} -\dfrac{HR}{6(x_0 + x_1)^2} & (x_0 + x_1 > a_0 \ - \ no\,contact) \\ -\dfrac{HR}{6a_0^2} + \dfrac{4}{3}E^*\sqrt{R}\left[a_0 - (x_0 + x_1)\right]^{3/2} & (x_0 + x_1 \le a_0 \ - \ contact) \end{cases} \tag{5-2}$$

where H is Hamakar constant, R the radius of curvature at the tip, E^* the effective elastic modulus of the tip-sample interaction, and a_0 the intermolecular distance of the specimen. It is noteworthy that $F_{ts}(x_1)$ is a discrete function depending on the amplitude of the displacement x_1: The van der Waals force is the sole attractive interaction force when the tip is not in contact with the surface of the specimen, whereas the repulsive force from the elastic compliance of the specimen becomes dominant when contact occurs.

To facilitate the analysis in the following sections Eq. (5-1) is further transformed into normalized, non-dimensionalized form by introducing the following parameters,

$$\begin{gathered} \omega_{xn} \equiv \sqrt{\frac{k_n}{m_1}}, \quad \delta \equiv \frac{m_2}{m_1}, \ \tilde{c}_n \equiv \frac{c_n}{m_1\omega_{m1}}, \ \tilde{k}_n \equiv \frac{\omega_{xn}^2}{\omega_{m1}^2}, \ \tilde{x}_n \equiv \frac{x_n}{l_0}, \quad \tilde{a}_0 \equiv \frac{a_0}{l_0} \\ \tau \equiv \omega_{m1}t, \ (\ )' \equiv \frac{d}{d\tau}, \ \Omega_d \equiv \frac{\omega_d}{\omega_{m1}}, \ K \equiv m_1\omega_{m1}^2, \ \tilde{y}_0 \equiv \frac{y_0}{l_0} \end{gathered} \tag{5-3}$$

where the subscript n denotes the base cantilever for n = 1, and the inner paddle for n = 2, and the new parameters, ω_{m1} and l_0, denote the fundamental eigenfrequency of the integrated microcantilever – nanomembrane system corresponding to the in-phase bending mode and the characteristic length of the system, respectively.

Applying (5-3) to (5-1) and (5-2), the final form of the normalized equations of motion are expressed as follows:

$$\begin{aligned} &\tilde{x}_1'' + \tilde{c}_1\tilde{x}_1' + \tilde{k}_1\tilde{x}_1 + \tilde{c}_2(\tilde{x}_1' - \tilde{x}_2') + \tilde{k}_2(\tilde{x}_1 - \tilde{x}_2) = \tilde{k}_1\tilde{y}_0\cos\Omega_d\tau + \left(Kl_0\right)^{-1} F_{ts}(\tilde{x}_1) \\ &\delta\tilde{x}_2'' + \tilde{c}_2(\tilde{x}_2' - \tilde{x}_1') + \tilde{k}_2(\tilde{x}_2 - \tilde{x}_1) = 0 \end{aligned} \tag{5-4a}$$

$$F_{ts}(\tilde{x}_1) = \begin{cases} -\dfrac{HR}{6l_0^2(\tilde{x}_0 + \tilde{x}_1)^2} & (\tilde{x}_1 > \tilde{a}_0 - \tilde{x}_0) \\ -\dfrac{HR}{6l_0^2\tilde{a}_0^2} + \dfrac{4}{3}E^*\sqrt{R}l_0^{3/2}\left[\tilde{a}_0 - (\tilde{x}_0 + \tilde{x}_1)\right]^{3/2} & (\tilde{x}_1 \le \tilde{a}_0 - \tilde{x}_0) \end{cases} \tag{5-4b}$$

This system is used in the computational study presented in the next section.

5.2.3 Parameter Determination for Internal Resonance

In order to determine the geometric parameters for implementing the nonlinear internal resonance behavior in the system described by Eq. (5-1), the discussion now addresses the necessary conditions for the realization of the *1:n* internal resonance, and the design that implements practically these conditions.

The internal resonance, by its definition, is a nonlinear transfer of vibration energy between the modes of the dynamical system involved in the internal resonance, even when these modes are well-separated in frequency. It is a phenomenon unrealizable in a linear system where the energy stored in a single mode cannot be transferred to any other mode, unless this mode is closely spaced in frequency; indeed, in the linear system the stored energy in a mode would merely remain constant (for a conservative system) or would be dissipated by the inherent modal damping (for a dissipative system). Accordingly, one can

deduce the first condition for realization of internal resonance in a dynamical system, which is the existence of *nonlinearity*. In the proposed design this requirement is well satisfied by the nonlinear tip-sample interaction force, expressed as the highly nonlinear function in terms of x_1 on the right-hand-side of Eq. (5-2). In addition to existence of system nonlinearity, *an internal resonance requires that the linearized eigenfrequencies of the modes of interest should satisfy a rational relationship* (Sanders *et al*., 2007; Vakakis *et al*., 2008). This is a critical condition that can be satisfied by proper design of the system parameters through a parametric study.

The linearized eigenfrequencies of a system can be deduced by neglecting the nonlinear, damping and forcing terms and performing modal analysis. Undoubtfully, modeling the entire system on the basis of continuum mechanics will provide the most accurate expressions for the corresponding eigenfrequencies; however, if the geometry of the given dynamic system is complicated (as in the system considered in this Chapter), deriving analytical solutions for eigenfrequencies is not possible, and resort to approximate or numerical methods is required. Considering the system examined, there is large discrepancy in the physical dimensions between the base microcantilever and the inner paddle realized by the transfer-printing technique. Moreover, the aspect ratio between the length and width of each cantilever is considerably large. These geometrical features, coupled with the fact that we will confine our analysis to a restricted frequency range containing two linearized modes, allow us to utilize approximated expressions for clamped-free cantilevers for modeling.

In particular, we perform an approximate analysis by considering the system partitioned into three basic components. Namely, we consider the set of two identical base cantilevers lying in parallel of Fig. 5.1 as the lumped mass with subscript '1' in the model of Fig. 5.2; the inner paddle (attached nanomembrane) denoted by the mass with subscript '2' in Fig. 5.2; and, finally, the remainder of the frame of the base cantilever (after excluding the two parallel cantilevers), including the tip. Moreover, all components of the system are made out of Silicon.

Hence, to obtain approximate expressions for the linearized eigenfrequencies of the system, we neglect in Eq. (5-1) the nonlinear forces due to tip-sample interactions, the harmonic base excitation and the damping terms, and consider the following modified linearized equations of motion:

$$\begin{aligned} &(m_e + M)\ddot{x}_1 + k_1 x_1 + k_2(x_1 - x_2) = 0 \\ &m_2\ddot{x}_2 + k_2(x_2 - x_1) = 0 \end{aligned} \tag{5-5}$$

where for design purposes the effective mass m_1 of the base microcantilever was expressed in terms of the effective mass m_e of the set of external cantilevers, and the added mass M of the remainder of the base microcantilever, so that in holds that $m_1 = m_e + M$. It is noteworthy that the remainder of the external frame only serves as a joint and does not affect the stiffness of the set of the external cantilevers; thus it can be approximated as the bulk of mass M in Eq. (5-5). Employing the well-known expression for the effective mass and stiffness of a clamped-free rectangular cantilever, m_e, m_2, k_1 and k_2 in Eq. (5-5) can be expressed in terms of the physical parameters of the system as follows:

$$m_e = \frac{33}{70}\rho_{si} l_1 w_1 t_1,\ \ m_2 = \frac{33}{140}\rho_{si} l_2 w_2 t_2 = \alpha\beta\gamma m_e,$$
$$k_1 = \frac{E_{si} w_1 t_1^3}{2l_1^3},\ \ k_2 = \frac{E_{si} w_2 t_2^3}{4l_2^3} = \frac{\alpha^3\gamma}{\beta^3} k_1 \tag{5-6}$$

where l is the length, w the width and t the thickness of each microcantilever, with the subscript denoting the set of the external cantilever (1) and the inner paddle (2); also, E_{si} and ρ_{Si} are the Young's modulus and the density of silicon, respectively. Note that m_2 and k_2 can be correlated to m_e and k_1, respectively, leading in further simplifications form by applying the following relations,

$$\alpha = \frac{t_2}{t_1},\ \beta = \frac{l_2}{l_1},\ \gamma = \frac{w_2}{2w_1} \tag{5-7}$$

where α, β and γ are the thickness, length and width ratio between the inner paddle and the base cantilevers, respectively. It is expected that the previous expressions for the effective mass and stiffness of each of the base microcantilevers and the inner paddle, as well as the following parametric design are approximately valid when these flexible systems oscillate in their fundamental bending modes. However, the previous expressions cannot account for higher modal interactions involving higher-order modes of the flexible system of Fig. 5.1; for such more complicated dynamical responses one needs to resort to computational analysis, such as finite-element simulations, but one would lose the capacity for deriving analytical expressions for the leading eigenfrequencies, as performed below.

Applying Eq. (5-6) to Eq. (5-5) followed by modal analysis, the expression for the two leading-order eigenfrequencies of the system can be expressed in terms of the normalized parameters α, β and γ as follows:

$$\omega_{m1,2} = \omega_L \left\{ \frac{\left(\alpha^2\left(1+\alpha\beta\gamma+\mu\right)+\beta^4\right) \mp \sqrt{\left(\left(\alpha^2\left(1+\alpha\beta\gamma+\mu\right)+\beta^4\right)^2 - 4\alpha^2\beta^4\left(1+\mu\right)\right)}}{2\beta^4(1+\mu)} \right\}^{1/2}$$

(5-8)

In Eq. (5-8), there are two newly introduced parameters, namely, $\mu = M/m_1$, the mass ratio of the remainder in the frame of the base microstructure and the parallel set of external microcantilevers; and ω_L, the resonance frequency of each of the base microcantilevers in the absence of the remainder, $\omega_L=(k_1/m_e)^{1/2}=1.03(E_{si}\, t_1^2/(\rho_{si}\, l_1^4))^{1/2}$. Eq. (5-8) serves as a convenient tool for determining the system parameters for realization of an *1:n* internal resonance; *e.g.*, the value of β can be deduced when α and γ are fixed, by solving for $\omega_{m2} / \omega_{m1}=n$ where n is an integer. The validity of Eq. (5-8) for determining the physical parameters will be further discussed in Section 5.4.1.

5.3 Device Fabrication

In Fig. 5.3, the fabrication process is summarized. As a base AFM cantilever, NSC-14 from MikroMasch was selected, depicted as an inset SEM (scanning electron microscopy) image in Fig. 5.3a. First, ion-milling process was performed inside a DB-235 FIB (focused ion-beam) machine to form a cavity in the middle of AFM cantilever, as shown in Fig. 5.3b. This is followed by transferring a silicon ink, in the form of a square-shaped slice of silicon membrane with a thickness of 300 nm prepared on SOI (silicon-on-insulator) wafer through conventional microfabrication technique (Kim *et al.*, 2010), as shown in Fig. 5.3c.

The adhesion of the transferred silicon membrane to the AFM cantilever is conveniently implemented by Si-SiO_2-Si fusion bonding as the fabricated cantilever undergoes the annealing process in a furnace at a temperature of 1000°C for 5 minutes (Fig. 5.3d). With adhesion formed, the silicon membrane is carved to form an inner paddle, as shown in Fig. 5.3e. The length of this inner paddle can be gradually controlled by removing the free end by step-wise attempts, consequently realizing the microcantilever with an attached nanomembrane for *1:n* internal resonance, as shown in Fig. 5.3f. It is noteworthy that the fabrication process depicted in Fig. 5.3c~f can be implemented as a batch-fabrication process, although serial integration and patterning were performed in this research. The feasibility of batch-fabrication paves the way for practical implementation of the proposed nonlinear microcantilever design, for mass production and cost-effective commercialization.

5.4 Results

5.4.1. CHARACTERIZATION

To implement the microcantilever in internal resonance, Eq. (5-8) is revisited with the physical parameters of the microcantilever coupled with a nanomembrane. The thickness ratio α and the width ratio γ are calculated as,

$$\alpha = \frac{t_2}{t_1} = \frac{300nm}{1.6\mu m} = 0.188, \qquad \gamma = \frac{w_2}{2w_1} = \frac{12\mu m}{2\times 11\mu m} = 0.545 \tag{5-9}$$

Then the mass ratio μ is computed as follows,

$$\mu = \frac{m_{rem} + m_{tip}}{m_e} = \frac{l_{rem} w_{rem} t_{rem} + 0.333\pi r_{tip}^2 h_{tip}}{0.236 l_1 (2w_1) t_1} = 2.609 \quad (5\text{-}10)$$

where l_{rem} = 27 μm, w_{rem} = 36 μm, and t_{rem} = 1.6 μm are the length, width and thickness of the remainder of the basic microcantilever, respectively; also, r_{tip} and h_{tip} are the radius and height of the tip, respectively. For evaluating m_e, the numerical value l_1=90 μm was applied whereas the values from Eq. (5-9) were used to estimate the parameters w_1 and t_1. Applying Eq. (5-9) and (5-10) to Eq. (5-8) and assuming that $\omega_{m2} / \omega_{m1} = n$ where n is an integer so that the condition of *1:n* internal resonance could be satisfied, we can deduce the value of β corresponding to two leading modal frequencies of the integrated system.

The scope of this research is focused on the cases n = 3 or 5, leading to 1:3 or 1:5 internal resonance, respectively. Accordingly, the corresponding values of β for these two cases are calculated as,

$$\beta_{1:3} = \frac{l_2}{l_1} = \frac{31.14\mu m}{90\mu m} = 0.346 \quad \text{or} \quad \beta_{1:5} = \frac{l_2}{l_1} = \frac{24.12\mu m}{90\mu m} = 0.268 \quad (5\text{-}11)$$

In the actual practical implementation and fabrication, the length of the inner paddle was gradually adjusted to realize the 1:3 internal resonance. At each attempt of the structural modification, the eigenfrequencies of the corresponding integrated microcantilever-nanomembrane system were measured by its frequency spectrum generated by the thermomechanical vibration (refer to Section 4.4.1 for the details of the experimental setup). The measurements of the eigenfrequencies were performed in both ambient (750 Torr) and high vacuum (4.5 mTorr) environments, in order to quantify any possible shift in the eigenfrequencies owing to ambient air damping effect.

In Figure 5.4 we depict typical experimental frequency spectra produced in the aforementioned manner, based on which measurement we assessed the progress of the structural modification and the gradual realization of the condition of internal resonance in the integrated system. The particular measurements presented in Fig. 5.4 correspond to the finalized design of the system possessing approximately 1:3 ratio between its two leading modes; the lowest-frequency (fundamental) mode corresponds to in-phase oscillations between the base cantilever and the inner paddle, whereas the higher-frequency second mode corresponds to out-of-phase oscillations. Note that for both modes, both the base cantilever and the inner paddle oscillate in their individual fundamental cantilever bending modes, which is in agreement to the assumptions made previously for constructing the theoretical models.

It is noteworthy that for the frequency spectra presented in Fig. 5.4 two sensing points were arbitrarily selected, surmising that the oscillation amplitude at each of these points will be maximized at the different mode, *i.e*, the point indicated by the red dot on the inner paddle for the in-phase mode, and the point corresponding to the blue dot for the out-of-phase mode. The results of Fig. 5.4 clearly depict the two leading resonance frequencies, measured at 122.8 kHz and 394.4 kHz in ambient environment, and at 123.4 kHz and 397.8 kHz in high vacuum. As expected, the air damping effect produces lower shifts in the resonance frequencies, as expected from linear vibration theory where increase damping causes a small decrease of the damped eigenfrequencies. This implies that the inherent structural damping of the linear integrated system in the absence of tip-sample interactions is small. In fact, in our study these frequency shifts are sufficiently small to be

neglected from further consideration, so the frequency ratios between the in-phase and the out-of-phase linear modes is considered to be almost constant (*i.e.*, 1/3.22 for high vacuum, and 1/3.21 for ambient environment). This implies that the effect of air pressure on the linearized eigenfrequencies due the ambient environment can be neglected in the proposed system.

To validate the previous theoretical design, the experimentally measured eigenfrequencies by the aforementioned manner are compared to the analytical estimations based on Eq. (5-8) for variation of the length ratio β; this comparison is depicted in Fig. 5.5. Considering the plot of Fig. 5.5a, we note that the estimated resonance frequencies from Eq. (5-8) are shown with the red line corresponding to the in-phase mode and the blue line to the out-of-phase mode; the green line is indicating the frequency corresponding to three times the estimated resonance frequency of the in-phase mode, whose intersection with the blue line indicates the desired design point for realization of the 1:3 internal resonance. The experimentally measured eigenfrequencies denoted by red (in-phase) and blue (out-of-phase) markers show good agreement with the analytical estimations. The small discrepancy is possibly due to the simplifying assumptions upon which the theoretical model Eq. (5-8) is based.

The plot of Fig. 5.5b depicts the variation of the frequency ratio between the in-phase and out-of-phase resonance frequencies following the variation of the normalized length ratio β. The analytical estimation based on Eq. (5-8), denoted by the solid line in Fig. 5.5b, exhibits a good fitting with the experimental results (black markers). In fact, the deviation between the analytical estimation and the experimental measurement is observed

to be even smaller than in the plot of Fig. 5.5a, indicating that the simplifying assumptions of the theoretical model affects less the frequency ratio.

In synopsis, good overall agreement between the analytical estimation and the experimental measurement of the eigenfrequencies of the integrated system is deduced, indicating that Eq. (5-8) can be used as an accurate predictive theoretical tool for designing the length ratio between the base microcantilever and the inner paddle (nanomembrane) for realization of *1:n* internal resonance, especially when the eigenfrequency ratio is utilized as a basis for the design.

The final microcantilever system incorporating 1:3 internal resonance shown in Fig. 5.4, was further characterized by experimentally measuring its frequency response under harmonic force excitation. In this characterization, the measurement was performed under ambient environment (pressure of 750 Torr) with AC voltage of 1 V applied to the piezoelectric shaker where the microcantilever system was mounted. In Fig. 5.6, two frequency responses of this system are presented, one in a lower frequency range corresponding to the in-phase mode (Fig. 5.6a), and other in a higher frequency range in the neighborhood of the out-of-phase (Fig. 5.6b). In the absence of tip-sample nonlinear interactions the frequency response near the in-phase mode exhibits the expected linear dynamic behavior, and the corresponding resonance frequency was measured at 122.8 kHz, which is identical to the measured resonance frequency due to thermal noise vibration.

In the vicinity of out-of-phase mode, however, the behavior of the frequency response is not as clear as that of in-phase mode, since there exist two peaks in that region, as depicted in the inset of Fig. 5.6b. The possible sources for this outcome could be

attributed on unaccounted effects due to imperfect adhesion between the microcantilever and the nanomembrane (inner paddle), which sometimes is unavoidable during the fabrication process. The lower plots at Figs. 5.6a and 5.6b show the shape of the oscillation at the maximum peaks of in-phase and out-of-phase modes, respectively; these shapes are constructed from the experimentally measured amplitudes and phases at the points of the interest when an AC voltage of 1 V is applied at the shaker. By interpreting the direction of the motion denoted by the embedded arrows, one can confirm that the frequency responses in Fig. 5.6 correspond to the in-phase and out-of-phase modes, respectively. It is noteworthy that the tip of the base cantilever remains almost stationary while the tip of the inner paddle is oscillating at a relatively large amplitude in the case of the out-of-phase mode. Hence, to extract the amplitude of the higher harmonic effectively, the sensing position for the proposed nonlinear, high-frequency AFM operation needs be on the inner paddle.

5.4.2. SIMULATIONS FOR $1:n$ INTERNAL RESONANCE

Before conducting the real AFM operation with the developed microcantilever system, numerical simulations of Eq. (5-4) were performed to estimate the amplitude and phase variations of the harmonics of the measured responses for variation of the clearance (x_0) between the tip and the surface of the specimen, based on the model formulated in Section 5.2.2. Assuming that Eq. (5-8) provides a reliable estimation of the two lowest eigenfrequencies, Eq. (5-9) and Eq. (5-10) are utilized again to determine the physical

parameters of the system for *1:n* internal resonance. Accordingly, the normalized parameter values for realizing 1:3 internal resonance are calculated as,

$$\tilde{k}_1 = 1.011,\ \tilde{k}_2 = 8.83\times10^{-2},\ \delta = 9.8\times10^{-3},\ K = 4.89N/m \tag{5-12}$$

whereas, for 1:5 internal resonance these values are:

$$\tilde{k}_1 = 1.008,\ \tilde{k}_2 = 1.89\times10^{-2},\ \delta = 7.61\times10^{-3},\ K = 4.89N/m \tag{5-13}$$

The remaining coefficients in Eq. (5-4) were arbitrarily chosen to be close to typical AFM systems used in practice:

$$\begin{aligned}&\tilde{c}_1 = 0.005,\quad \tilde{c}_2 = 0.005,\quad l_0 = 10^{-9}m,\quad \Omega_d = 1,\\ &\tilde{y}_0 = 1,\quad R = 30nm,\quad H = 3\times10^{-19}J\end{aligned} \tag{5-14}$$

It should be noted that choosing l_0=1 nm facilitates the analysis as the normalized amplitudes will be automatically expressed using the characteristic length of 1 nm. The yet undefined parameters, such as the effective Young's modulus (E^*) and the initial clearance between the tip and the sample (x_0), will be employed as the controlled parameters in the forthcoming simulations.

The numerical simulations were performed by solving Eq. (5-4) directly with zero initial conditions utilizing a Runge-Kutta method implemented in Matlab. The steady state time-domain response was then transformed into the frequency-domain response by numerical Fast Fourier Transforms. In this manner, the amplitude and the phase information for each frequency component of a measured steady state response was identified.

First, the case of 1:3 internal resonance utilizing Eq. (5-12) is investigated. Fig. 5.7 depicts the frequency spectra of x_1 (the response of the tip of the base microcantilever) and x_2 (the tip response of the inner paddle), when the static separation from the surface of the specimen (clearance x_0) is varied from 100 nm to 250 nm for three cases of the effective Young's modulus (E^*): 0.1 GPa (Fig. 5.7a), 1 GPa (Fig. 5.7b) and 10 GPa (Fig. 5.7c). As depicted by the responses of x_1 in Fig. 5.7, the dominant peak is observed at $\Omega = 1$ for each case of E^*. This is expected since the driving normalized frequency of the base harmonic excitation of the microcantilever, as well as the first normalized eigenfrequency of the system is equal to unity (*i.e.*, $\Omega_d = \Omega_{m1} = 1$). In addition to this dominant peak, however, there exist smaller peaks at higher harmonics (*i.e.*, for $\Omega = n\Omega_d$, where $n = 2,3,\ldots$) owing to the strong nonlinearity arising from the tip-sample interaction.

In the responses of x_2 of Fig. 5.7, it is observed that the amplitude of the third harmonic at normalized frequency $3\Omega_d$ is amplified when compared to the corresponding responses of x_1. This can be explained by the dynamical mechanism of 1:3 internal resonance: Due to the 1:3 internal resonance the nonlinear tip-sample interaction leads to nonlinear energy transfer from the directly excited lower (fundamental) eigenfrequency to the third harmonic of this frequency, which, by design, corresponds to the second eigenfrequency; hence, relatively strong excitation of the higher-frequency, out-of-phase mode of the cantilever system is realized, upon which the proposed nonlinear, high-frequency AFM operation is performed.

Since the laser is focused on the inner paddle in the practical realization of the proposed AFM operation, any further discussion regarding the simulated dynamic response

is limited to the response of the inner paddle, x_2. In Fig. 5.8, the amplitude and phase at $\Omega = 1$ and 3 with respect to the static equilibrium separation x_0 is plotted for E*=0.1, 1 and 10 GPa. Note that since the free linear oscillation amplitude at the drive frequency (*i.e.*, at $\Omega = 1$) is 200 nm, when the tip is sufficiently far away from the sample surface ($x_0 > 200$ nm), there is absence of tip-sample interaction. Note that in the absence of tip-sample interaction ($x_0 > 200$ nm), the third harmonic amplitude response is not observed since the 1:3 resonance cannot be activated and no nonlinear energy transfer from the fundamental harmonic (at the driving frequency) and the third harmonic can be realized. However, when $x_0 < 200$ nm and tip-sample interaction exists, it activates the 1:3 internal resonance and the amplitude of the third harmonic of the tip response of the inner paddle emerges; this amplitude gradually increases as the tip-sample distance decreases, indicating that the nonlinearity in the system is stronger, and, in turn, more vigorous nonlinear energy transfer from the fundamental mode to the third harmonic (the second mode) takes place. This means that the third harmonic amplitude is sensitive to the change of tip-sample interaction and, thus, can be utilized to measure it.

In the phase plots of Fig. 5.8 another interesting trend appears. In particular, a transition of the phase starts to occur as the tip-sample interaction begins to affect the dynamics of the system (as can be deduced from the corresponding amplitude plots). Moreover, the discontinuity of the phase plot near the initiation point of the tip-sample interaction becomes clearly visible. The phase transits to higher values in the vicinity of this initiation point, and males sadden transitions (‘jumps’) to lower values as the initial clearance becomes much smaller. Considering that the phase transition arises from the shift

in the resonance frequency due to the nonlinearity in the tip-sample interaction (R. Garcia, 2010), one can surmise that this phase discontinuity arises from the sudden change of the direction of the force acting on the tip, from attractive to repulsive, as discussed previously.

Hence, the transition of the phase to higher values is due to the dominance of the attractive force, whereas the opposite holds by the repulsive force. In other words, the former is strongly influenced by van der Waals interactions, whereas the latter by the elastic deformation of the tip when in contact with the sample surface. It is also noteworthy that the regions where these phase discontinuities occur expand as the effective Young's modulus decreases, as deduced by comparing Figs. 5.8a, b and c. Since the repulsive force from the elastic deformation of the specimen decreases as the surface of the sample softens (corresponding to a decrease in E*), changing the direction of the force from attraction to repulsion would require deeper penetration of the tip in the surface, and smaller values of the initial clearance x_0.

Similar numerical simulations were performed for 1:5 internal resonance by applying Eq. (5-13) to Eq. (5-4), with the other parameters fixed as in the aforementioned analysis on 1:3 internal resonance. The overall frequency response is plotted in Fig. 5.9. Instead of occurring at $\Omega = 3$ as in Fig. 5.6, in this case the amplified higher harmonic emerges at $\Omega = 5$ since a 1:5 internal resonance is now in effect. In Fig. 5.10, the amplitudes and phase transitions at $\Omega = 1$ and $\Omega = 5$ for variation of the initial displacement x_0 are plotted. The trends of the transitions resemble the analogous trends for 1:3 internal resonance (Fig. 5.7); however, in this case the rates of change of the amplitude

and the phase exhibit small deviations, calling for a direct comparison between the cases of 1:3 and 1:5 internal resonance.

In Fig. 5.11a, the amplitude transition as function of the tip-sample distance at E*=1 GPa is plotted for three different cases: (i) The microcantilever without an attached nanomembrane (x_1 for both $\Omega=3$ and 5), (ii) with attached nanomembrane and 1:3 internal resonance (x_2 at $\Omega=3$), and (iii) with attached nanomembrane and 1:5 internal resonance (x_2 at $\Omega=5$). By comparing the responses without and with internal resonance, we deduce that the amplitudes at the higher harmonics are amplified by approximately one order of the magnitude in the presence of the internal resonance. In the operation of the amplitude-modulated AFM (AM-AFM), the higher harmonic signal components are always enhanced due to the nonlinear tip-sample interaction. Considering that in typical AFM cantilevers higher harmonic terms are usually on the order of the noise level (so they are difficult to utilize in order to provide reliable information), the one order enhancement of the higher-harmonic magnitude through the internal resonance amplification is significantly meaningful for realizing the methodology of multi-frequency nonlinear AM-AFM.

Perhaps even more important, a similar comparison is performed for the phase transition with respect to the tip-sample distance at E*=1 GPa, as depicted in Fig. 5.11b. In this plot, two cases are considered, namely the response x_2 for the systems with (i) 1:3 internal resonance implemented at $\Omega = 1$ and $\Omega = 3$, and (ii) with 1:5 internal resonance at $\Omega = 1$ and $\Omega = 5$. We observe that the phase varies more drastically for the higher harmonic when the internal resonance is implemented. Since a small perturbation of the

initial clearance x_0 near the set-point is related to the change in the tip-sample interaction force (from attractive to repulsive, as discussed previously), and, accordingly, the material property of the specimen, the absolute rate of the phase change in this localized region is of great concern, since it determines the force sensitivity. The comparisons show that the amplified phase transitions of the higher harmonics can be utilized for enhanced sensitivity of practical AM-AFM operations. This will further discussed in the following sections.

5.4.3. AMPLITUDE AND PHASE TRANSITIONS

To validate the theoretical predictions from the previous simulations, measurements on amplitude and phase transitions for variations of the initial static clearance were performed for one of the fabricated microcantilevers integrated with an inner paddle and designed for 1:3 internal resonance. The selected microcantilever exhibited its two leading modes at 121.8 kHz and 365.3 kHz, thus possessing the frequency ratio of 1:2.999 which is very close to the ideal case of 1:3 internal resonance. The selected microcantilever was mounted on a conventional AFM system (model MFP-3D AFM, Asylum Research), through which the mounted system was controlled and response acquisition was performed at the tip of the inner paddle. For the target specimen, a silicon surface with grating, typically utilized for the initial calibration of the microcantilever, was employed. The system was driven at its first linearized eigenfrequency ($\Omega_d = 1$), and the resulting signal was processed through the embedded lock-in amplifier to extract the amplitude and phase information at the fundamental and third harmonic frequencies, Ω_d and $3\Omega_d$. The initial clearance, namely the

distance between the tip of the microcantilever and the surface specimen, was controlled gradually for the tip first to approach to the surface and then to retreat from the surface.

Fig. 5.12 depicts the experimental results for the amplitude and the phase at frequencies Ω_d and $3\Omega_d$ under the variation of the initial clearance. In each plot presented therein a new parameter, Δx_0, is introduced on the horizontal axis, indicating the relative displacement from the point where the tip-sample interaction is initiated; thus a positive value of Δx_0 corresponds to the tip approaching towards the surface, whereas a negative value of Δx_0 indicates the reverse. The red and blue lines in each plot of Fig. 5.12 indicate the responses measured for approaching and retreating scenarios, respectively. One can observe that in each plot these two lines are in considerably good match, thus validating the reliability of the experimental measurements and results.

In Fig. 5.12a and b, the amplitude transitions of the harmonics at Ω_d and $3\Omega_d$ are shown, respectively. As predicted from the numerical simulations, the amplitude at Ω_d decreases as the tip approaches the surface (*i.e.*, for positive increments of Δx_0), while the amplitude at $3\Omega_d$ exhibits a gradual increase. Notably, the observed amplitude at $3\Omega_d$ is far above the noise level, thus implying that it is now an utilizable signal component, unlike the case of a typical microcantilever without incorporating internal resonance.

The corresponding phase results shown in Fig. 5.12c and d also follow the theoretical predictions of the previous simulations, as one can observe the transition from the attractive to the repulsive region with decreasing tip-sample separation. Additionally, the comparison between the phases of the different harmonic components indicates that the

rate of change of the phase for variation of the static tip-sample separation is greater for the 3rd harmonic $3\Omega_d$ compared to the 1st harmonic Ω_d, thus validating the theoretical prediction concerning the magnification of the phase transition predicted previously from the numerical simulations.

5.4.4. NONLINEAR AFM OPERATION WITH INHOMOGENEOUS SPECIMEN

Based on the results of Sections 5.4.3 and 5.4.4, the new features of the fabricated microcantilever incorporating 1:3 internal resonance can be summarized as follows: (i) The amplitude of the harmonic component at $3\Omega_d$ (*i.e.*, three times the driving frequency) is above the noise level, and, hence, available for measurement and post-processing; and (ii) the phase transition at $3\Omega_d$, during the tip-sample nonlinear interaction is magnified. To qualitatively assess the importance of these new features for practical AM-AFM operation, the fabricated microcantilever incorporating 1:3 internal resonance was tested to generate the images of a specimen. Considering that the response at higher harmonics may contain more information on the tip-sample interaction, and, accordingly, on the compositional property at the sampling point due to the reduced sampling time, AFM measurements were conducted on an inhomogeneous specimen. In this manner, the discretized regions observed based on the higher harmonic response (and not readily observable based on the lower harmonic response) in the image should prove its capability for enhancement of AFM operation, and its capacity to better identify differences in material properties of the specimen compared to current AFM performance.

The inhomogeneous specimen consisted of randomly distributed polystyrene (PS) nanoparticles with diameters of ~200 nm on polydimethylsiloxane (PDMS) substrate, prepared by the drop casting method (Dol *et al.*, 2001). At first, 4 different concentrations (2%, 0.2%, 0.02%, and 0.002%) of nanoparticle samples were prepared by 10-fold serial dilution from original 2% solution. A 5 μL droplet of each solution was then applied onto the glass slide and dried in room temperature to remove all solutions. In the next step, PDMS (Sylgard 184, Corning) was prepared by mixing hexane to a weight ratio of PDMS (at ratios of curing agent / base / hexane of 1:10:1000). The mixture was spin-coated at 5000 rpm onto the glass slide for 2 minutes to obtain ultra-thin PDMS film (Thangawng *et al.*, 2007). Finally, the PDMS films with nanoparticle-coated glass slides were cured on a hot plate at 150 º C for 10 minutes.

Figure 5.13 summarizes the measurements conducted with a set point (initial clearance) of 0.8, where the attraction force is dominant. The 'set point' is one of the control parameters in tapping mode AFM operation. It is expressed as a nominal oscillation amplitude normalized by a free (disengaged) oscillation amplitude, which is maintained constant during the AFM measurement by feedback control. Hence, the set point value controls the magnitude of the force that the tip exerts to the surface of the sample, *e.g.*, the lower set point value is, the stronger is the impact force exerted to the sample.

In the topography image (*cf.* Fig. 5.13a), one can notice that there clearly exist three nanoparticles closely packed in the center, yet their borders are not clearly distinguishable. The image taken by the third harmonic amplitude ($3\Omega_d$) in Fig. 5.13b provides enhanced results in terms of a better discrimination for the boundaries of the nanoparticles; indeed,

the boundary of the upper nanoparticle is visualized as it clearly contrasts with the other two lower particles. The plots of Figs. 5.13c,d depict the corresponding images constructed based on phase information at $1\Omega_d$ and $3\Omega_d$, which are known to be sensitive to compositional variations related to energy dissipation on heterogeneous surfaces. Even though the different composition between the nanoparticles and the PDMS thin film gives clear recognition of the nanoparticles in both phase images qualitatively, the third harmonic phase quantitatively provides almost three times better sensitivity.

In Fig. 5.14, the same area is imaged with a lower set point of 0.5, where the repulsive force is dominant. Considering that the repulsive force is generated by the elastic deformation when the tip is in contact with the surface of the specimen, the specimen's elastic compliance is undoubtfully one of the main contributors to the interaction force. Comparing the results of the different force regimes, the most noticeable change is found in the images based on the phase information, especially, based on the phase at $3\Omega_d$, where high contrast between the upper and the lower nanoparticles is noticed (*cf.* Fig. 5.14d). It is noteworthy that this contrast also exists in the image based on the phase at $1\Omega_d$ (*cf.* Fig. 5.14c) but is less distinguishable as the darker region does not form a clear perimeter for the nanoparticle. The main source for this contrast can be attributed to the difference in the material composition of each nanoparticle. Because of the nature of the processes utilized for the sample preparation, some of the nanoparticles may be exposed to the PDMS substrate, whereas others may be embedded and/or covered by PDMS. Regarding that the Young's modulus of PS (3000~3600 MPa) is significantly larger than that of PDMS

(360~870 kPa), the images based on phase information are more capable in discriminating between any PDMS-covered nanoparticles and bare nanoparticles.

To conduct a qualitative comparison on the sensitivity for each of the considered cases, the cross-section of the images of Fig. 5.14 were generated along the indicated dissection line, as depicted in Fig. 5.15. In the topography image (*cf.* Fig. 5.15a), the height for each nanoparticle is measured to be close in value. The image based on the third harmonic amplitude $3\Omega_d$ (*cf.* Fig. 5.15b) on the other hand, exhibits a large discrepancy in the corresponding amplitude of each nanoparticle; it can be deduced, therefore, that the tip-sample interaction is affected by the measurement position, although similar topography information is generated. This implies that the amplitude at $3\Omega_d$ may contain information on the composition of the specimen. The plots depicted in Figs. 5.15c and 5.15d present the acquired phases at $1\Omega_d$ at $3\Omega_d$, respectively. The range of the phase variation at $3\Omega_d$ is measured to be approximately 30°, whereas the corresponding measurement for $1\Omega_d$ is 8°. The enhanced sensitivity of the phase of the third harmonic, leading to four times magnification of the range of phase variation in this case, evidently validates the previous theoretical prediction and highlights the importance of phase information in the proposed new AFM design.

5.5 Conclusions

In the third application of constructive utilization of intentional nonlinearity in micro/nanoresonator design, we proposed a new high-frequency AFM concept. The new

design was based on structural modification of a typical AFM microcantilever in order to incorporate an internal resonance between its leading modes. In the particular application studied in this Chapter the AFM system was designed to possess an inherent *1:n* internal resonance, in order to amplify the signal at the *n*-th harmonic of the response of an inner paddle in the form of an attached nanomembrane. The overall aim of the work was to generate compositional mapping measurements with enhanced spatial resolutions based on higher-harmonic amplitude and phase information.

The attached nanomembrane, implemented as an inner paddle rigidly connected to the base AFM microcantilever, served as a structure that could be controlled to adjust the eigenfrequency ratio to *1:n*; this was a necessary (but not sufficient) condition for implementation of the *1:n* internal resonance in the system. Then, activation of this internal resonance was achieved by the nonlinear tip-sample interactions that occurred during the AFM operation. In turn, the internal resonance led to nonlinear energy transfer from the lower-frequency harmonic (corresponding to the fundamental bending mode of the system) that was directly excited by the driving frequency, to the *n*-th higher harmonic (corresponding to the second bending mode), leading to amplification of that harmonic.

The analytical reduced-order model presented in this study was proven to be a good theoretical tool for determining the dimensions and material parameters of the nanomembrane for realizing the internal resonance, since the experimentally measured eigenfrequencies of the integrated microcantilever – nanomembrane system showed good match with the analytical predictions. It is noteworthy that the transfer-printing technique enhanced the accuracy of the model as the thickness between the base microcantilever and

the inner paddle showed a large discrepancy, avoiding any unwanted coupling effects between modes, and thus enabling the construction of the reduced-order, lower dimensional model.

The theoretical simulations and the experimental results validate the proposed concept of nonlinear AFM based on internal resonance, since the targeted amplification of the higher harmonic was clearly achieved. The results indicate that enhanced sensitivity and AFM performance can be expected from the proposed design. In particular, as long as the oscillation amplitude of the higher harmonic is amplified above a certain noise level, this signal can be effectively measured to generate not only amplitude information, but also phase information based on the higher harmonic component. The sensitivity enhancement was well proved by comparing the images based on phase information taken for a heterogeneous material in the region where the repulsive force in the tip-sample interaction was dominant, expressed as high contrast imaging between exposed and the covered nanoparticles of the tested sample. Based on this result, we expect that the proposed microcantilever design will be able to measure subsurface composition by interacting with the underlying surface and performing non-destructive measurement simultaneously.

Although this new design has proven to generate improved images compared to conventional AFM operation, it is not yet well understood how the composition of the surface is correlated to the extracted amplitude and the phase information. Additionally, the influence of the excitation of a certain harmonic component (other than $3\Omega_d$ and $5\Omega_d$) is not yet fully disclosed. This calls for future study of the variations of the measured harmonics caused by the tip-sample interaction, in order to develop suitable analytical

models capable of predicting the effects of the material property of the specimen on the amplitude and the phase transitions of the acquired harmonics of interest.

FIGURES

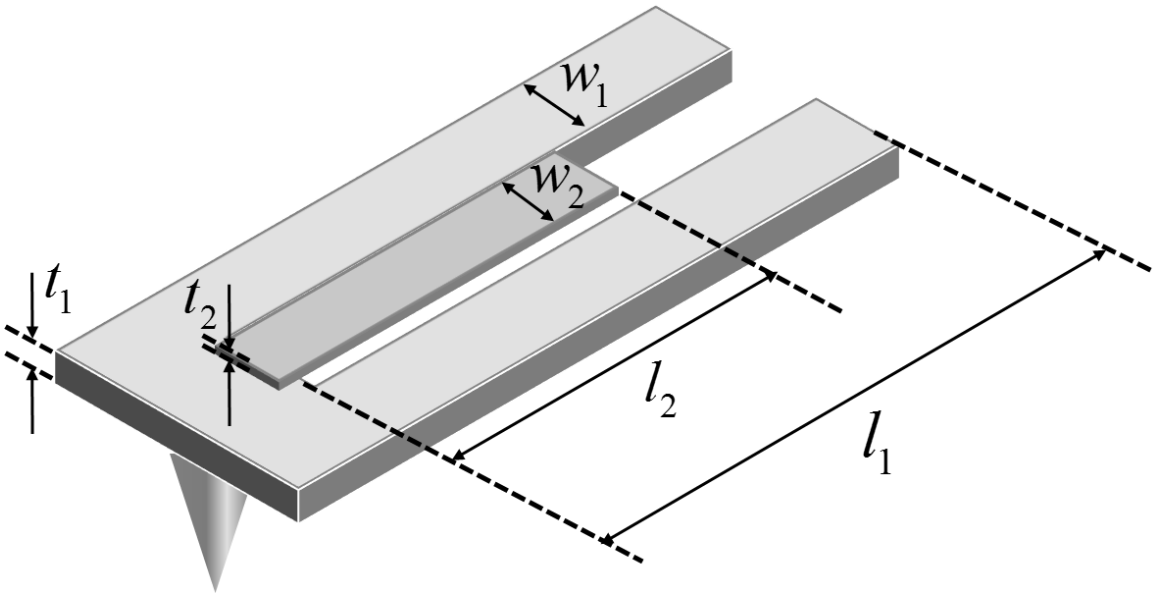

Figure 5.1. Schematic view of the proposed AFM microcantilever with inner paddle, incorporating internal resonance.

.

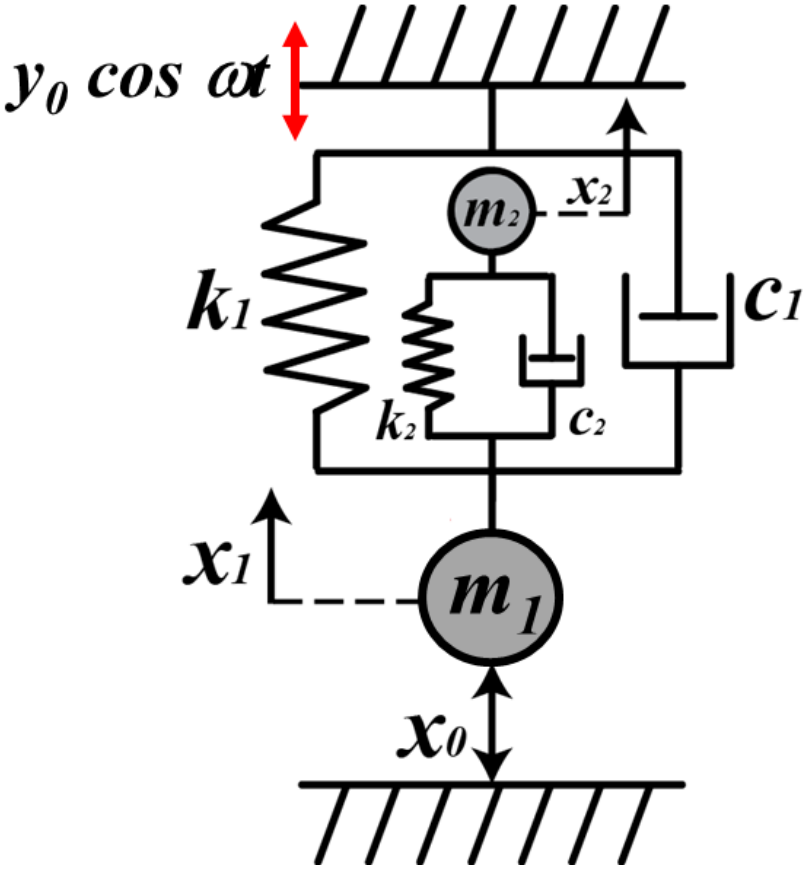

Figure 5.2. Lumped-parameter model of the microcantilever with an attached inner paddle under the simplifying assumption that in the frequency range of interest both components oscillate in their fundamental cantilever bending modes.

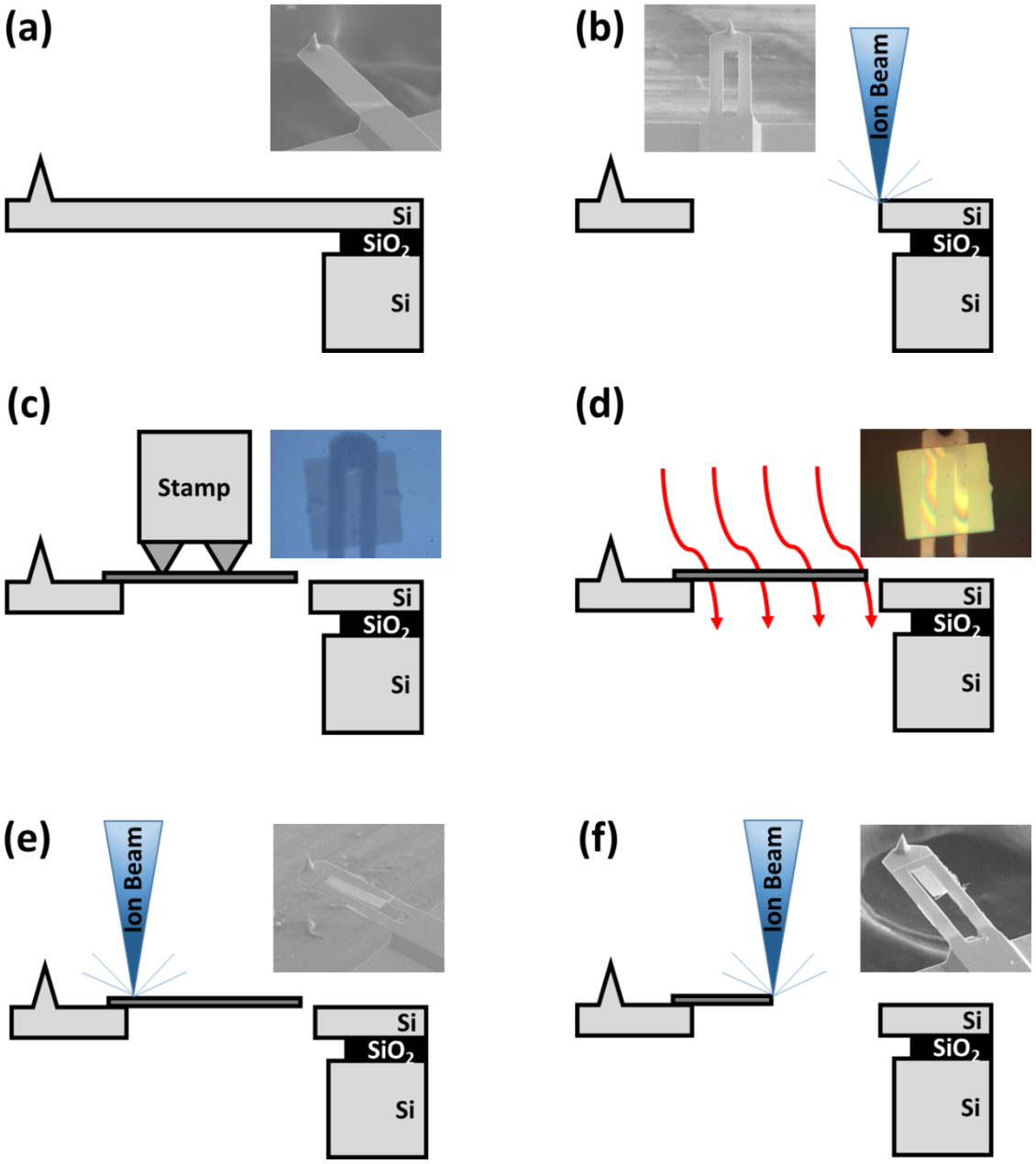

Figure 5.3. Fabrication process for the proposed AFM system incorporating internal resonance: (a) Base microcantilever, (b) ion-milling process to form the cavity, (c) transferring silicon-ink onto the structure, (d) annealing to form the silicon fusion boding, (e) ion-milling to form the paddle, and (f) gradually adjusting the length of the inner paddle to introduce the desired *1:n* eigenfrequency ratio between the two leading modes of the integrated system; each of the optical/SEM images in the insets provides a representative view of the fabricated system after completion of each of these processes.

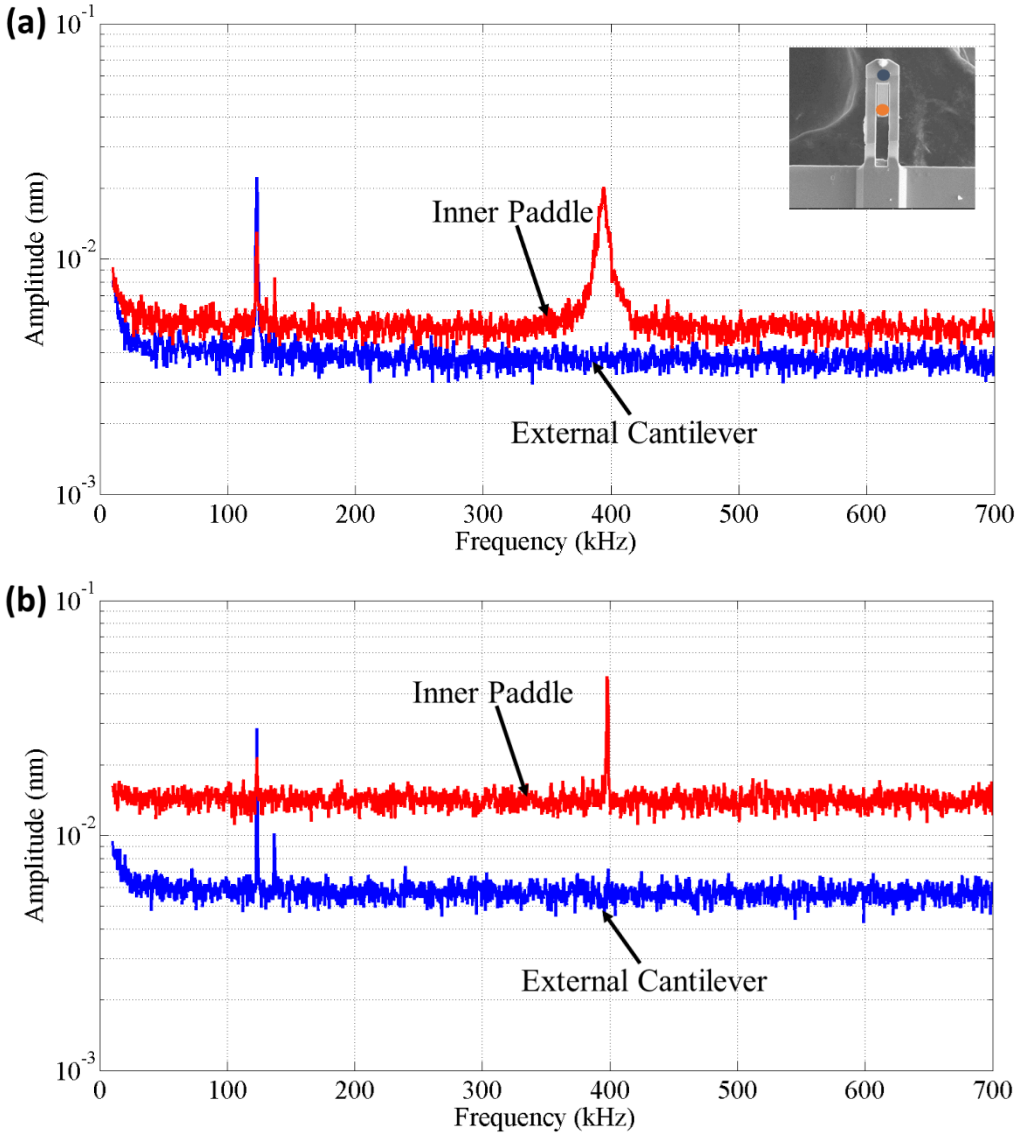

Figure 5.4. Frequency spectra of thermal noise signals measured for the finalized cantilever incorporating an 1:3.2 eigenfrequency ratio between its leading bending modes at (a) ambient environment (750 Torr), and (b) high vacuum environment (8 mTorr), with the red line indicating the response of the inner paddle (nanomembrane), and the blue line the response of the base microcantilever; the inset in (a) depicts the measurement points (sensing positions) on the two components of the system.

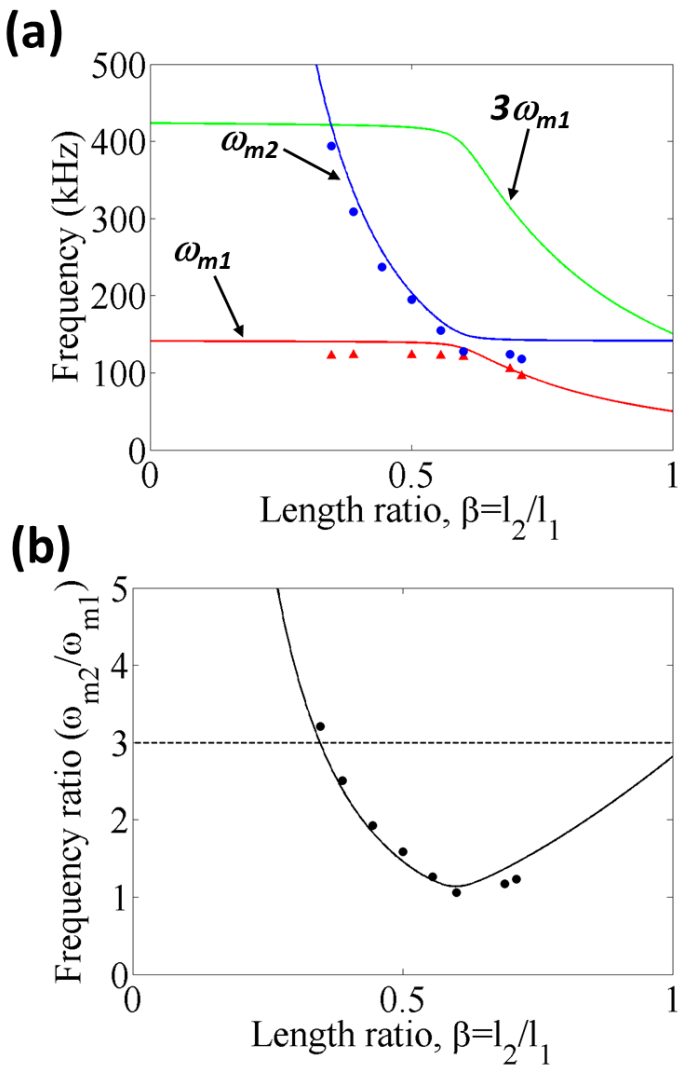

Figure 5.5. Linearized eigenfrequencies predicted by the analytical model (Eq. 5-8) for varying length ratio between the inner paddle and the external cantilever: (a) Eigenfrequencies in Hz, with red and blue lines indicating the first (in-phase) and second (out-of-phase) modes of the system, respectively; the red and blue markers denote experimentally measured eigenfrequencies, whereas the green line results from the multiplication of the first eigenfrequency by 3 times, and its intersection with the blue line corresponds to the aimed point for realizing 1:3 internal resonance; (b) analytically predicted eigenfrequency ratio (black line), as compared to experimentally measured values (black markers) obtained by thermal noise measurements (*cf.* Fig. 5.4).

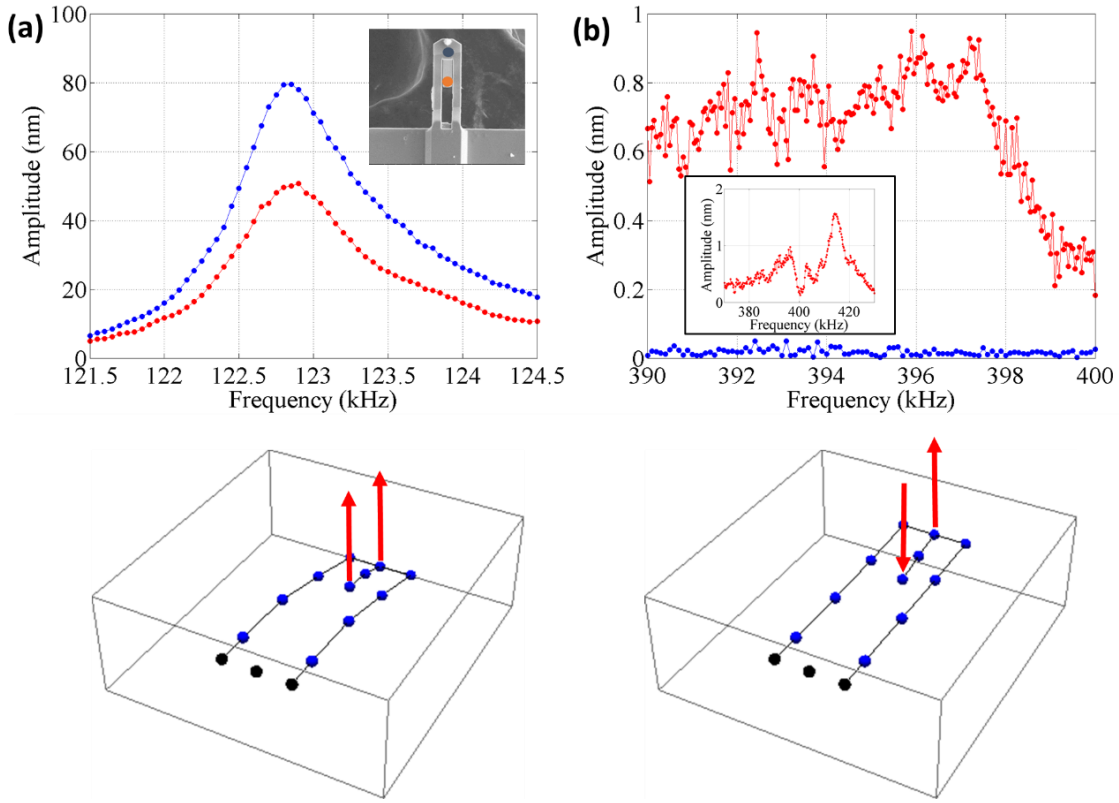

Figure 5.6. Resonance response of the microcantilever with 1:3.2 frequency ratio obtained by frequency sweep at a range in the neighborhood of (a) its first mode and (b) its second mode, when the microcantilever was driven by base harmonic excitation at constant AC voltage of 1 V in ambient environment (750 Torr); the red and blue lines indicate the responses of the tip of the inner paddle and the tip of the microcantilever, respectively, whereas the inset in (a) depicts the points of the measurement; the inset in (b) shows the forced response of the inner paddle in an extended frequency range, whereas lower figures in (a) and (b) depict the corresponding mode shapes at the peak (resonance) frequencies (122.85 kHz and 397.4 kHz), constructed by the experimentally measured amplitudes and phases of selected points on the microcantilever and the paddle. The effective modal stiffness has been estimated as 1.04 N/m for the 1st mode and 0.385 N/m for the 2nd mode, based on the assumption that the effective modal mass is m_e (as the mass of the paddle is negligible compared to the outer cantilever in the 1st mode) and $\alpha\beta\gamma\, m_e$ (as the outer cantilever remains nearly stationary in the 2nd mode) for each respective mode.

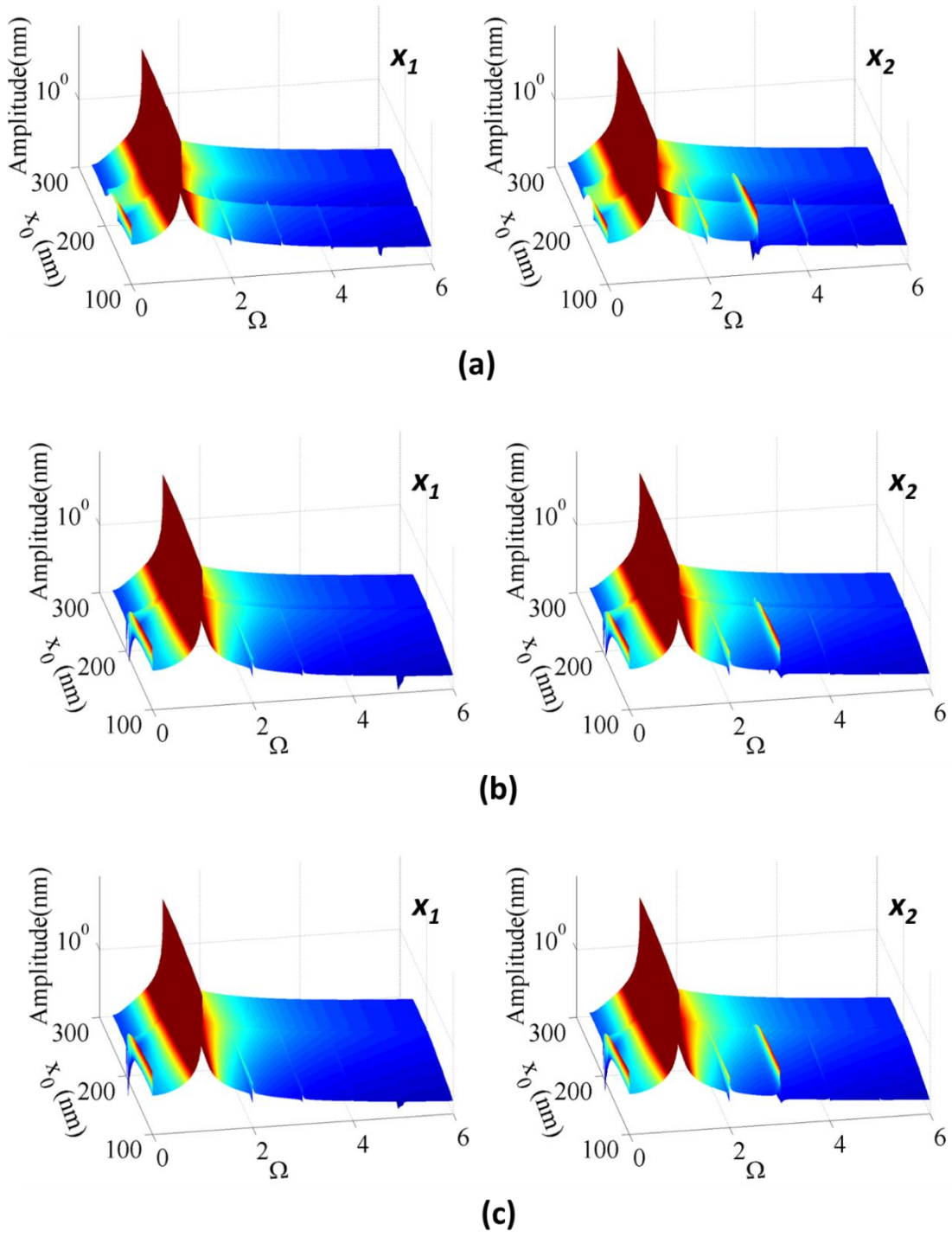

Figure 5.7. Frequency spectra of the theoretical model with 1:3 internal resonance (Eq. 5-12), when (a) E*=0.1 GPa, (b) E*=1.0 GPa and (c) E*=10.0 GPa; the left and right columns show the responses of the base microcantilever and inner paddle, respectively.

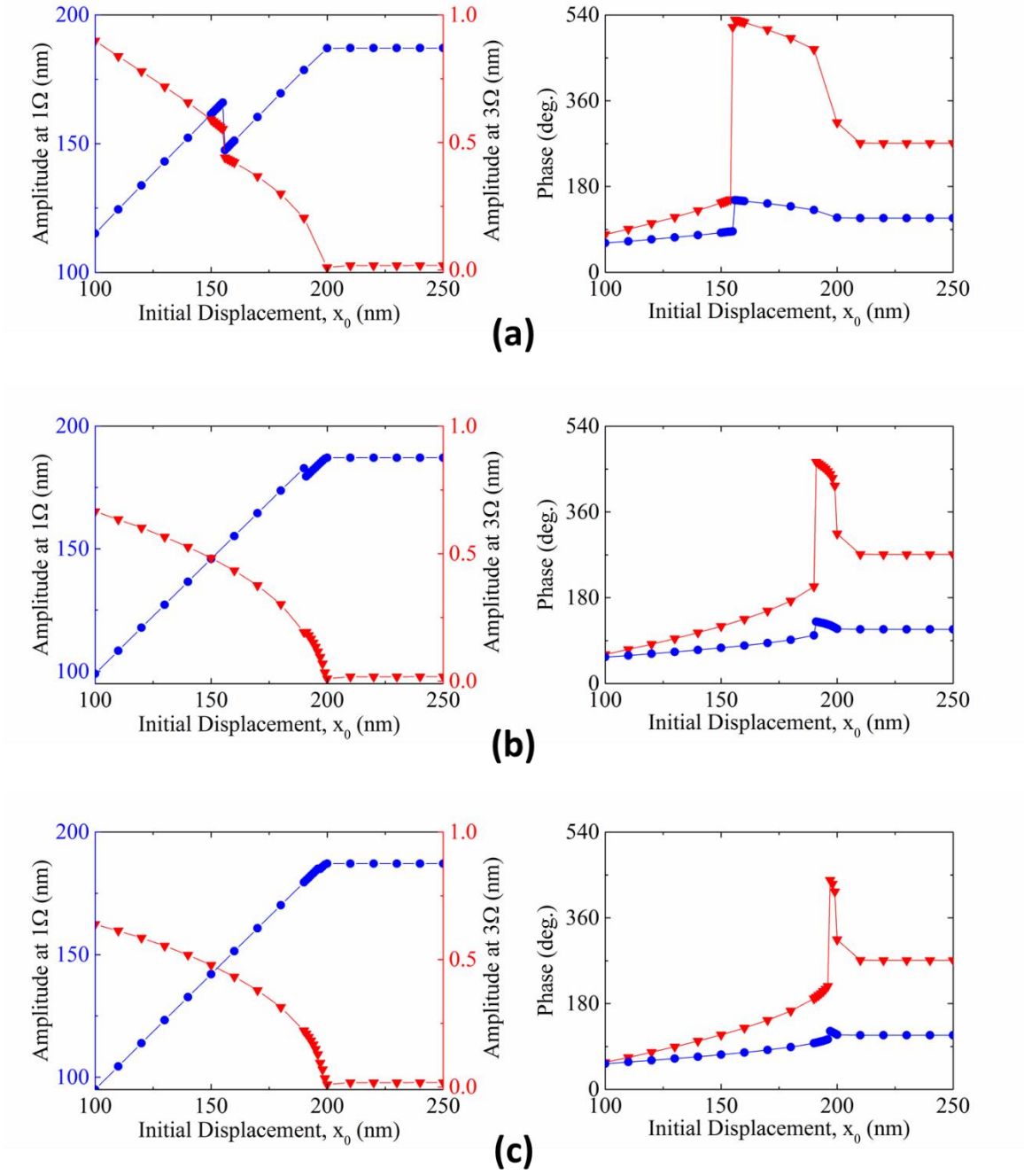

Figure 5.8. Amplitude (left column) and phase (right column) transitions of the theoretical model with 1:3 internal resonance for varying initial clearance x_0, when (a) E*=0.1 GPa, (b) E*=1.0 GPa and (c) E*=10.0 GPa; the blue and the red lines indicate the responses of the harmonics at $1\Omega_d$ (driving frequency) and $3\Omega_d$, respectively.

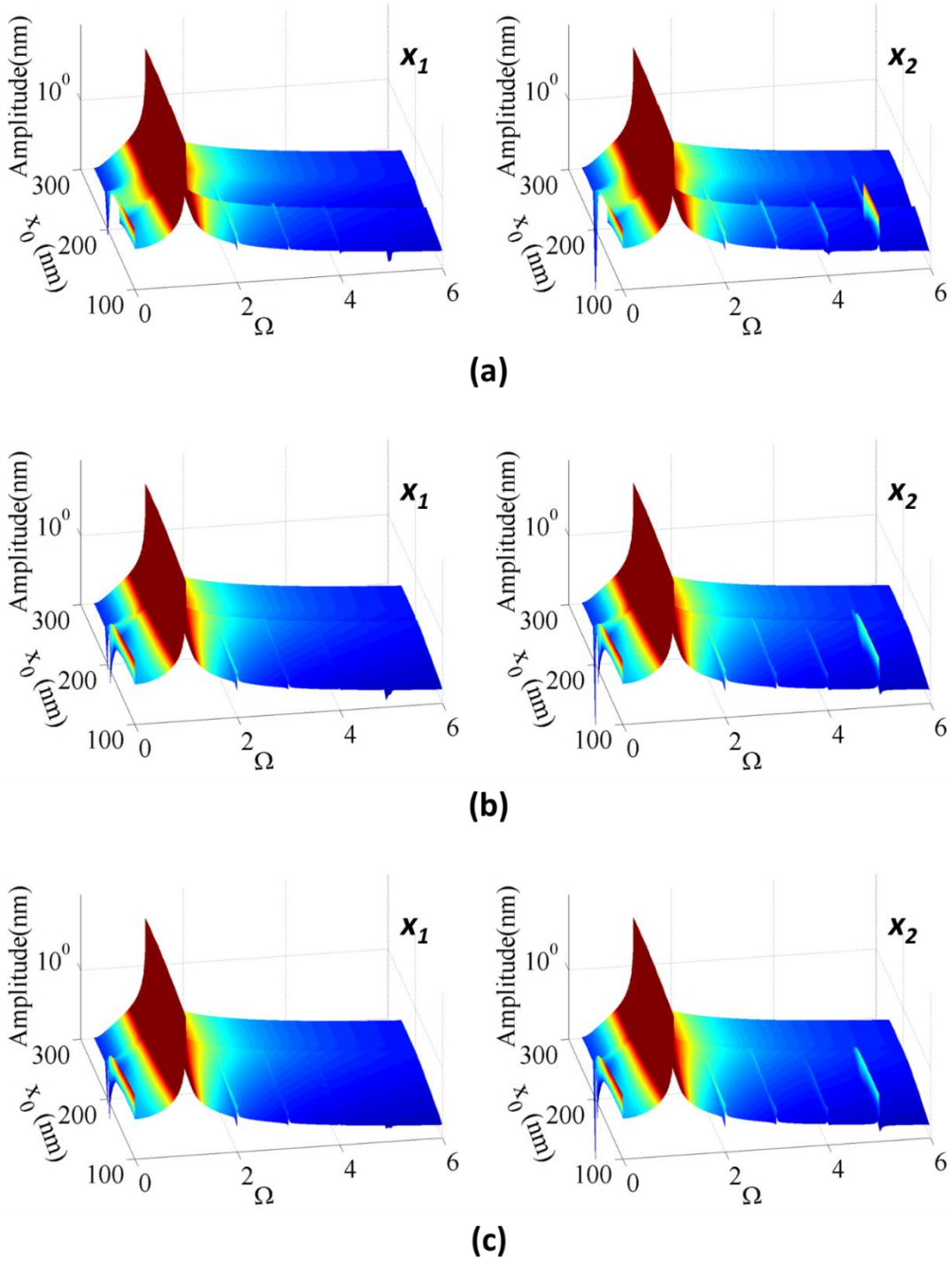

Figure 5.9. Frequency spectra of the theoretical model with 1:5 internal resonance (Eq. 5-13), when (a) E*=0.1 GPa, (b) E*=1.0 GPa and (c) E*=10.0 GPa; the left and right columns show the responses of the base microcantilever and inner paddle, respectively.

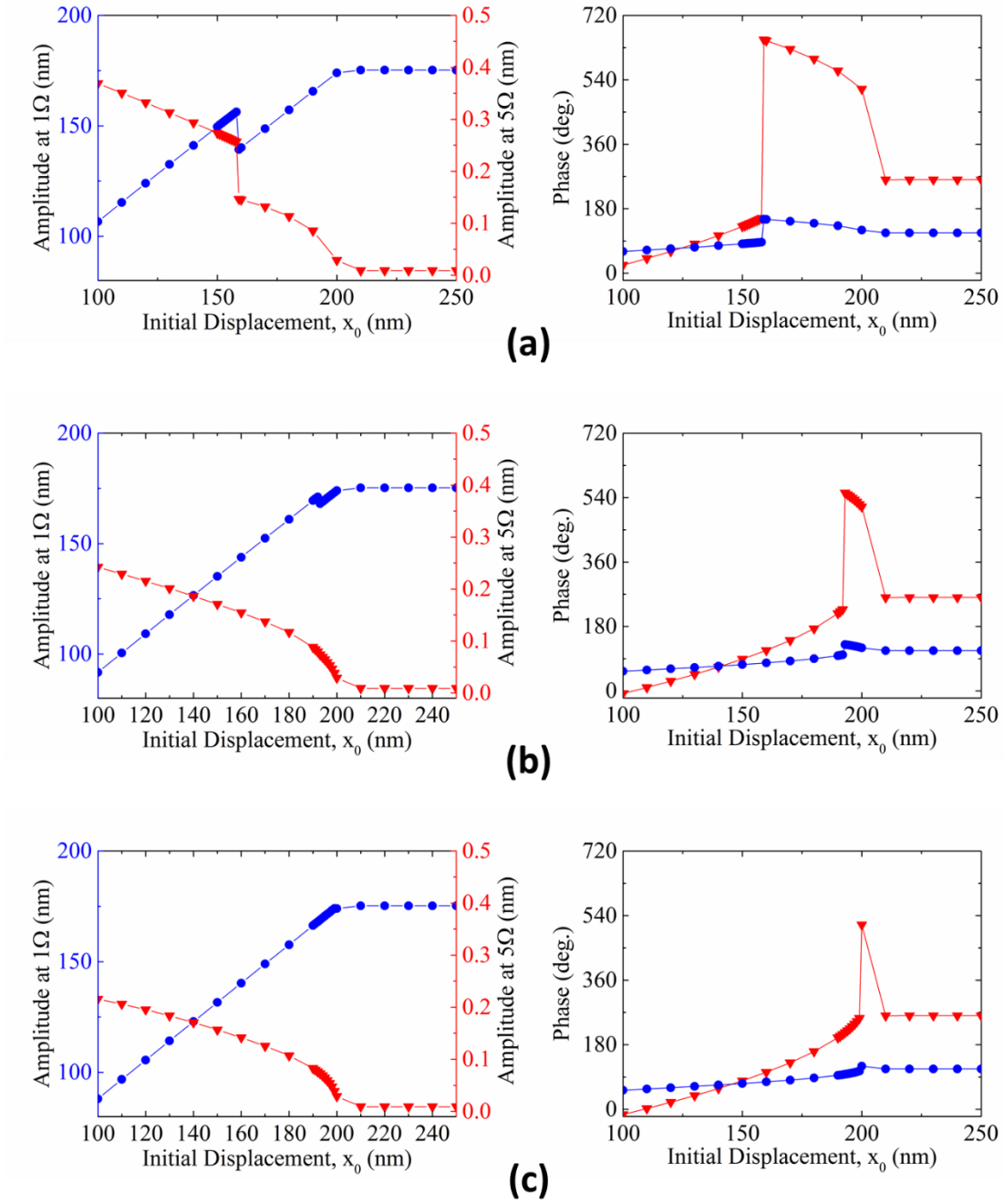

Figure 5.10. Amplitude (left column) and phase (right column) transitions of the theoretical model with 1:5 internal resonance for varying initial clearance x_0, when (a) E*=0.1 GPa, (b) E*=1.0 GPa and (c) E*=10.0 GPa; the blue and the red lines indicate the responses of the harmonics at $1\Omega_d$ (driving frequency) and $5\Omega_d$, respectively.

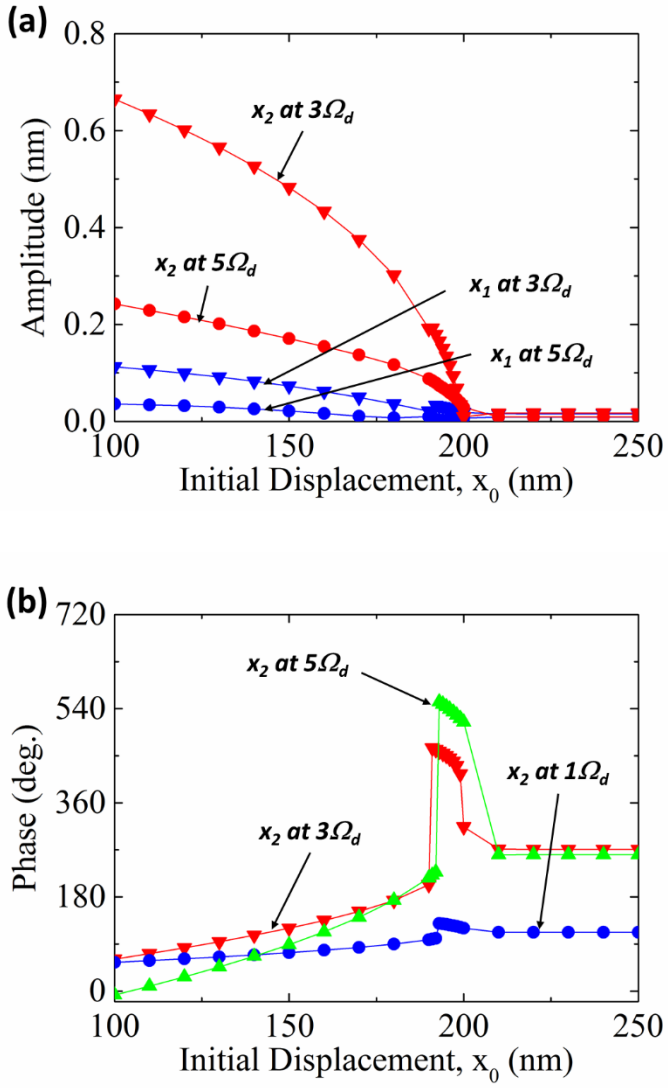

Figure 5.11. Comparisons of the sensitivities of the responses of microcantilevers for variation of the initial clearance x_0, as predicted by the theoretical model: (a) Amplitude of the steady state response of the inner paddle at $3\Omega_d$ for the system with 1:3 internal resonance and at $5\Omega_d$ for the system with 1:5 internal resonance (red lines), and of the microcantilever with (blue line); (b) phase of the steady state response of the inner paddle at $3\Omega_d$ for the system with 1:3 internal resonance (red line), at $5\Omega_d$ for the system with 1:5 internal resonance (green line), and at $1\Omega_d$ for either 1:3 or 1:5 resonance.

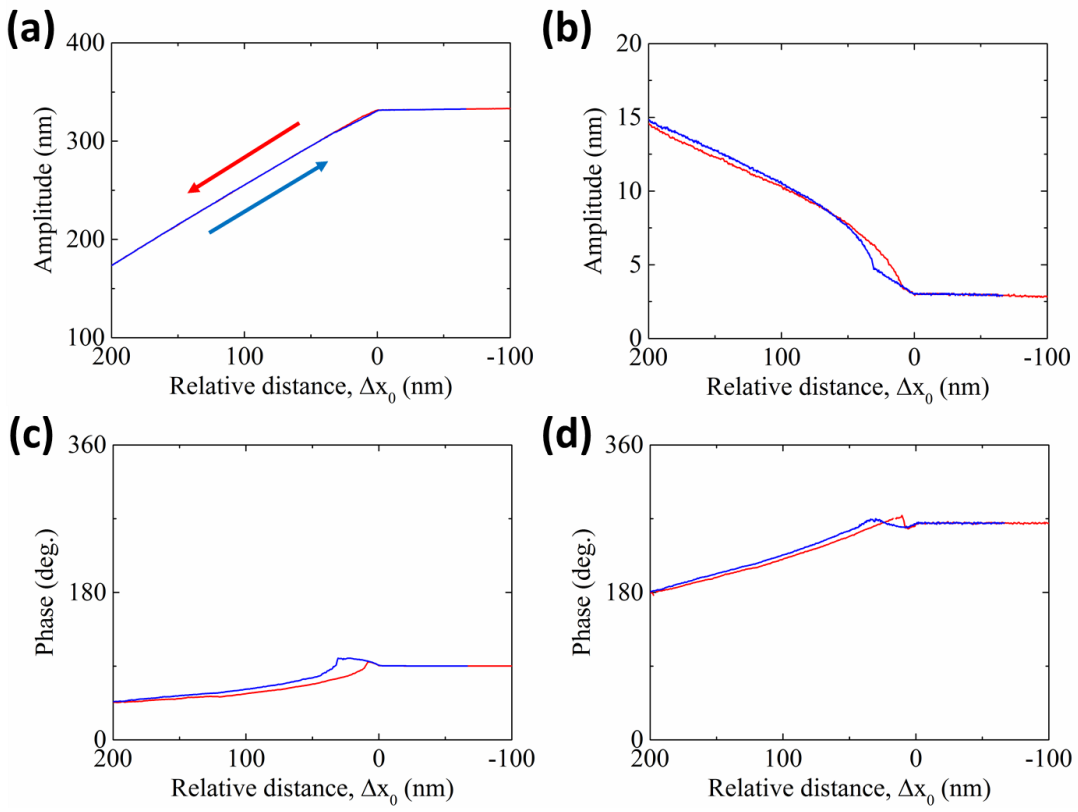

Figure 5.12. Experimental sensitivity curves for the paddle response of a system with an 1:2.999 eigenfrequency ratio, and driven at Ω_d =122.0 kHz: (a) Amplitude of the harmonic at $1\Omega_d$, (b) amplitude of the harmonic at $3\Omega_d$, (c) corresponding phase at $1\Omega_d$, and (d) corresponding phase at $3\Omega_d$; red and the blue line indicate that the measurement was performed as the tip approached to, or retreated from the surface of the sample, respectively.

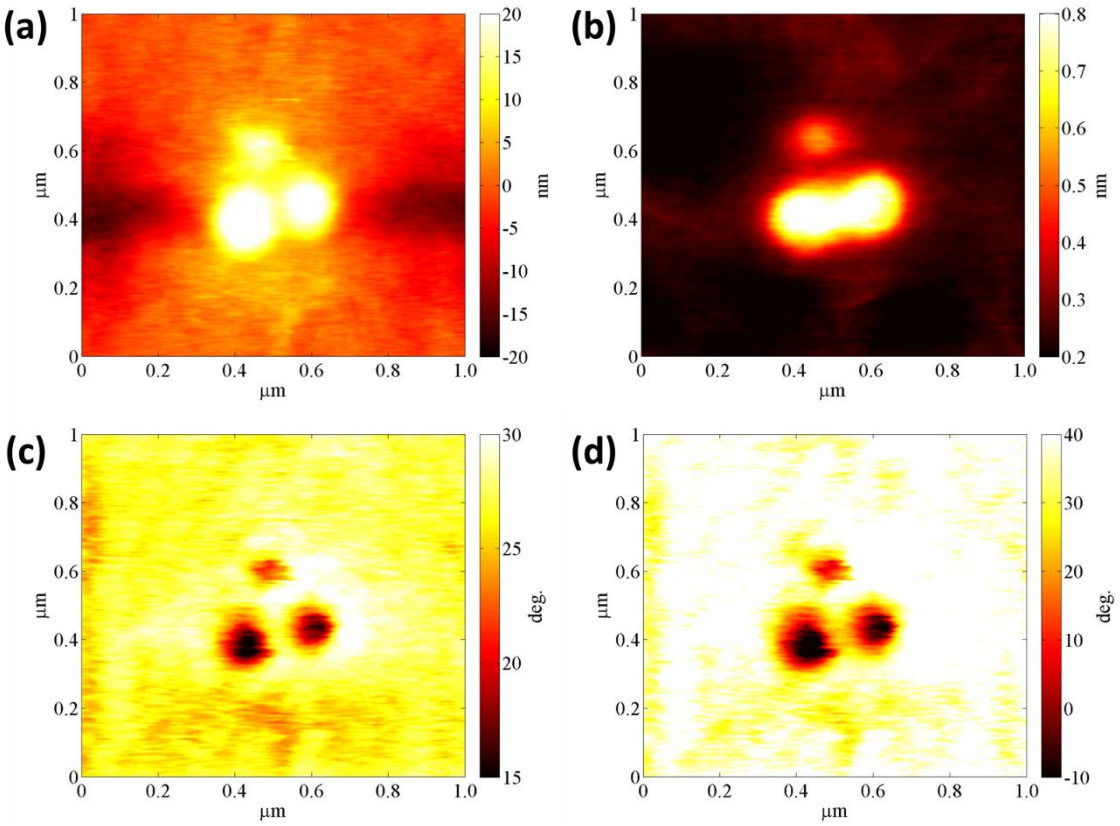

Figure 5.13. AFM images taken of a heterogeneous surface by the proposed microcantilever system with 1:2.95 eigenfrequency ratio (leading modes at 120.0 kHz and 353.8 kHz), depicting (a) the topography of the sample, and the image based on (b) the amplitude of the harmonic at $3\Omega_d$, (c) the phase of the harmonic at $1\Omega_d$ and (d) the phase at the harmonic $3\Omega_d$,; the system was driven at Ω_d =115 kHz with a set point of 0.8.

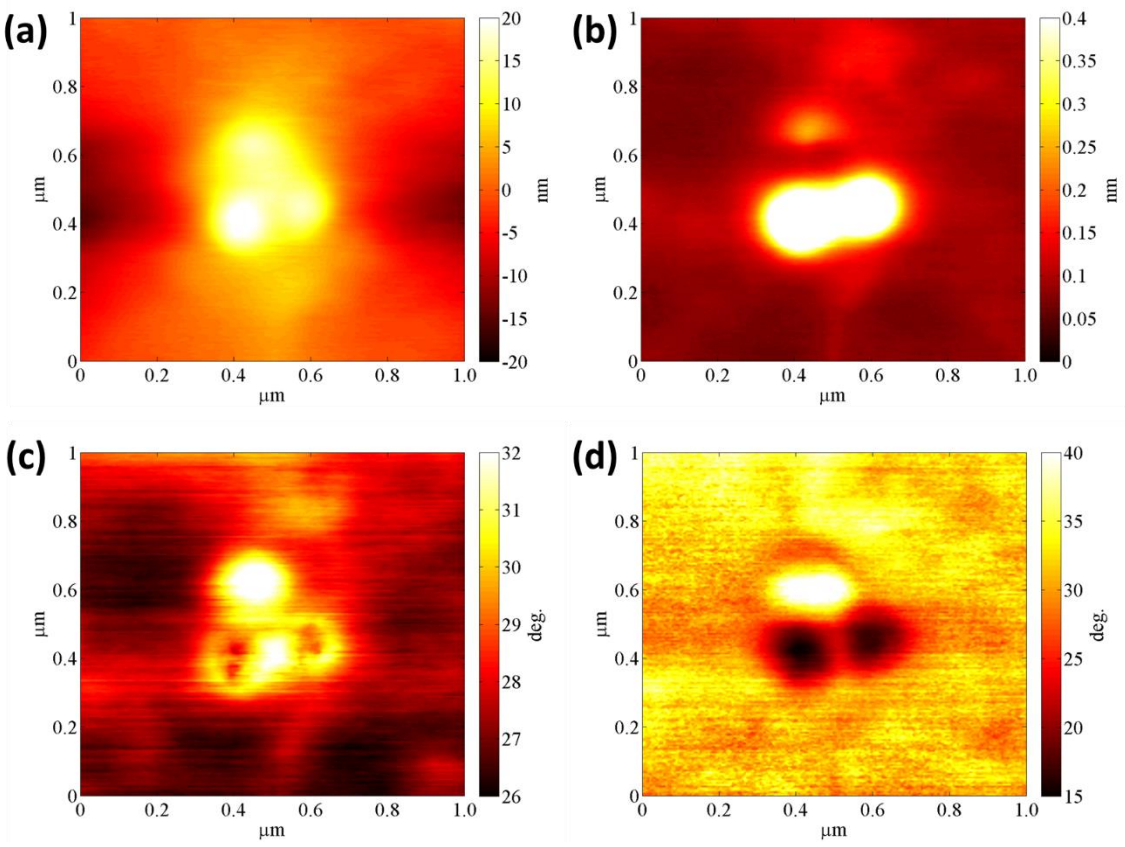

Figure 5.14. AFM images taken of a heterogeneous surface by the proposed microcantilever system with 1:2.95 eigenfrequency ratio (leading modes at 120.0 kHz and 353.8 kHz), depicting (a) the topography of the sample, and the image based on (b) the amplitude of the harmonic at $3\Omega_d$, (c) the phase of the harmonic at $1\Omega_d$ and (d) the phase at the harmonic $3\Omega_d$,; the system was driven at Ω_d =115 kHz with a set point of 0.5 (stronger tip-sample interaction compared to the results of Fig. 5.13).

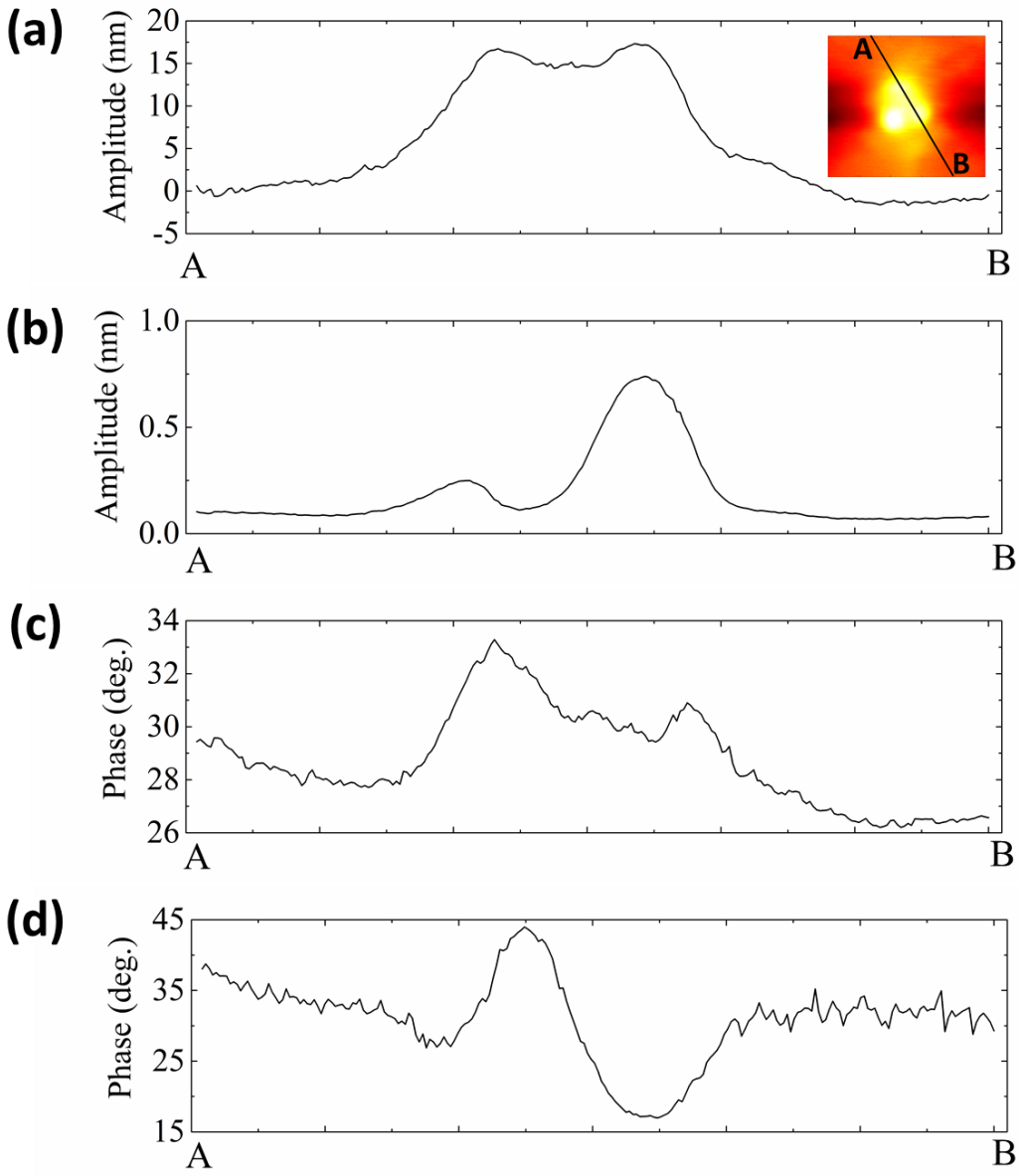

Figure 5.15. Cross-sections of the images depicted in Figure 5.14 along the line A-B shown in the inset, depicting (a) topography, (b) amplitude at $3\Omega_d$, (c) phase at $1\Omega_d$ and (d) phase at $3\Omega_d$.

REFERENCES

Baumann, M., Stark, R. W., Dual Frequency Atomic Force Microscopy on Charged Surfaces, *Ultramicroscopy*, 110, 578-581 (2010).

Binnig, G., Quate, C. F., Atomic Force Microscope, *Phys. Rev. Lett*., 56, 930-933 (1986).

Derjaguin, B., Müller, V., Toporov, Y., On Different Approaches to the Contact Mechanics, *J. Colloid Interface Sc*., 73(1), 293-294 (1980).

Dietz, C., Zerson, M., Riesch, C., Gigler, A. M., Stark, R. W., Rehse, N., Margerle, R., Nanotomography with Enhanced Resolution using Bimodal Atomic Force Microscopy, *Appl. Phys. Lett.*, 92, 143107 (2008).

Dol, G. C., Tsuda, K., Weener, J.-W., Bartels, M. J., Asavei, T., Gensch, T., Hofkens, J., Latterini, L., Schenning, A. P. H. J., Meijer, B. W., Schryver, F. C. D., Merging of Hard Spheres by Phototriggered Micromanipulation, *Angew. Chem. Int. Edit.,* 40 (9), 1710-1714 (2001).

Dong, M., Husale, S., Sahin, O., Determination of Protein Structural Flexibility by Microsecond Force Spectroscopy, *Nat. Nanotech.*, 4, 514-517 (2009).

Ebeling, D., Eslami, B., Solares, S. D. J., Visualizing the Subsurface of Soft Matter: Simultaneous Topographical Imaging, Depth Modulation, and Compositional Mapping with Triple Frequency Atomic Force Microscopy, *ACS Nano*, 11, 10387-10396 (2013).

Fritz, M., Radmacher, M., Cleveland, J. P., Allersma, M. W., Stewart, R. J., Gieselmann, R., Janmey, P., Schmidt, C. F., Hansma, P. K., Imaging Globular and

Filamentous Proteins in Physiological Buffer Solutions with Tapping Mode Atomic Force Microscopy, *Langmuir*, 11, 3529 (1995).

Garcia, R., 2010, *Amplitude Modulated Atomic Force Microscopy, Ch 4: Theory of Amplitude Modulation AFM,* Wiley-VCH.

Hacker, E., Gottieb, O., Internal Resonance Based Sensing in Non-contact Atomic Force Microscopy, *Appl. Phys. Lett.*, 101, 053106 (2012).

Kim, S., Wu, J., Carlson, A., Jin, S. H., Kovalsky, A., Glass, P., Liu, Z., Ahmed, N., Elgan, S.L., Chen, W., Ferreira, P.M., Sitti, M., Huang, Y., Rogers, J.A., Microstructured elastomeric surfaces with reversible adhesion and examples of their use in deterministic assembly by transfer printing, *Proc. Natl. Aca. Sci. U. S. A.*, 107, 17095-17100 (2010).

Lyubchenko, Y. L., Shlyakhtenko, L. S., Visualization of supercoiled DNA with atomic force microscopy in situ., *Proc. Natl. Aca. Sci. U. S. A.*, 94, 496 (1997).

Martin, Y., Williams, C.C., Wickramasinghe, H. K., Atomic Force Microscope: Force Mapping and Profiling on a Sub 100 Angstrom Scale., *J. Appl. Phys.*, 61, 4723 (1987).

Martinez, N. F., Lozano, J. R., Herruzo, E. T., Garcia, F., Richter, C., Sulzbach, T., Garcia, R., Bimodal Atomic Force Microscopy Imaging of Isolated Antibodies in Air and Liquids, *Nanotechnology*, 19, 384011 (2008).

Martinez, N. F., Patil, S., Lozano, J. R., Garcia, R., Enhanced Compositional Sensitivity in Atomic Force Microscopy by the Excitation of the First Two Flexural Modes, *Appl. Phys. Lett*., 89, 153115 (2006).

Martinez-Martin, D., Herruzo, E. T., Dietz, C., Gomez-Herrero, J., Garcia, R., Noninvasive Protein Structural Flexibility Mapping by Bimodal Dynamic Force Microscopy, *Phys. Rev. Lett.*, 106, 198101 (2011).

Müller, V.M., Yushchenko, V.S., Derjaguin, B.V., On the Influence of Molecular Forces on the Deformation of an Elastic Sphere and its Sticking to a Rigid Plane, *J. Colloid Interface Sc.*, 77 (1), 91-101.

Preiner, J., Tang, J., Pastusehnko, V., Hinterdorfer, P., Higher Harmonic Atomic Force Microscopy: Imaging of Biological Membranes in Liquid, *Phys. Rev. Lett.*, 99, 046102 (2007).

Proksch, R., Multifrequency, Repulsive-mode Amplitude-modulated Atomic Force Microscopy, *Appl. Phys. Lett.*, 89, 113121 (2006).

Radmacher, M., Fritz, M., Hansma, H. G., Hansma, P. K., Direct Observation of Enzyme-activity with the Atomic-Force Microscope., *Science*, 265, 1577 (1994).

Rodriguez, T. R., Garcia, R., Compositional Mapping of Surfaces in Atomic Force Microscopy by Excitation of the Second Normal Mode of the Microcantilever, *Appl. Phys. Lett.*, 84, 449-451 (2004).

Sadewasser, S., Villanueva, G., Plaza, J. A., Special Cantilever Geometry for the Access of Higher Oscillation Modes in Atomic Force Microscopy, *Appl. Phys. Lett.*, 89, 033106 (2006).

Sahin, O., Magonov, S., Su, C., Quate, C. F., Solgaard, O., An Atomic Force Microscope Tip Designed to Measure Time-varying Nanomechanical Forces, *Nat. Nanotech.*, 29, 507-514 (2007).

Solares, S. D., Chawla, G., Frequency Response of Higher Cantilever Eigenmodes in Bimodal and Trimodal Tapping Mode Atomic Force Microscopy, *Meas. Sci. Technol.*, 21, 125502 (2010a).

Solares, S. D., Chawla, G., Triple-frequency Intermittent Contact Atomic Force Microscopy Characterization: Simultaneous Topographical, Phase, and Frequency Shift Contrast in Ambient Air, *J. Appl. Phys.*, 108, 054901 (2010b).

Sanders, J. A., Verhulst, F., Murdock, J., *Averaging Methods in Nonlinear Dynamical Systems*, Springer Verlag (2007).

Stark, M., Stark, R. W., Heckl, W. M., Guckenberger, R., Spectroscopy of the nharmonic Cantilever Oscillations in Tapping-mode Atomic-force Microscopy, *Appl. Phys. Lett*., 77, 3293-3295 (2000).

Thangawng, A. L., Ruoff, R. S., Swartz, M.A., Glucksberg M. R., An Ultra-thin PDMS Membrane as a Bio/Micro-nano Interface: Fabrication and Characterization, *Biomed. Microdevices,* 9 (4), 587-595 (2007).

Vakakis, A. F., Gendelman, O., Bergman, L. A., McFarland, D. M., Kerschen, G., Lee, Y. S., *Passive Nonlinear Targeted Energy Transfer in Mechanical and Structural Systems: I and II,* Springer Verlag (2008).

Xu, X., Melcher, J., Basak, S., Reifenberger, R., Raman, A., Compostional Contrast of Biological Materials in Liquids Using the Momentary Excitation of Higher Eigenmodes in Dynamic Atomic Force Microscopy, *Phys. Rev. Lett.*, 102, 060801 (2009).

Chapter 6

Main Findings and Suggestions for Future Work

6.1 Summary of Main Findings

This dissertation has dealt with three novel applications of coupled micro/nanomechanical resonators based on the concept of constructive use of intentional nonlinearity for design. Each of the presented designs integrated nanoscale components (nanotubes or nanomembranes) into microcantilever resonators, and was supported by theoretical analysis and experimental testing.

The first application discussed in Chapter 3 was motivated from previous studies (Cho *et al.*, 2010; Cho *et al.*, 2012), and geometric nonlinearity generated by the flexural oscillations of a nanotube attachment (specifically, a boron nitride nanotube) was implemented on a modified microcantilever design, which resembles the physical dimensions of a typical conventional AFM microcantilever. The integrated microcantilever – nanotube system successfully demonstrated the occurrence of broadband nonlinear resonance, unlike conventional linear AFM microcantilevers whose resonance is narrowband. Notably, it was found that the nonlinear damping originating from the geometric nonlinearity and the viscoelastic property of the locally attached nanotube had significant influence on the global dynamics of the integrated system, resulting in saturation of the effective Q-factor of the system, and confinement of the resonance

bandwidth under the high vacuum environment. Moreover, by fitting a theoretical model to experimental measurements we were able to quantify the different contributions to the response of the linear and nonlinear damping terms in different ambient pressures, which ultimately led to damping identification of the attached nanotube. The presented methodology was based on studying the effects on the global dynamics of a microstructure of a locally attached nanocomponent, so it can be used for damping identification of a more general class of nanoresonators such as nanowires and nanomembranes composed of different materials.

The second application considered in Chapter 4 was designed with the aim to overcome the challenges of accurate and reliable nanotube integration in microstructures of previous studies (Cho *et al.*, 2010; Cho *et al.*, 2012; Jeong *et al.*, 2013). In the system considered in that application, the implementation of nanocomponent coupling and intentional geometric nonlinearity was accomplished by assembling a silicon nanomembrane and integrating it through a transfer-printing technique as the coupling component onto the otherwise linear system of two microcantilevers. The transfer-printing assembly method not only showed that the geometric nonlinearity could be achieved in a reliable, convenient and mass-producible manner, but also allowed for fine tuning of the coupling strength via FIB post-processing. The experimental investigation with respect to the coupling strength performed with this system revealed unexpected nonlinear phenomena, especially in the limit of weak coupling. First, it was shown that nonlinear effects clearly emerged when the nonlinear mid-plane axial stiffness of the coupling bridge (nanomembrane) overcame the inherent linear stiffnesses of the inner and external

microcantilevers; also, that the nonlinear effects became more evident as coupling became weaker due to reduced width of the nanomembrane system. Then, we observed that in the limit of weak coupling the steady state oscillations of the microcantilevers were no longer synchronous in the vicinity of resonance, so that each sensing point of the microcantilever system exhibited its resonance peak at a different frequency; we conjectured that this was due to mode complexity, caused by the local damping provided by the oscillating nanomembrane and causing non-proportional damping distribution in the system. This mode complexity caused mode splitting and strong localization phenomena at intermediate frequency ranges between the in-phase and out-of-phase modes of the integrated system. It is noteworthy that these interesting phenomena occurred only below a critical threshold of coupling, and in that sense resemble nonlinear mode bifurcations leading to symmetry breaking, localization and motion confinement in weakly coupled discrete oscillators (Vakakis *et al.*, 1996).

In the final application discussed in Chapter 5, we presented a new design for AFM microcantilever incorporating an internal resonance between its two leading modes. When in tapping mode AFM operation, the nonlinear microcantilever tip-sample interaction triggers the internal resonance and energy transfer from the lower, directly excited mode to the higher mode occurs. The net result is that the responses at the higher harmonics of the cantilever response are amplified and can be utilized for high-frequency AFM operation. The utilization of tip-sample interaction in AM-AFM operation as an intrinsic source of nonlinearity to trigger high-frequency energy transfers between modes and amplify higher harmonics in the response was theoretically studied, and its feasibility was

assessed. Then, the enhancement of the higher harmonic amplitudes in the measured response was confirmed by computational analysis and experimental measurements. Remarkably, higher harmonic amplitude and phase signals not only resulted in improved spatial resolution of AFM imaging, but also mapped compositional differences of inhomogeneous polymer specimen consisting of PS and PDMS.

In summary, the applications presented in this work provide further examples of constructive utilization of strong nonlinearity in the micro- and nano-scale, and demonstrate the benefits of such designs compared to traditional linear approaches. Moreover, the findings reported in this dissertation convey interesting physical phenomena arising from strong stiffness and damping nonlinearities in coupled micro/nanomechanical resonating systems. These new findings can pave the way for novel applications, once systematic studies of the beneficial effects (and corresponding limitations) of intentional nonlinearities in designing this type of systems is accomplished.

6.2 Suggestions for Future Work

In what follows we provide suggestions for further work, and discuss certain potential applications of the developed nonlinear resonator designs.

Energy dissipation of one- and two-dimensional nanoscale components

Characterizing the damping effects of newly discovered nanomaterials, such as graphene and carbon nanotubes (CNTs), is important since their Q-factors (and thus their sensing

sensitivity) strongly depend on the energy dissipation of mechanical resonators composed of them. It is difficult, however, to quantitatively estimate the damping properties of nanoscale components through traditional methods, *e.g.*, classical tensile stress testing, due to their small dimensions. Indeed, when subjected to a compressive forces, one- or two-dimensional nanoscale structures will merely buckle as they are ultraflexible in their transverse directions. However, the methodology described in Chapter 3 (and successfully applied for studying geometrically nonlinear damping of a nanotube coupled to a microcantilever) can be employed to quantitatively measure energy dissipation, and characterize linear as well as nonlinear damping in these nanoscale components. In fact, energy dissipation in a silicon nanomembrane with a thickness of 300 nm is currently under investigation utilizing the approach developed in Chapter 3.

Complex nonlinear dynamical systems

As conjectured in Chapter 4, nonlinear damping in the coupling nanoscale component is expected to induce nonlinear complex modes in the coupled dynamic system. To adopt these modes in practical applications, it is required to develop analytical models to predict the dynamics, *e.g.*, resonance bands, for different system configurations. As a result, conceptually new broadband mechanical resonators can be implemented, exhibiting widely dispersed peak amplitudes (corresponding to different locations on the resonator) in the resonance band. Such resonators can be utilized as conceptually new frequency-modulated mechanical manipulators.

Nonlinear atomic force microscopy

A multi-frequency AFM microcantilever, realized by *1:n* internal resonance, has proven to generate the compositional map of the specimen simultaneously with its topography. The research results presented in Chapter 5 still require the analytical studies to conclusively correlate the measured responses at the higher harmonics to the quantitative properties of the interacting surface. Once this relation is revealed, we expect that the current design can be further modified to possess multiple higher harmonics. Utilizing such multiple frequencies may improve the measurement precision by analyzing and comparing each higher harmonic component separately or in combination. Besides, the amplification of higher harmonic signals needs to be further investigated to achieve enhanced sensitivity – one convenient way to achieve it is to test the multi-frequency AFM microcantilever described in Chapter 5 in liquid environment, where intrinsic amplification of higher harmonics has been reported in previous studies (Preiner, *et al.*, 2007; Xu, et al., 2009).

Intentional nonlinearity for frequency-up conversion

Finally, unidirectional energy transfer from one mode to another by internal resonance, also known as targeted energy transfer (TET) (Vakakis *et al.*, 2008), can be employed in micro/nanoscale dynamic systems to achieve energy conversion from low to high frequencies. The frequency multiplier in an electrical circuit is one of the potential applications. By introducing TET in a typical micro/nanomechanical resonator to convert up the input frequency, we expect that the electromechanical frequency multiplier can be realized. Besides, a micro/nanoscale vibration energy harvester is another potential

application that can benefit from the frequency-up conversion through TET. Regarding that the frequency of ambient environmental vibration is usually too low (<100 Hz) to be accommodated for micro/nanoscale energy harvesting, converting this frequency up to the operational bandwidth of the typical micro/nanoscale energy harvester (>1 kHz) can enable harvesting of environmental vibration energy. For both of the aforementioned applications, we believe that the intentional nonlinearity realized by the integration of the nanoscale component can be a key solution.

REFERENCES

Cho, H., Yu, M.-F., Vakakis, A.F., Bergman, L.A., McFarland, D.M., Tunable, broadband nonlinear nanomechanical resonator, *Nano Lett.*, 10, 1793-1798 (2010).

Cho, H., Jeong, B., Yu, M.-F., Vakakis, A., McFarland, D. M., Bergman, L., Nonlinear hardening and softening resonances in micromechanical cantilever-nanotube systems originated from nanoscale geometric nonlinearities, *Int. J. Sol. Struct.*, 49, 2059-2065 (2012).

Jeong, B., Cho, H., Yu, M.-F., Vakakis, A., McFarland, D. M., Bergman, L.A.; Modeling and measurement of geometrically nonlinear damping in a microcantilever-nanotube system, *ACS Nano*, 10, 8547-8553 (2013).

Preiner, J., Tang, J., Pastusehnko, V., Hinterdorfer, P., Higher Harmonic Atomic Force Microscopy: Imaging of Biological Membranes in Liquid, *Phys. Rev. Lett.*, 99, 046102 (2007).

Xu, X., Melcher, J., Basak, S., Reifenberger, R., Raman, A., Compostional Contrast of Biological Materials in Liquids Using the Momentary Excitation of Higher Eigenmodes in Dynamic Atomic Force Microscopy, *Phys. Rev. Lett.*, 102, 060801 (2009).

Vakakis, A.F., Manevitch, L.I., Mikhlin, Y.V., Pilipchuk, V.N., Zevin, A.A., *Normal Modes and Localization in Nonlinear Systems*, John Wiley & Sons (1996).

Vakakis, A.F., Gendelman, O., Bergman, L.A., McFarland, D.M., Kerschen, G., Lee, Y.S., *Passive Nonlinear Targeted Energy Transfer in Mechanical and Structural Systems*, Springer Verlag (2008).